Fabrication and Characterization of Thin Film Transistors based on Sol-Gel Derived Zinc Oxide Channel Layers

by

Vahid Mirkhani

A dissertation submitted to the Graduate Faculty of
Auburn University
in partial fulfillment of the
requirements for the Degree of
Doctor of Philosophy

Auburn, Alabama
May 5, 2018

Keywords: ZnO, Sol-Gel, Spin-Coating, Characterization,
Thin Film Transistors, Gamma Irradiation

Copyright 2018 by Vahid Mirkhani

Approved by

Minseo Park, Chair, Professor of Physics
Michael C. Hamilton, Associate Professor of Electrical & Computer Engineering
Sarit Dhar, Associate Professor of Physics
Michael Bozack, Professor of Physics
Ayayi C. Ahyi, Associate Research Professor of Physics
Majid Beidaghi, Assistant Professor of Mechanical and Material Engineering

به نام آنکه هستی نام ازو یافت   فلک جنبش زمین آرام ازو یافت

" پس همانا همراه سختی ، آسانی ست.

همانا همراه سختی آسانی ست ! "

تقدیم به:

مهربان ترین و شیرین ترین مادر ، اعظم حیدریان

صبور ترین و دلسوز ترین پدر ، داوود میرخانی رشتی

زیبا ترین ، پاک ترین ، کوشا ترین و عزیز ترین خواهران ،

پوپک ، ماهک ، مهرک

فداکار ترین و وفادار ترین همسر ، یار نازنینم ، شادی وجودم ،

نسرین

Abstract

This dissertation aims to explore film and device characteristics of zinc oxide (ZnO) based channel layers fabricated *via* the sol-gel spin-coating growth technique. ZnO is wide band gap semiconductor with a wide range of industrial applications and numerous electronic applications such as optoelectronics, flexible transparent electronics and sensors. ZnO films were synthesized with different number of layers by repeating the spin-coating process and then annealed at different temperatures. Micro-Raman, Photoluminescence (PL), Scanning Electron Microscopy (SEM) and X-ray Diffraction (XRD) were used for film characterization and to investigate crystal quality of the films. The results indicated an increase in the magnitude of E_2^{High} Raman shift as well as the near-band-edge PL peak as the annealing temperature increased. This intensification was related to the enlargement of grain size as a result of higher annealing temperature. The area under the curve ratio for UV PL over visible PL, in addition to the intensification of E_2^{High} Raman peak, suggested higher film quality as the annealing temperature increases. However, SEM images revealed that annealing temperatures higher than 800 ℃ result in the formation of gaps between grains, causing non-continuity in the film. Bottom gate thin film transistors (TFTs) were fabricated and Current-Voltage (I-V) and Capacitance-Voltage (C-V) measurements were implemented to investigate a possible "kink-effect" (also known as the "hump-effect") in the multilayer-channel samples, due to the renowned surface oxygen chemisorption in oxide semiconductors. The measurements hint to the possibility of depletion layer formation at the ZnO-ZnO interlayer-interfaces. The kink effect disappeared after high doses of radiation, suggesting the likelihood of

the distortion of the depletion layers due to the displacement damage. After 18 months, the kink effect in unirradiated samples remained existent and in the irradiated samples, it remained absent. Multilayer ZnO TFTs were exposed to a ^{60}Co radiation source and the robustness of ZnO TFTs against gamma irradiation was verified by comparing the transfer and output characteristics of TFTs and the PL of the channel layers before and after irradiation. By applying High Resolution Digital Optical Microscopy and Atomic Force Microscopy (AFM), it was found that the thickness of the ZnO was drastically influenced by the irradiation. A model was provided to explain the possible etching mechanism. Three effective medium approximations were applied to theoretically investigate the modification of the refractive index of the flexible conductive polymer matrix Poly(3,4-ethylenedioxythiophene) and Poly(styrene sulfonic acid) (PEDOT:PSS) by gallium doped ZnO nanoparticle inclusions, as a function of volume fraction of nanoparticle inclusions. Calculations determined the desired volume fraction of the gallium doped nanoparticles to be between 45% and 71% when gallium dopant concentration varies between 0 and 4 percent.

Acknowledgments

My endless appreciations go to my advisor, Prof. Minseo Park, for believing in me, for his precious instructions, his inspirations and invaluable support in every way possible. This work would not have been possible without his patronage, endless encouragement and compassion. I would like to thank Prof. Hamilton for his valuable advices and directions during our project. My deep appreciations go to Prof. Ayayi Claude Ahyi for his patience, valuable counsels and teachings. In addition to training me on fabrication processes and device measurements, Mrs. Tami Isaac-Smith was always sympathetic and kind. Thank you, Tami. I also want to thank Mr. Max Cichon for all his help, including gamma irradiation of the samples. My great appreciations go to Prof. Sarit Dhar for giving me insightful instructions, as well as giving me the opportunity to use the atomic force microscope. My deep gratitude goes to Prof. Michael Bozack for his support and for accepting to kindly serve as my committee member in such a short notice. My appreciations also go to Prof. Majid Beidaghi for his encouragement, collaboration, for kindly accepting to serve as my external committee member and for his inspection of my dissertation. In addition, I would like to thank Dr. Burcu Ozden for her companionship, benevolence, loyalty and integrity; Dr. Mobassar Hasssan Sk for his friendship and our invaluable conversations; Dr. Shiqiang Wang for selflessly helping me when needed; and Mr. Muhammed Shezad Sultan for his grace and brotherly love, as well as his kind help on data analysis. I want to deeply thank Mr. Kosala Yapabandara, Mr. Min Khanal and Mr. Sunil Uprety for our precious discussions and for all the help they provided me with. My thanks

go to Mr. Chungman Yang for his friendship and for training me on fabrication processes; Mr. Benjamin Schoenek and Mr. Suman Das for helping me with AFM images; and Mr. Asanka Jayawardena for our fruitful discussions over four-probe measurement and DLTS. My deep gratitude goes to Dr. Jie Jiang for his advices on ZnO sample preparations and characterization instructions. My thanks and commendations go to Mr. Uisub Shin, Mr. Sangjong Ko and Ms. Suhyeon Youn for their friendship and providing me with a considerable amount of assistance with Raman and PL measurements and data analysis. I would also like to thank Dr. Fei Tong for training me on Raman Spectroscopy and Dr. Yoonsung Chung for assisting us in our sample preparation.

Finally, I wish to express my deepest love to my treasured parents Mr. and Mrs. Davoud Mirkhani Rashti and Azam Heydarian, and my beloved sisters Poopak, Mahak and Mehrak. My innermost gratitude goes my cherished wife, future Dr. Nasrin Mohabbati Kalejahi, for her passionate support, immeasurable love, and her boundless dedication and selflessness.

Table of Contents

Abstract iii

Acknowledgments v

List of Tables viii

List of Figures ix

List of Abbreviations xv

Chapter 1: Introduction 1

References 4

Chapter 2: Literature Review 6

References 43

Chapter 3: Growth and Characterization of ZnO Channel Layers 60

3.1 Sol-gel Spin-Coating Growth 60

3.2 Raman Spectroscopy 62

3.3 Photoluminescence 79

3.4 Scanning Electron Microscopy 86

References 87

Chapter 4: Formation of Depletion Layers at ZnO-ZnO Interlayer-Interfaces 94

4.1 Introduction 94

4.2 Experimental 96

4.3 Results and Discussion 97

4.4 Conclusion 107

References 110

Chapter 5: Gamma Irradiation Effects on Sol-Gel Derived Thin Film Transistors 115

5.1 Introduction 115

5.2 Experimental 118

5.3 Results and Discussion 119

5.4 Conclusion 138

References 140

Chapter 6: ZnO Nanoparticle Inclusions as Refractive Index Modifiers 149

6.1 Introduction 149

6.2 Simulation Details 151

6.3 Results and Discussion 153

6.4 Conclusion 160

References 161

Chapter 7: Summary and Future Work 164

7.1 Summary 164

7.2 Future Work 166

List of Tables

Table 2.1: Fundamental properties of wurtzite zinc oxide 7

Table 2.2: Mechanical properties of wurtzite zinc oxide acquired by experimental techniques .. 8

Table 2.3: Cohesive energies for B4 (wurtzite), B3 (zinc blende), B1 (rocksalt), and B2 (CsCl) phases of ZnO. All extensive quantities are per ZnO formula unit 13

Table 2.4: Comparison of ZnO TFT characteristics, deposited *via* different methods.............. 39

Table 3.1: Thickness range for ZnO samples with different number of layers annealed at different temperatures 61

Table 3.2: Experimental Raman shifts and configurations required to observe the phonon modes in bulk single-crystal wurtzite ZnO. The bar over a direction (*e.g.* $\bar{X}$) represents the opposite of that direction (*e.g.* X) 74

Table 3.3: Raman shift values reported by experimental groups... 77

Table 5.1: Device characteristics of 4L-1 and 4L-2 before and after irradiation. The arrows indicate the enhancement/decline of the value compared to the unirradiated sample. 123

Table 5.2: Device characteristics of 8L-1 and 8L-2 before and after irradiation. The arrows indicate the enhancement/decline of the value compared to the unirradiated sample. 128

Table 6.1: Refractive Index of Ga-ZnO 154

List of Figures

Figure 2.1: Ball and stick presentation of zinc oxide crystal structures: (a) cubic rock salt (B1), (b) cubic zinc blende (B3), (c) hexagonal wurtzite (B4). The structures were generated by *VESTA*.10

Figure 2.2: (a) The Brillouin zone in reciprocal lattice. (b) Wurtzitic ZnO structure with lattice constants a (basal plane) and c (basal direction); u parameter (0.375 for an ideal crystal) obtained by dividing the bond length (nearest-neighbor distance) b by c; and equal bond angles α and β (109.47° for an ideal crystal) 10

Figure 2.3: ZnO band structure and valence band maximum splitting due to spin-orbit coupling. The open circles were obtained *via* atomic sphere approximation linearized muffin-tin orbital method (including spin-orbit coupling) and the black lines represent a fit to Rashba-Sheka-Pikus effective Hamiltonian.......... 14

Figure 2.4: Simulation of ZnO Band structure by LDA (solid lines) and G^0W^0 method (green circles) on the left, BITC (solid lines) and VMC (red circle) methods with experimental data (black dots) in the middle figure, and HF (solid line) method on the right. Blue broken lines show experimental data for the positions of the conduction band minimum, the O-2p bottom, and the Zn-3d peak position 16

Figure 2.5: Native point-defect formation energies as a function of Fermi level position in zinc-rich (left) and oxygen-rich (right) environments. The lowest-energy charge states are represented on the graph.......... 29

Figure 2.6: Cross-section schematics of typical MOSFETs and TFTs.......... 37

Figure 2.7: Flow diagram of the sol-gel deposition process.......... 40

Figure 2.8: Flow diagram for the reverse photolithography process.......... 42

Figure 3.1: Infra-red transition (a), Rayleigh scattering (b), Stokes (c) and anti-Stokes (d) Raman scattering, and fluorescence (e) among electronic and vibrational energy levels.......... 64

Figure 3.2: Polarizability ellipsoids' evolutions during displacements in different vibrational modes ν_1, ν_2 and ν_3 in (a) CO_2 and (b) H_2O molecules ... 73

Figure 3.3: The Raman shift of bulk ZnO. The E_2^H , E_1(TO) and A_1(LO) modes can be observed ... 75

Figure 3.4: The dependence of Raman spectra of ZnO layers deposited *via* sol-gel spin-coating method on the annealing temperature for (a) 1 layer, (b) 2 layers, (c) 3 layer, (d) 4 layers and (e) 8 layers ... 78

Figure 3.5: The dependence of E_2^H Raman shift and the FWHM of the peak on the annealing temperature for the 8-layer ZnO ... 79

Figure 3.6: Energy states created by native point defects as reported by (a) Djurišić *et al.*, (b) Lima *et al.*, (c) Lin *et al.*, (d) Nikitenko *et al.*, (e) Van de Walle, (f) Janotti and Van de Walle, and (g) Zwingel ... 82

Figure 3.7: PL spectrum of bulk ZnO ... 82

Figure 3.8: PL spectra of ZnO films for different annealing temperatures: (a) 1 layer, (b) 2 layers, (c) 3 layer, (d) 4 layers and (e) 8 layers. The insets depict the visible region ... 83

Figure 3.9: Peak position center, Xc, for (a) the NBE emission, Xc1, and (b) the exciton-exciton "P" emission, Xc2, as a function of annealing temperature ... 84

Figure 3.10: Peak position center, Xc, for (a) the NBE emission, Xc1, and (b) the exciton-exciton "P" emission, Xc2, as a function of the number of layers ... 85

Figure 3.11: Ratio of the integrated area under the UV PL over the visible PL as a function of (a) annealing temperature and (b) number of layers ... 85

Figure 3.12: SEM images of the 2-layer ZnO film annealed at 600 ℃ (top left), 700 ℃ (top right), 800 ℃ (bottom left), and 900 ℃ (bottom right) ... 86

Figure 4.1: Left: Optical image of bottom-gate ZnO TFT with 4 channel layers (4L) with a mean film thickness of $100\ nm$ on a $247\ nm$ dry oxidized SiO_2. Right: The cross-section schematics of the Corbino bottom-gate ZnO TFTs ... 97

Figure 4.2: Left: X-ray Diffraction pattern obtained from the 4L ZnO sample. The smaller peak at 33 degrees represents the silicon wafer. The inset shows the 34.5 degrees peak at a higher magnification. Right: Raman shift of the 8L sample. The 436.8 cm^{-1} and 520 cm^{-1} correspond to the ZnO E_2^{High} (oxygen vibration) and the single crystal silicon wafer under the transparent silicon dioxide substrate, respectively 98

Figure 4.3: Output characteristics of samples 1L (a), 4L (b), and 8L (c) 100

Figure 4.4: Drain current (black squares) and transconductance (blue stars) of samples 1L (a), 4L (b) and 8L (c) as a function of gate-source voltage bias. A kink effect can be observed in the transfer characteristics, as well as local maxima in the multiple layer samples 101

Figure 4.5: Normalized quasi-static capacitance-voltage measurements for samples 1L (a), 4L (b) and 8L (c). The insets exhibit the specific region with a higher magnification to distinguish the kink-effect in 4L (b) from a possible noise in 1L (a) 105

Figure 4.6: Device cross-section schematics of representation the ZnO-ZnO interlayer-interfaces with gate bias at depletion mode (left). The red arrows represent the electric field applied by the bottom gate, fully depleting the active layer (hatched area). Energy band diagram representation of the channel layer with gate bias lower than V_{ON} (right) 108

Figure 4.7: Device cross-section schematics of representation the ZnO-ZnO interlayer-interfaces with gate bias just above V_{ON} (left). The red arrows represent the electric field applied by the bottom gate, partially depleting the active layer (hatched area). Energy band diagram representation of the channel layer with gate bias just above V_{ON}, allowing carriers to form a back channel (right) 108

Figure 4.8: Device cross-section schematics of representation the ZnO-ZnO interlayer-interfaces (left). The red arrows represent the electric field applied by the bottom gate, depleting (hatched area) parts of the active layer just below the potential barrier at the interface. Energy band diagram representation of the channel layer with gate bias just below the critical voltage (V_C) just before the hot carriers can tunnel through the barrier (right) 109

Figure 4.9: Device cross-section schematics of representation the ZnO-ZnO interlayer-interfaces (left). The red arrows represent the electric field applied by the bottom gate, depleting (hatched area) parts of the active layer well below the potential barrier at the interface. Energy band diagram representation of the channel layer with gate bias just above the critical voltage (V_C), allowing the hot carriers to tunnel through the barrier (right) 109

Figure 5.1: Characteristics of the devices from 4L wafer before irradiation. Top: Output (right) and saturation transfer (left) curves for Un-4L-1. Bottom: Output (right) and saturation transfer (left) curves for Un-4L-2 120

Figure 5.2: Characteristics of the devices from 4L wafer after 1.2 MGy irradiation. Top: Output (right) and saturation transfer (left) curves for 120-Irr-4L-1. Bottom: Output (right) and saturation transfer (left) curves for 120-Irr-4L-2.......... 121

Figure 5.3: Characteristics of the devices from 8L wafer before irradiation. Top: Output (right) and saturation transfer (left) curves for Un-8L-1. Bottom: Output (right) and saturation transfer (left) curves for Un-8L-2 125

Figure 5.4: Characteristics of the devices from 8L wafer after 1.2 MGy irradiation. Top: Output (right) and saturation transfer (left) curves for 120-Irr-8L-1. Bottom: Output (right) and saturation transfer (left) curves for 120-Irr-8L-2.......... 126

Figure 5.5 Characteristics of the devices from 8L wafer after 2.2 MGy irradiation. Top: Output (right) and saturation transfer (left) curves for 220-Irr-8L-1. The gate insulator of the other device, 220-Irr-8L-2, experienced a permanent break down due to the high gate voltage bias…........ 127

Figure 5.6: Optical microscope top view of irradiated circular TFTs from the samples: 4L sample after 1.2 MGy (Top Left), 4L sample after 2.2 MGy (Top Right), 8L sample after 1.2 MGy (Bottom Left), 8L sample after 2.2 MGy (Bottom Right) 129

Figure 5.7: AFM of the ZnO/SiO_2 edge (left) and ZnO film surface topography (right) of pristine sample from 4L wafer.......... 130

Figure 5.8: AFM of the 4L sample after 1.2 MGy gamma irradiation. The ZnO/SiO_2 edge (left) and the ZnO film surface topography (right).......... 130

Figure 5.9: AFM of the 4L sample ZnO/SiO_2 edge after 2.2 MGy gamma irradiation from 2 different regions (left and right). The faint tilted-vertical border line at the center of the image (left) is the ZnO/SiO_2 edge.......... 131

Figure 5.10: AFM images of the sample from the 8L wafer after 1.2 MGy gamma irradiation dose: the ZnO/SiO_2 edge (left) and the surface topography (right).......... 131

Figure 5.11: Compton scattering inside ZnO lattice. The orange and blue sphere represent O and Zn atoms. The incoming photons (violet arrows) collide with electrons inside the lattice. The outgoing photons (red arrows) have a smaller energy, transferring momentum to energetic electrons (green arrows).. 133

Figure 5.12: Energetic electrons go through inelastic collisions with the lattice atoms. The outgoing nuclei collide with other atoms inelastically. The displacement chain stops when the last nucleus' energy is smaller than the threshold atomic displacement energy of other atoms................... 135

Figure 5.13: Stable distortions (inside the green circle) require higher number of displacements ($n \geq 5$). If the atom being displaced is a surface atom, it might leave the lattice (the atom inside the red circle) 135

Figure 5.14: PL spectra of the sample from the 4L wafer (a) and the 8L wafer (b) before and after irradiation 137

Figure 5.15: Gate current as a function of gate-source voltage after different irradiation doses for 8L-1 (*i.e.* Un-8L-1, 120-8L-1 and 220-8L-1). The inset indicates the magnified leakage current for the unirradiated sample 138

Figure 6.1: Schematics of the embedded Ga doped ZnO nanoparticles in PEDOT:PSS polymer matrix. 153

Figure 6.2: Effective Refractive Index of Ga-ZnO/PEDOT:PSS determined by BG at 403nm... 155

Figure 6.3: Effective Refractive Index of Ga-ZnO/PEDOT:PSS determined by MG at 403nm... 155

Figure 6.4: Effective Refractive Index of Ga-ZnO/PEDOT:PSS determined by LL at 403nm... 156

Figure 6.5: Effective Refractive Index of Ga-ZnO/PEDOT:PSS determined by BG at 550nm… 156

Figure 6.6: Effective Refractive Index of Ga-ZnO/PEDOT:PSS determined by MG at 550nm... 157

Figure 6.7: Effective Refractive Index of Ga-ZnO/PEDOT:PSS determined by LL at 550nm... 157

Figure 6.8: Effective Refractive Index of Ga-ZnO/PEDOT:PSS determined by BG at 650nm... 158

Figure 6.9: Effective Refractive Index of Ga-ZnO/PEDOT:PSS determined by MG at 650nm... 158

Figure 6.10: Effective Refractive Index of Ga-ZnO/PEDOT:PSS determined by LL at 650nm… 159

List of Abbreviations

2DEG	2-Dimensional Electron Gas
AFM	Atomic Force Microscopy
ALD	Atomic Layer Deposition
AZO	Aluminum doped ZnO
BG	Bruggeman
BJT	Bipolar Junction Transistors
CCD	Charge-Coupled Device
CBM	Conductance Band Minimum
CM	Center of Mass
C-V	Capacitance-Voltage
CVD	Chemical Vapor Deposition
DAP	Donor-Acceptor Pairs
DC	Direct Current
DFT	Density Functional Theory
DI	Deionized
ECR MBE	Electron Cyclotron Resonance Assisted Molecular Beam Epitaxy
EL	Electroluminescence
EMA	Effective Medium Approximations

FET	Field Effect Transistor
FWHM	Full Width at Half Maximum
HCP	Hexagonal Close-Packed
HF LCAO	Hartree-Fock Linear Combination of Atomic Orbitals Method
HEMT	High Electron Mobility Transistor
Ga-ZnO	Gallium doped Zinc Oxide
GGA	General Gradient Approximation
IGZO	Indium Gallium Zinc Oxide
I-V	Current-Voltage
IZO	Indium Zinc Oxide
LDA	Local Density Approximation
LCD	Liquid Crystal Displays
LED	Light Emitting Diode
LL	Lorentz-Lorenz
LO	Longitudinal Optical
MBE	Molecular Beam Epitaxy
MEA	Monoethanolamine
MESFET	Metal Semiconductor Field Effect Transistor
MG	Maxwell-Garnet
MOCVD	Metalorganic Chemical Vapor Deposition
MOSFET	Metal Oxide Semiconductor Field Effect Transistor

MOVPE	Metalorganic Vapor Phase Epitaxy
MS	Magnetron Sputtering
NBE	Near Band Edge
NC	Nanocrystalline
NP	Nanoparticles
OLED	Organic Light Emitting Diode
OMVPE	Organometallic Vapor Phase Epitaxy
OSC	Organic Solar Cells
PBE	Perdew-Burke- Ernzerhof
PEALD	Plasma-Enhanced Atomic Layer Deposition
PECVD	Plasma-Enhanced Chemical Vapor Deposition
PEDOT:PSS	Poly(3,4-ethylenedioxythiophene) and Poly(styrene sulfonic acid)
PEMOCVD	Plasma-Enhanced Metalorganic Chemical Vapor Deposition
PL	Photoluminescence
PLD	Pulsed laser deposition
PP LDA	Pseudopotential Local Density Approximation
QHO	Quantum Harmonic Oscillator
rf	Radio Frequency
RHEED	Reflected High Energy Electron Diffraction
RMS	Reactive Magnetron Sputtering
RS	Rock Salt

RTA	Rapid Thermal Annealing
RTM	Repeated Temperature Modulation
SCVT	Seeded Chemical Vapor Transport
SEM	Scanning Electron Microscopy
SHO	Simple Harmonic Oscillator
SIC PP LDA	Self-Interaction Corrected Pseudopotential Local Density Approximation
SIMS	Secondary Ion Mass Spectrometry
SS	Subthreshold Swing
TFT	Thin Film Transistor
TO	Transverse Optical
UV	Ultraviolet
VBM	Valence Band Maximum
VPE	Vapor Phase Epitaxy
VTD	Vapor Transport Deposition
WBGS	Wide Band Gap Semiconductor
WZ	Wurtzite
XPS	X-ray Photoelectron Spectroscopy
XRD	X-ray Diffraction
ZB	Zinc Blende

Chapter 1

Introduction

During the last three decades the interest in zinc oxide (ZnO) research as a semiconductor has been uplifted, despite the compound being exploited in industry for more than 150 years. [1,2,3] In the realm of semiconductors, various compounds such as arsenides, phosphates, tellurides and selenides are toxic and often, a comprehensive discretion must be exercised during the fabrication process. ZnO is an odorless, non-toxic and ultra-violet (UV) absorbent mineral with various convenient growth methods. Furthermore, it has antibacterial behavior[4], making it ideal for rampant medical, cosmetic and nutrition applications in an industrial scale. Whereas the optical studies on this II-VI compound was initialized more than a century ago[5], various properties of ZnO such as the band structure, phonon dispersion, irradiation damage and donor/acceptor impurity behavior were investigated in 1950s and 1960s. ZnO has been recently scrutinized as a prominent candidate for numerous electronic applications such as transparent electrodes[6], varistors[7], solar cells[8], gas sensors[9], biosensors[10], piezo-phototronic[11] and optoelectronic[12] devices and etc. ZnO has been studied along organic conductors as well. Recently, ZnO-PEDOT nanowires with a core-shell structure were fabricated *via* hydrothermal growth, indicating fast switching rates and high efficiencies suitable for transparent displays.[13] Silicon is the dominant semiconductor implemented in electronics. Yet, the relatively small indirect band gap (~1.12 eV) of the

semiconductor imposes limitations on the electronic properties such as their operation temperature. This is where the wide band gap semiconductors (> 2eV) come into play. Wide band gap semiconductors (WBGS) can be utilized in power electronics and the efficiency of the devices are more advanced compared to the silicon-based devices. Another property of the WBGS such as zinc oxide (ZnO), gallium nitride (GaN), silicon carbide (SiC), titanium dioxide (TiO_2) and n-diamond is their transparency. Transparent electronics are far from being a mere ambition. Fully transparent screens are available due to the transmittive property of each device structure. On the contrary, the aforementioned WBGS are UV absorbent, as their band gap energy's corresponding wavelength lies between 400nm and 200nm. The UV absorption property along with non-toxicity of ZnO and TiO2 qualifies them to be in medical products such as sunscreen and cosmetics, as well as UV sensors. The UV absorption is not without consequences. The interacting photons produce electrons and holes which, as a result, contribute to the conductivity. In some crystals, such as ZnO and GaN, this conductivity amplification endures, even after the light source is removed and hence, the persistent photoconductivity effect.[14]

This work further explores the properties of thin film transistors fabricated *via* the sol-gel spin-coating growth method. Chapter 2 introduces the basic properties of ZnO and surveys the background research performed on different aspects of the direct WBGS such as its band structure, doping with elements from different groups, recent transactions on p-type doping of ZnO, ZnO High Electron Mobility Transistors (HEMT), different growth techniques, and etc.

In Chapter 3, the growth method applied for ZnO thin film deposition used as the active layer is discussed. The films are characterized by Raman spectroscopy, photoluminescence and Scanning Electron Microscopy (SEM) in order to investigate the crystal quality of the films.

Chapter 4 investigates the possibility of the formation of depletion layers at the ZnO-ZnO interlayer-interfaces during film deposition. In addition to film characterization methods such as X-ray Diffraction (XRD), Current-Voltage (I-V) and Capacitance-Voltage (C-V) measurements are conducted on TFTs. The measurements indicated a likelihood of depletion regions being present inside the ZnO bulk.

ZnO TFTs with 2 different thicknesses were fabricated and irradiated with gamma rays. After device measurements, the samples were additionally irradiated to a higher dose to examine the consequences of irradiation on the thicker sample. The results are presented in Chapter 5. Although the transistors with different thicknesses displayed different traits, measurements after additional irradiation resulted in an apparent trend as the thickness of the channel layer was lessened, due to displacement damage occurred to the surface atoms.

In Chapter 6, in an attempt to match the refractive index of the organic conductive layer (PEDOT:PSS) with the emissive layer, effective medium approaches were applied to increase the refractive index of the conductive layer with doped ZnO nanoparticle inclusions. Gallium doped ZnO nanoparticles with different doping concentrations and therefore, different refractive indices were used to obtain a range for the volume fraction of nanoparticle inclusions inside the conductive layer.

References

[1] Milbank, I.M., 1860. Improvement in apparatus for manufacturing oxide of zinc. U.S. Patent 27,142.

[2] Whabton, J., 1862. Improvement in furnaces for the manufacture of oxide of zinc. U.S. Patent 37,190.

[3] Harrison, J., 1847. Improvement in compositions for door-knobs. U.S. Patent 5,315.

[4] Zhang, L., Jiang, Y., Ding, Y., Povey, M. and York, D., 2007. Investigation into the antibacterial behaviour of suspensions of ZnO nanoparticles (ZnO nanofluids). Journal of Nanoparticle Research, 9(3), pp.479-489.

[5] Nichols, E.L. and Snow, B.W., 1892. II. On the character of the light emitted by incandescent zinc oxide. The London, Edinburgh, and Dublin Philosophical Magazine and Journal of Science, 33(200), pp.19-28.

[6] Minami, T., Nanto, H., Shooji, S. and Takata, S., 1984. The stability of zinc oxide transparent electrodes fabricated by RF magnetron sputtering. Thin Solid Films, 111(2), pp.167-174.

[7] Gupta, T.K., 1990. Application of zinc oxide varistors. Journal of the American Ceramic Society, 73(7), pp.1817-1840.

[8] Law, M., Greene, L.E., Johnson, J.C., Saykally, R. and Yang, P., 2005. Nanowire dye-sensitized solar cells. Nature materials, 4(6), pp.455-459.

[9] Yen, J.C., 1975. An investigation of the electrical properties of zinc oxide thin films influenced by oxygen adsorption. Journal of Vacuum Science & Technology, 12(1), pp.47-51.

[10] Wang, J.X., Sun, X.W., Wei, A., Lei, Y., Cai, X.P., Li, C.M. and Dong, Z.L., 2006. Zinc oxide nanocomb biosensor for glucose detection. Applied Physics Letters, 88(23), p.3106.

[11] Wang, Z.L., 2010. Piezopotential gated nanowire devices: Piezotronics and piezo-phototronics. Nano Today, 5(6), pp.540-552.

[12] Pauporté, T. and Lincot, D., 2000. Electrodeposition of semiconductors for optoelectronic devices: results on zinc oxide. Electrochimica Acta, 45(20), pp.3345-3353.

[13] Kateb, M., Safarian, S., Kolahdouz, M., Fathipour, M. and Ahamdi, V., 2016. ZnO–PEDOT core–shell nanowires: An ultrafast, high contrast and transparent electrochromic display. Solar Energy Materials and Solar Cells, 145, pp.200-205.

[14] Takahashi, Y., Kanamori, M., Kondoh, A., Minoura, H. and Ohya, Y., 1994. Photoconductivity of ultrathin zinc oxide films. Japanese Journal of Applied Physics, 33(12R), p.6611.

Chapter 2

Literature Review

Wurtzite ZnO is a direct wide band gap semiconductor (3.37 eV at room temperature) with a relatively high free exciton binding energy (60 meV) [1], appointing ZnO an exemplary candidate for excitonic emission applications, such as light emitting devices. This is due to its high device efficiency at room temperature (k_BT = 26 meV) among other direct band gap semiconductors' exciton binding energies such as GaAs (4.8 meV), CdTe (10 meV), 4H-SiC (20 meV), GaN (25 meV) and ZnSe (22 meV). [2,3,4]

ZnO has been compared to GaN due to their crystal structure, lattice constants and other various similarities due to the proximity of oxygen (zinc) with nitrogen (gallium). In addition to high free exciton binding energy, ZnO has several advantages, over GaN such as the possibility of wet etching and more resistance to irradiation.[5] Tables 2.1 and 2.2 represent the fundamental and the mechanical properties of wurtzite ZnO, respectively.

Table 2.1 Fundamental properties of wurtzite zinc oxide [6]

Property	Value
Lattice parameters at 300 K	
a	3.2495 Å
c	5.2069 Å
c/a	1.602
u	0.380
Density	5.606 $g.cm^{-3}$
Melting point	1975 °C
Thermal conductivity	0.6 – 1.2
Linear expansion coefficient (/ °C)	
a	6.5×10^{-6}
c	3.0×10^{-6}
Static dielectric constant	8.656
Refractive index	2.008 – 2.029
Energy gap	3.4 eV, direct
Carrier concentration	
Intrinsic (electrons)	$< 10^{6}$ cm^{-3}
Max n-type doping (electrons)	$> 10^{20}$ cm^{-3}
Max p-type doping (holes)	$< 10^{17}$ cm^{-3}
Exciton binding energy	60 meV
Electron effective mass (m_e^*)	0.24 m_0
Electron Hall mobility at 300 K for low n-type conductivity	200 $cm^2.V^{-1}.s^{-1}$
Hole effective mass (m_h^*)	0.59 m_0
Hole Hall mobility at 300 K for low p-type conductivity	5 – 50 $cm^2.V^{-1}.s^{-1}$

Table 2.2 Mechanical properties of wurtzite zinc oxide acquired by experimental techniques [7,8,9,10]

Parameters	Value
C_{11} (GPa)	157
C_{12} (GPa)	89
C_{13} (GPa)	83
C_{33} (GPa)	208
C_{44} (GPa)	38
C_{66} (GPa)	34
e_{31} (C.m^{-2})	– 0.51
e_{33} (C.m^{-2})	1.22
e_{15} (C.m^{-2})	– 0.45
Bulk modulus, *B* (GPA)	183
dB/*dP*	4.0
Young's modulus, *E* (GPa)	111.2
Hardness (GPa)	5.0

ZnO is among the many II-VI compound semiconductors which have recently been attracting attention. Due to its distinct properties, ZnO is one the most important metal oxide semiconductors. ZnO may crystalize in structures such as hexagonal wurtzite (WZ) ($P6_3mc$), zinc blende (ZB) and rock salt (RS) structures. Figure 2.1 indicates the aforementioned structures. The space group of these structures (WZ, ZB and RS) reside in $P6_3mc$, $F\bar{4}3m$ and $Fm\bar{3}m$ in the Hermann-Mauguin notation, respectively; and in C_{6v}^4 , T_d^2 and O_h^5 in the Schoenflies notation, respectively. The hexagonal wurtzite is the most stable structure of ZnO in the ambient temperature and the ambient pressure. The unit cell of this structure has two lattice constants $\boldsymbol{a}$ and $\boldsymbol{c}$ and the ideal ratio of $\frac{\boldsymbol{c}}{\boldsymbol{a}} = \sqrt{8/3}$. Experimental values for lattice constants are obtainable *via* X-ray

diffraction analysis (XRD). It can be indicated that the spacing $\vec{d}_{hkl}$ between reticular planes with Miller indices hkl for a crystal structure can be obtained from its relationship with the reciprocal space vector $\vec{N}^*_{hkl}$

$$\vec{N}^*_{hkl} \,.\, \vec{d}_{hkl} = 1 \,.$$

In hexagonal wurtzite structures, Bragg's relation $2d_{hkl} \sin\theta_{hkl} = n\lambda$ can be used to extract the lattice parameters, where n is the order of diffraction and λ is the wavelength of incident ray.[11]

$$\theta_{hkl} = = \sin^{-1} \{ \frac{n\lambda}{2d_{hkl}} \} = \sin^{-1} \{ \frac{n\lambda}{2} \sqrt{\frac{4}{3\boldsymbol{a}^2} (h^2 + hk + k^2) + \frac{l^2}{\boldsymbol{c}^2}} \}$$

For ZnO, the $\boldsymbol{a}$ parameter may vary from 3.2475 Å to 3.2501 Å and the $\boldsymbol{c}$ parameter may vary from 5.2042 Å to 5.2075 Å. The definition of the lattice constant $\boldsymbol{u}$ is defined as the length of oxygen-zinc bond along the c-axis by $\boldsymbol{u} = \frac{1}{3} \times (\frac{\boldsymbol{a}}{\boldsymbol{c}})^2 + \frac{1}{4}$. The $\frac{\boldsymbol{c}}{\boldsymbol{a}}$ ratio, which is influenced by the electronegativities of oxygen and zinc, varies between 1.593 to 1.6035 and the lattice constant $\boldsymbol{u}$ varies between 0.3817 to 0.3856. [12,13] The aforementioned empirical ratio values are in agreement with the ideal hexagonal wurtzite structure ratio values. The wurtzite structure can be formed by inserting two parallel hexagonal closed packed (HCP) structures into one another, one with zinc constituents and the other with oxygen atoms, with the separation lattice-constant $\boldsymbol{u}$ (Figure 2.2 (b)). Figure 2.2 (a) shows the Brillouin zone in reciprocal lattice. The high symmetry points of the Brillouin zone are $\Gamma = (0, 0, 0)$, $A = \frac{2\pi}{c}\left(0, 0, \frac{1}{2}\right)$,

$K = \frac{2\pi}{a}\left(\frac{\sqrt{3}}{3}, \frac{1}{3}, 0\right)$, $M = \frac{2\pi}{a}\left(\frac{\sqrt{3}}{3}, 0, 0\right)$, $H = \frac{2\pi}{a}\left(\frac{\sqrt{3}}{3}, \frac{1}{3}, \frac{a}{2c}\right)$, $L = \frac{2\pi}{a}\left(\frac{\sqrt{3}}{3}, 0, \frac{a}{2c}\right)$.

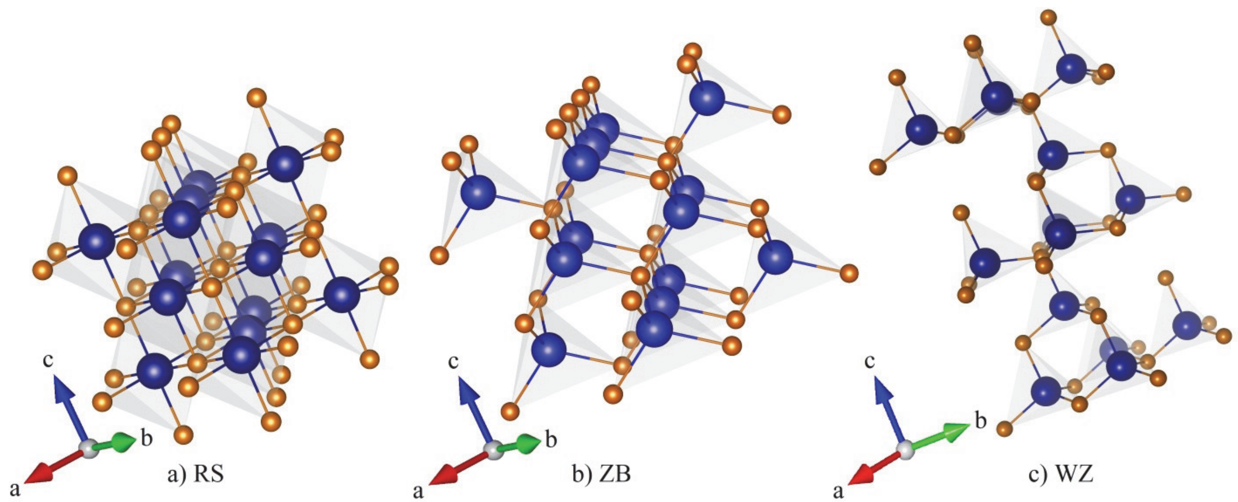

Figure 2.1: Ball and stick presentation of zinc oxide crystal structures: (a) cubic rock salt (B1), (b) cubic zinc blende (B3), (c) hexagonal wurtzite (B4). The structures were generated by *VESTA*.[14]

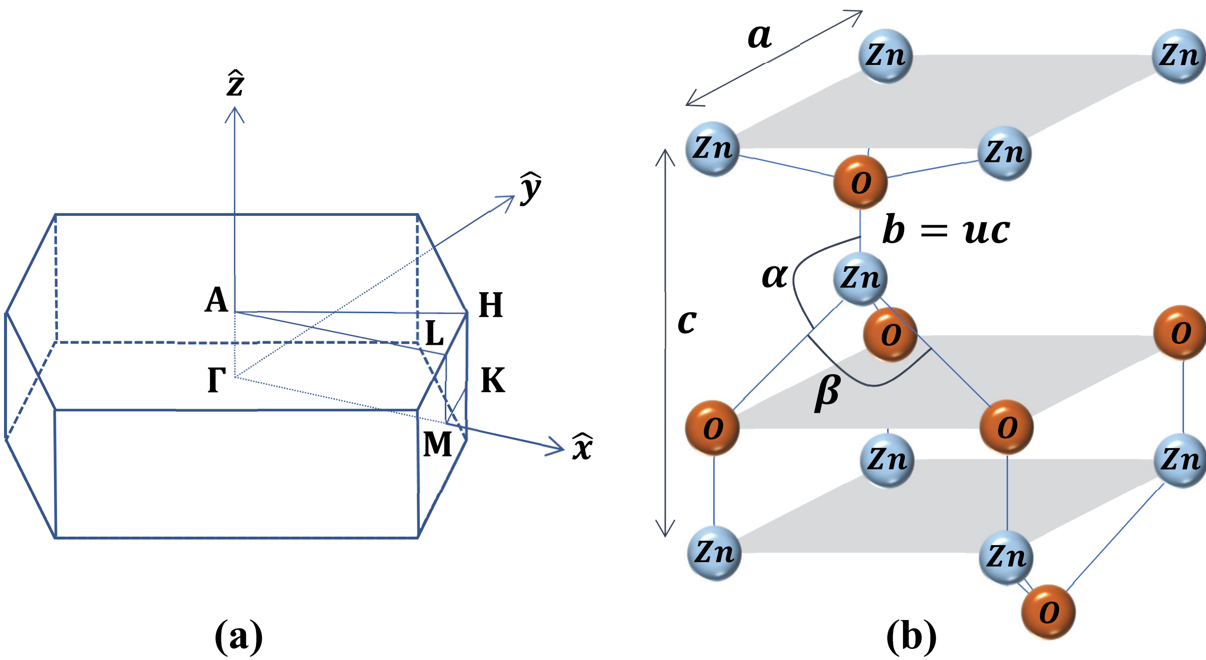

Figure 2.2: **(a)** The Brillouin zone in reciprocal lattice. **(b)** Wurtzitic ZnO structure with lattice constants $\boldsymbol{a}$ (basal plane) and $\boldsymbol{c}$ (basal direction); $\boldsymbol{u}$ parameter (0.375 for an ideal crystal) obtained by dividing the bond length (nearest-neighbor distance) $\boldsymbol{b}$ by $\boldsymbol{c}$; and equal bond angles $\boldsymbol{\alpha}$ and $\boldsymbol{\beta}$ (109.47° for an ideal crystal).

Along the c-axis, each basal plane consists of either Zn^{2+} or O^{2-} ions. The polar plane terminating with oxygen atoms (the $(000\bar{1})$ plane) is negatively charged while the polar plane terminating with zinc atoms (the (0001) plane) is positively charged. Every oxygen (zinc) atom is surrounded by four zinc (oxygen) atoms at the corners of a tetrahedron. The Zn-O bonds in the tetrahedron have an indication of sp^3 bonding (hybridization of zinc 3d and oxygen 2p orbitals) and yet, they possess a very strong ionic character as well. This ionic character tends to widen the band gap compared to the band gap expected from the purely covalent bonding. Due to ZnO crystal structure being deficient in any inversion symmetry, a spontaneous c-axis oriented electric dipole moment exists in every tetrahedron. The electromechanical coupling and the strong polarization along the c-axis, result in the pyroelectricity[15] and piezoelectricity[16] of ZnO, respectively. The layer growth advances along the c-axis (0001). Fujimura *et al.* grew ZnO *via* radio frequency (RF) magnetron sputtering with various conditions and Ar:O_2 compositions in order to manipulate the growth orientation of the films. Growth occurred along the $(10\bar{1}0)$ and $(11\bar{2}0)$ (a-axis) and (0001) (c-axis) orientations. The calculated values for the surface energy densities of the aforementioned orientations were 0.209 eV/ $Å^2$, 0.123 eV/ $Å^2$ and 0.099 eV/ $Å^2$, respectively.[17] Due to the surface energy density along the c-axis being minimum, growth along this orientation is the most stable. The maximal growth rate of ZnO nanostructures is normally along the (0001) orientation. Jin *et al.* grew ZnO *via* PLD, on sapphire (001), and confirmed the disappearance of the corresponding (1000) orientation XRD peak and the development of the (0002) XRD peak of ZnO subsequent to an increase in the growth temperature.[18]

A stable zinc blende ZnO structure can only be realized *via* growth on cubic substrates while the rocksalt ZnO structure requires high pressure. Under 9 GPa, the rocksalt ZnO can be formed and the stability can be maintained under pressures as high as 209 GPa, indicating the

feasibility of the use of ZnO in an internal pressure standard at high pressures.[19] Jaffe and Hess[20] implemented periodic Hartree-Fock linear combination of atomic orbitals method (HF LCAO) to calculate the ground state total energy of ZnO phases, as a function of unit cell volume, by addition of an isolated neutral Zn and an O atom energies after reoptimization of outer orbitals. Later, Jaffe *et al.*[21] calculated E_0 *via* the local density approximation (LDA) and general gradient approximation (GGA) for the three aforementioned phases in addition to a previously predicted B4 phase by Liu and Basset[22] where under an extremely high pressure the B1 phase (cubic NaCl) reconstructs into the B4 phase (cubic CsCl). The rough estimated base of the total cohesive energy (E_0) for each phase is summarized in Table 2.3 Whereas the GGA results in the closest result to the wurtzite ZnO experimental value -7.52 eV extracted from experimental Zn heat of vaporization, O_2 binding energy and ZnO enthalpy of formation[23], all methods confirm the higher stability of the hexagonal wurtzite structure with respect to other phases.

Electronic band structure of ZnO has been investigated by various groups *via* different experimental and theoretical approximation methods. Varshni[24] proposed a temperature dependent universal function for band gap (E_g) variation, based on experimental data for several semiconductors:

$$E_g(T) \approx E_g(T=0) - {\alpha T^2}/{\beta + T}$$

where α and β are constants. β is proportional to θ_D (Debye temperature). Wang and Giles[25] used temperature-dependent photoluminescence to determine α, β and θ_D and θ_E (Einstein temperature) values. They reported 700 K and 240 K as the Debye temperature and the Einstein temperature, respectively.

Table 2.3 Cohesive energies for B4 (wurtzite), B3 (zinc blende), B1 (rocksalt), and B2 (CsCl) phases of ZnO. All extensive quantities are per ZnO formula unit.

	LDA	GGA	HF	Experiment
B4	9.769	7.692	5.658	7.52
B3	9.754	7.679	5.606	
B1	9.611	7.455	5.416	
B2	8.462	6.334	N/A	

Wurtzite band structure was investigated by Birman[26] in 1959 and a spin-orbit splitting was reported for CdS. In 1960, D.G. Thomas[27] studied wurtzite ZnO band structure at low temperature (4.2 K) and witnessed the spin-orbit splitting in the valence band *via* reflectance and absorption measurements. Rossler[28] (among other researchers[29,30]) confirmed Thomas' results regarding the Γ_7 symmetry of the first and the third subbands (A and C) and the Γ_9 symmetry of the second subband (B), and adopted the empirical pseudopotential method (EPM) considering relativistic mass-velocity and Darwin corrections to calculate the energy band structure. Hopfield[31] considered the hexagonal structure as a perturbation of a cubic structure and developed a "quasi-cubic" Hamiltonian for wurtzite ZnO and derived the energy states for the valence band maxima A, B and C. By setting the top valence band energy to zero ($E_A = 0$), he derived other eigenstates as

$$E_{B,C} = -\frac{\delta + \Delta}{2} \pm \sqrt{\left[\left(\frac{\delta + \Delta}{2}\right)^2 - \frac{2}{3}\delta\Delta\right]}$$

The parameters δ and Δ represent contributions of spin-orbit and uniaxial field interactions, respectively, and can be obtained by measuring the level splitting E_{AB} and E_{BC}. Reynolds *et al.*[32] were able to observe free-exciton emission for the first time by investigating low temperature

photoluminescence (PL) and reflection spectra of wurtzite ZnO single crystal, grown by a seeded physical vapor transport method, in the presence of an external magnetic field. The experiment confirmed the spin-orbit splitting. The authors, however, suggested the Γ_9 symmetry for the top valence band (A) and Γ_7 symmetry for the lower valence bands (B and C). They measured δ and Δ as 16 meV and 43 meV, respectively. Figure 2.3 represents the splitting of the ZnO VBM, *via* simulations based on the density functional theory.[33]

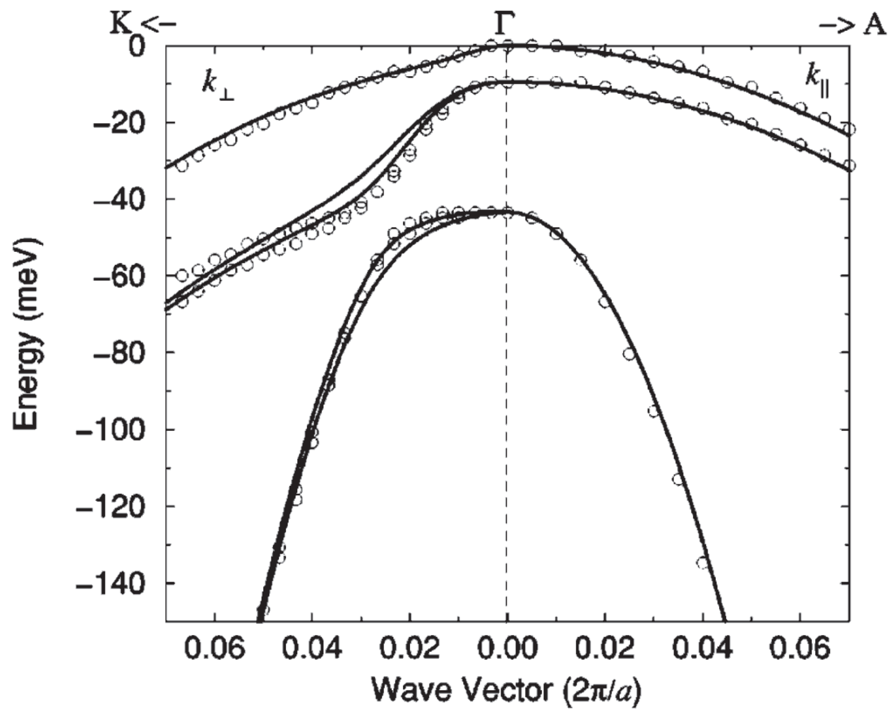

Figure 2.3: ZnO band structure and valence band maximum splitting due to spin-orbit coupling. The open circles were obtained *via* atomic sphere approximation linearized muffin-tin orbital method (including spin-orbit coupling) and the black lines represent a fit to Rashba-Sheka-Pikus effective Hamiltonian. *Reprinted figure with permission from Walter Lambrecht, Anna Rodina, Sukit Limpijumnong, B. Segall and Bruno Meyer, Valence-band ordering and magneto-optic exciton fine structure in ZnO, Physical review B, 65 (7), p.075207 (2002). Copyright (2002) by the American Physical Society.*

Among various theoretical approaches toward calculating ZnO band structure, standard pseudopotential local density approximation (PP-LDA) is implemented by most researchers. In this approximation, the cationic *d* electrons are not simply considered as core electrons in the valance band. Despite its infamous band gap underestimation and overestimation of occupied cationic *d* bands, lattice constants provided by LDA comply with experimental values.[34] Self-interaction corrected pseudopotential LDA (SIC-PP-LDA) mitigates these misestimations *via* the down-shifting of the *d* bands, drastic alteration of the bandwidth of oxygen anion 2p valence bands, and the reduction of p-d interactions between oxygen and zinc valence bands. Vogel *et al.* obtained a close estimate $\left(E_g = 3.77\ eV \right)$ using SIC-PP-LDA.[35] Shih *et al.*[36] implemented the GW method combined with LDA to simulate ZnO band structure while addressing the band convergence issues caused by the perturbative nature of the method. GW method formulates a one-particle Green's function for the electron-gas problem[37]; and by obtaining the Green's function *G*, the dynamical screened interaction *W* and approximating the self-energy operator, quasiparticle energies and wave functions can be calculated by solving the pseudopotential equation.[38] Figure 2.4 indicates band structure simulation by Ochi *et al.* [39] using various methods such as LDA, HF method, biorthogonal transcorrelated Hamiltonian method (BITC) and comparing these approximations with other studies such as the standard GW method (G^0W^0),[40] variational quantum Monte Carlo (VMC)[41] and experimental data by Zwicker and Jacobi[42]. Band structure computational results indicate that in crystal momentum space (k-space), all energy states forming the valence band maximum (VBM) are directly below the energy states forming the conductance band maximum. This entails the fact that electrons in the VBM may have transitions to the CBM without momentum change and hence, the direct band gap of ZnO.

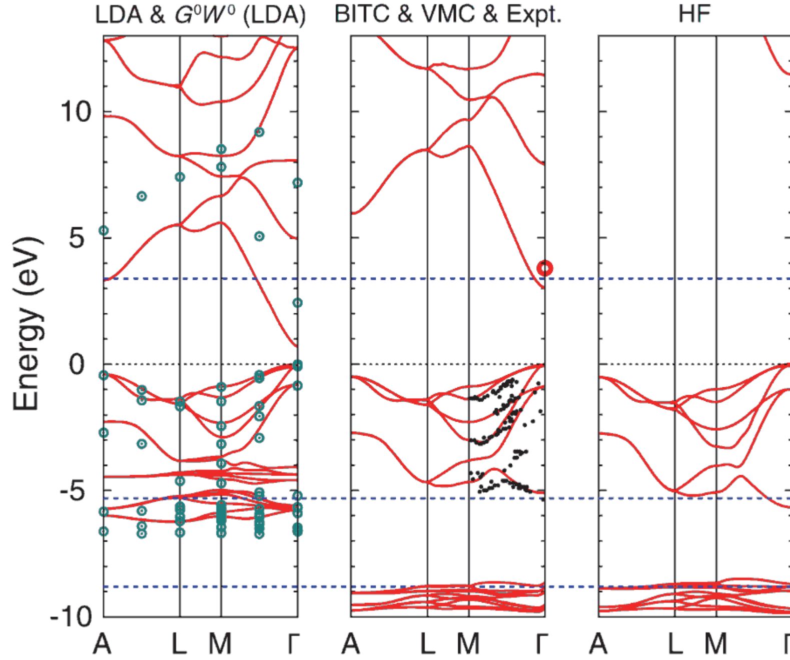

Figure 2.4: Simulation of ZnO Band structure by LDA (solid lines) and G^0W^0 method (green circles) on the left, BITC (solid lines) and VMC (red circle) methods with experimental data (black dots) in the middle figure, and HF (solid line) method on the right. Blue broken lines show experimental data for the positions of the conduction band minimum, the O-2*p* bottom[43], and the Zn-3d peak position.[44] The valence band maximum energy is set to 0 eV. *Reprinted figure with permission from Masayuki Ochi, Ryotaro Arita, and Shinji Tsuneyuki, Correlated Band Structure of a Transition Metal Oxide ZnO Obtained from a Many-Body Wave Function Theory, Physical Review Letters, 118 (2), p.026402 (2017). Copyright (2017) by the American Physical Society.*

Introducing impurities into the lattice structure can change the properties of the host (e.g. by introducing new energy states into the band gap). Donor or acceptor impurities may substitute zinc or oxygen, resulting in a higher or lower carrier concentration. Since ZnO indicates strong n-type conductivity, it's straightforward to dope the semiconductor with donor impurities for an increase in the free carrier concentration. Group III elements act as shallow donors by substituting Zn, having a dangling bond. Minami *et al.*[45] reported preparing highly conductive transparent Al-doped ZnO (AZO) thin films for use in transparent displays. The group later reported doping of ZnO with boron, aluminum, gallium, indium *via* rf magnetron sputtering and group III oxide powders (B_2O_3, Al_2O_3, Ga_2O_3 and In_2O_3). A general trend of decreased resistivity was observed

and the lowest resistivity was observed when the doping concentration reached 2~3 atomic% for impurities Al, Ga and In, and 10 atomic% for boron. [46] Fluorine can substitute for oxygen and act as a shallow donor due to its 2*p* orbital being half-filled. Hu and Gordon deposited F-doped ZnO films, *via* chemical vapor deposition (CVD). With deposition temperature of 450 ^{o}C and 0.25 at.% fluorine concentration, the highest doping efficiency of 96%, largest grain size of 250 nm, and highest electron mobility of 36 $cm^2.V^{-1}.s^{-1}$ was achieved.[47] Hydrogen doping of ZnO was first conducted by Mollwo[48] and later further studied by Thomas and Lander[49] who observed smooth diffusion of hydrogen into the crystal structure and measured diffusion coefficients. They proposed hydrogen atoms remaining as interstitial protons, forming shallow donors. Van de Walle[50] studied interstitial hydrogen sites in ZnO by using density functional theory (DFT) within the plane-wave pseudopotential local density approximation (PP-LDA) and proposed the non-amphoteric behavior of this element in ZnO as the host, in contrast to its behavior in other hosts where it counteracts prevalent conductivity.

Park *et al.*[51] applied alkali metal dopants (such as lithium, sodium, potassium and rubidium) *via* solution process and achieved higher mobility n-type ZnO thin film transistors (TFTs) compared to undoped samples. Interstitial sites for alkali metals are preferable for their lower formation energies where they will act as shallow donors; in contrast with substitutional sites where the impurities behave as acceptors. [52]

Whereas n-type doping of ZnO is relatively straightforward and the doped ZnO remains stable, albeit with limited dopant solubility, achieving the p-type ZnO has been controversial due to reproducibility and degradation issues. The II-VI semiconductors' resistance towards doping has been long established. Aven[53] considered acceptor doping difficulties to originate from (i) small solubility of the impurities compared to donor dopants, (ii) acceptor dopants acting as donors

when occupying other sites such as interstitials, (iii) the tendency of acceptor dopants to pair with other defects to form electrically inactive complexes. Yet, p-type ZnO opens the door to various device opportunities *via* proper p-n junction (homojunction) being fulfilled and therefore, has been of great interest for the past two decades. Numerous experimental attempts have been made and theoretical calculations have been conducted to investigate the possibility of the achievement. Ryu *et al.*[54] reported fabrication of homostructural p-n junction for ZnO for the first time, using Al-doped ZnO (n-type) and As-doped ZnO (p-type). A brief review of attempts at different dopants to realize p-type ZnO is presented as follows.

As mentioned, alkali metals may introduce acceptor levels if they are situated at substitutional sites. Lander[55] discussed the behavior of lithium dopant both as a donor and as an acceptor. As an interstitial impurity (Li_i), Li contributes to the free carrier concentration whereas when it substitutes Zn (Li_{Zn}), it pushes the Fermi level down to the center of the band gap. Wardle *et al.*[56] theoretically investigated the formation energies of Li_i , Li_{Zn} and their complexes with each other, with diffused hydrogen atoms in different sites, and with oxygen and zinc vacancies (V_O and V_{Zn}, respectively). They concluded that the deep levels cannot merely originate from isolated Li_{Zn}. Lithium usually compensates the n-type conductivity in ZnO. However, claims of p-type Li-doped ZnO with hole concentration of $p = 1.44 \times 10^{17}\ cm^{-3}$ was reported by Zeng *et al.*[57] and Lee *et al.*[58] reported the fabrication of homojunction diodes and back-gate field effect transistors (FETs) based on p-type Li-doped ZnO nanowires (NWs) and n-type ZnO thin films. Shin *et al.*[59] employed Li-doped ZnO NWs to fabricate flexible piezoelectric nanogenerators.

Lin *et al.*[60] estimated an acceptor level of 164 meV in sodium-doped ZnO films obtained by pulsed laser deposition (PLD). Lin *et al.* claimed realization of stable homojunction light

emitting diodes (LEDs) by applying n-type Al-doped ZnO and p-type Na-doped films and reported the electroluminescence (EL) and photoluminescence (PL) of the LEDs at low temperatures of 110 K and 10 K, respectively.

Copper-doped ZnO was studied by Dietz *et al.*[61] for its electronic structure and it was observed that a hole can be formed in the 3d shell of Cu. Dingle[62] observed the green luminescence of the impurity and proposed a binding energy for the deep acceptor level (~3.3 eV). To study the compensating behavior of copper, Muller[63] doped ZnO with hydrogen and indium to increase the carrier concentration and by using Cu as a co-dopant, he observed a reduction in carrier concentration and assigned it to the acceptor behavior of Cu. Many groups, however, have reported acquiring n-type ferromagnetic Cu-doped ZnO samples instead.[64,65,66,67]

Group V elements introduce acceptor levels into the band gap of ZnO due to their oxidation number. Kobayashi *et al.*[68] [cross ref.] theoretically predicted the shallow acceptor behavior of nitrogen but deemed other group V elements (P, As, Sb and Bi) as border line deep acceptors. Whereas nitrogen is the most suitable candidate to replace oxygen, other elements (P, As, Sb) result in deep acceptor states if they occupy oxygen sites (substitution). [cross ref.][69]

Aoki *et al.*[70] fabricated a ZnO diode by achieving phosphorus-doped ZnO, using excimer-laser pulses to deposit zinc phosphide (Zn_3P_2) on n-type ZnO substrate as dopant material, and observed white-violet electroluminescence at 110 K. Kim *et al.*[71] used phosphorus oxide (P_2O_5) as the dopant and claimed obtaining p-type ZnO implementing low-temperature photoluminescence (acceptor-bound exciton peak near 3.35 eV at 10 K) and Hall measurements. They suggested thermal activation using rapid thermal annealing (RTA) to overcome reproducibility and degradation issues.

Ryu *et al.*[72] reported synthesizing arsenic-doped ZnO for the first time *via* pulsed laser ablation in an ultra-pure oxygen ambient, characterized by low-temperature PL and Hall measurements. Ryu *et al.* later conducted more characterizations to present two acceptor levels of 115 and 164 meV above the valence band maximum (VBM), exciton binding energy of 12 meV and carrier concentration up to 10^{17} cm^{-3} for As-doped ZnO samples with different doping concentrations .[73]

Xiu *et al.*[74] grew antimony-doped ZnO *via* electron cyclotron resonance assisted molecular beam epitaxy (ECR-MBE) and claimed achieving a p-type conductivity with a high hole concentration of 10^{18} cm^{-3} and Hall mobility of 20 $cm^2.V^{-1}.s^{-1}$. Homojunction light emitting diodes were fabricated by Chu *et al.*[75] with Sb-doped ZnO (p-type) and Ga-doped ZnO (n-type) where low temperature electroluminescence (EL) exhibited strong UV emission. The group was able to obtain the constants for Varshni's temperature-dependent band gap equation ($\alpha = 5.8 \times 10^{-4}$ eV/K and $\beta = 520$ K) from near band edge (NBE) peak position of the EL spectra measured at various temperatures.

Considering the deep level of oxygen-substituting group V dopants, Limpijumnong *et al.*[76] presented a model to describe the possibility of shallow level behavior of the dopants in the "mysterious key experimental observations" of p-type ZnO. They suggested the dopants to substitute for zinc instead and form a complex with two zinc vacancies (*e.g.* As_{Zn}-$2V_{Zn}$). These complexes, however, have high formation energies and therefore, are scarce.

Following the predictions of Kobayashi *et al*. on shallow acceptor behavior of nitrogen in ZnO, Sato *et al.*[77] tried growing N-doped ZnO films on $\alpha-Al_2O_3$ substrates by zinc evaporation in O_2-N_2 mixed radio-frequency plasmas. The investigations on films annealed at different temperatures indicated n-type conductivity in all samples. Minegishi *et al.*[78], however, reported

achieving p-type N-doped ZnO by adding NH_3 and excess Zn into carrier gas and source during chemical vapor deposition (CVD). They claimed extreme difficulty in controlling the growth temperature. Joseph *et al.*[79] co-coped ZnO with Ga and N and claimed achieving high carrier concentration p-type ZnO thin films, but reported how subtle experimental parameter alterations may easily "flip" the carrier type. Look *et al.*[80] produced N-doped ZnO using MBE and compared their obtained hole concentrations (p) and hole mobility (μ_p) to previous p-type ZnO reports. The group criticized the fact that the acceptor levels in the 150 meV range, reported by various groups achieving p-type ZnO *via* doping, cannot result in such high hole concentrations claimed by these groups and further cautioned how deceitfully high values for p and low values for μ_p can be caused by artificially low Hall voltage differences. Tsukazaki *et al*.[81] observed violet to green regions in EL spectrum at room temperature from their fabricated ZnO LED with p-i-n junctions, using N-doped ZnO as p-type. The LED was structured with stacked ZnO films, with undoped ZnO film (i-ZnO) sandwiched between Ga-doped ZnO (n-type) and N-doped ZnO (p-type) films. In order to obtain high nitrogen concentration, repeated temperature modulation (RTM) was applied to the film, due to the fact that N concentration decreases at steadily high temperature annealing. This work was followed by other groups reporting the fabrication of LEDs using nitrogen as p-type dopant.[82,83] The p-type conductance of nitrogen in ZnO was challenged by Lyons *et al.*[84] using density functional calculation and concluding that the calculated ionization energy of 1.3 eV will denote nitrogen as a deep acceptor, preventing it from contributing to free carrier concentration. To resolve this issue, Liu *et al.*[85] suggested defect complexes which could be considered as shallow donors. Liu *et al.* considered nitrogen substituting oxygen paired with zinc vacancy (N_O–V_{Zn}) and nitrogen substituting zinc paired with oxygen vacancy (N_{Zn}–V_O) as candidates for shallow acceptors, but refuted the N_{Zn}–V_O complex since the complex may easily evolve into N_O–V_{Zn}

complex due to the lower energy of the latter. Yong *et al.*[86] proposed the possibility of hydrogen stabilizing the N_O–V_{Zn} complex, forming N_{Zn}–*m*H–V_O where *m*=1–4 is the number of hydrogen atoms bonding with the N_O–V_{Zn} complex, and estimated an ionization energy of 138 meV for the N_{Zn}–H–V_O complex. Reynolds *et al.*[87] incorporated nitrogen in ZnO film growth *via* organometallic vapor phase epitaxy (OMVPE) and claimed the existence of V_{Zn}–N_O–H^+ complex with approximated ionization energy of 134 meV. In order to achieve stabilized N_O–V_{Zn} complexes, Tang *et al.*[88] implemented tellurium as a co-dopant.

Despite the fact that one of the main carrier-type identification methods used by most researchers is the Hall measurements, it should be noted that this identification method might lead to erroneous results. Ohgaki *et al.*[89]discussed how Hall measurements with a Van der Puaw configuration of non-homogenous n-type ZnO films may lead to an improper carrier-type identification and indicate a "false hole concentration" in the films. The possibility of this improper identification in inhomogeneous samples was later confirmed by theoretical studies of Bierwagen *et al.*[90]

Doping may as well be used to alter the band gap of the host; and band gap engineering has been of interest for various optical and electronic device applications. Magnesium and cadmium have been used to alter the band gap of ZnO, since magnesium oxide (MgO) and cadmium oxide (CdO) are II-VI compound WBGS with 7.8 eV[91] and 2.2 eV[92] band gaps, respectively. Note that the electronegativities of Mg, Zn and Cd on the Pauling scale are 1.31, 1.65 and 1.69, respectively. Makino *et al*[93]. were able to tune ZnO band gap from 3.19 eV to 3.87 eV by achieving $Cd_{0.07}Zn_{0.93}O$ and $Mg_{0.33}ZnO_{0.67}O$ alloys, respectively. They reported an issue with the limited solubility of magnesium and cadmium in ZnO. Das *et al.*[94] used the spray pyrolysis method to fabricate nickel-doped wurtzite ZnO nanofibrous structured thin films. They observed

Ni substituting Zn for concentrations less than 4% and NiO phase was observed in XRD analysis for higher concentrations. They reported obtained data from two methods (optical transmittance and X-ray emission spectroscopy) indicated a decrease in the band gap (up to ~2.9 eV for 15% Ni concentration). The result is compelling since the decrease is not due to the ZnO band gap shifting toward the band gap of NiO. This cubic direct WBGS has a p-type semiconductivity with a band gap in the range of 3.6 to 4 eV [95,96] and the reduction of the Ni-doped ZnO band gap may be attributed to Ni states appearing at the top of the valence band maximum. Ahn *et al.* [97] observed significant optical band gap reduction by doping ZnO with copper *via* reactive rf magnetron sputtering and claimed achieving p-type ZnO. The reduction was in agreement with computational studies of Ferhat *et al.*[98] using density functional theory (DFT) and generalized gradient approximation (GGA). Chen *et al.*[99] also observed the optical band gap reduction in Cu-doped ZnO films, but an increase in the silver-doped ZnO sample was observed. Sernelius *et al.* [100] were able to synthesize heavily n-type aluminum-doped ZnO films (with electron concentration $n = 4.5 \times 10^{20}\ cm^{-3}$ for 2.14 at. % Al concentration) and observe a rise in the optical band gap. They reported band gaps of 3.40, 3.55, 3.79 and 3.90 eV for aluminum atomic percent of 0%, 0.95%, 1.40% and 2.14%, respectively). Similarly, an optical band gap increase of ~0.4 eV was observed in gallium-doped ZnO, deposited by laser molecular beam epitaxy (MBE), as the carrier concentration increased by the group III dopant.[101] Selenium can also be implemented as a group VI dopant, incorporating oxygen vacancies, to tune ZnO band gap. Nenavathu *et al.*[102] measured an increase of 0.2 eV and 0.33 eV for 2 wt% and 5 wt% Se in the band gap of Se-doped ZnO nanoparticles (NPs) synthesized by thermos-mechanical method. As the Se doping concentration increased, a decline in crystal size was observed.

Another use of dopants, altering the band gap, is in high electron mobility field effect transistors (HEMTs), where heterostructures are the fundamental blocks of these types of devices. Heterostructures are formed when two different semiconductors with the same majority carrier type (e.g. n-type) with similar crystal structures but dissimilar band gaps, are in contact, and the difference in the band gaps will cause a band edge offset. Before contact, if the CBM (and the VBM) of one of the semiconductors is lower than (and higher than) the CBM (and the VBM) of the other semiconductor, this "normal" offset causes a band bending at the interface after contact (heterojunction). By engineering the Fermi level on both semiconductors before contact, one can coordinate the lower CBM to bend down toward the global Fermi level after contact in such a way that the Fermi level would be adjacent to the CBM at the interface. In case the Fermi level is increased slightly, it would overcome the CBM at the interface and the electrons would be trapped on the surface forming a 2-dimensional electron gas (2DEG). This surface Tampo *et al.*[103] and Tsukazaki *et al.*[104] separately reported the construction of ZnO/MgZnO heterostructures with MBE. Tampo *et al.* achieved heterostructures with room temperature mobility of 250 $cm^2.V^{-1}.s^{-1}$ and 2750 $cm^2.V^{-1}.s^{-1}$ at 4K with a sheet electron concentration of 10^{13} cm^{-2}. Tsukazaki *et al.* accomplished a highly confined 2DEG and measured mobilities as high as 14,000 $cm^2.V^{-1}.s^{-1}$ at 0.5K. Recently, Falson *et al.*[105] used ozone as an assistant in their MBE-grown ZnO/MgZnO heterostructure to reduce the residual impurity contents of the film in order to achieve exceedingly high electron mobilities (as high as 1,200,000 $cm^2.V^{-1}.s^{-1}$) at extremely low temperatures ($T < 20$ mK). Wang *et al.*[106] investigated the previous claims *via* Monte Carlo method and confirmed the values reported by other researchers.

In a single crystal lattice, the crystal indicates a periodic structure. A hypothetical perfect periodicity occurs only in an ideal situation, however, and this periodicity is perturbed by

irregularities due to inevitable thermal excitations. The dimension of these irregularities may differ. Zero dimensional defects or “point defects” are defects which occur in matters of one or a few atoms. If a certain atom is missing from its location inside the lattice, it creates a “vacancy”. If an atom fills the vacancy by migrating to the vacant site, the vacancy simply switches places with the migrating atom. This type of defect is also known as the Schottky defect. In an ideal single crystal, the atoms are located in places which can be reached by lattice point position vectors. If an atom is misplaced in a position which cannot be reached by a position vector (namely, between the lattice points) it is called an “interstitial” atom. A “Frenkel Pair” or a “Frenkel Defect” occurs when an interstitial atom is placed in the neighborhood of its vacancy. In compound crystals where the lattice is composed of two or more atoms, an “antisite” atom is an atom which is mispositioned at another constituent atom’s position (*e.g.* a carbon atom replacing the silicon atom in a silicon carbide crystal). Whereas the concept of a pure and perfectly periodic crystal is ideal for basic theoretical and computational solid state physics, pure crystal structures are impractical and impurities are type of point defects which may intentionally or unintentionally be introduced into the lattice structure. When impurities are intentionally introduced into a lattice, the process is called “doping”. The “dopant” atom usually replaces a constituent atom and is considered as a “substitutional” defect. If the impurity’s oxidation number matches the oxidation number of the original atom which was expected at that position, the substitution is known as an “isovalent” substitution. On the contrary, if the oxidation number of the original atom differs from the impurity’s oxidation number, an “aliovalent” substitution has occurred. In the latter case, an imbalance may occur and the impurity may be ionized, contributing to the free carrier density of the crystal.

The formation energy of a type of point defect (*e.g.* a vacancy) may differ from another. This is due to the possible charge of the defect. In ZnO, an oxygen vacancy may be neutral in charge or it might be singly or doubly charged. The Fermi level comes into play when the formation energy of a charged defect as $q\epsilon_f$ where q is the charge of the defect and ϵ_f is the Fermi level. Higher dimensional defects may also occur during crystal growth or by physical impacts. This section focuses on point defects in ZnO and the methods used to identify and characterize these defects. Stoichiometric ZnO should be nonconductive as a pure semiconductor. But due to its overt n-type conductivity, it has been long assumed that ZnO conductivity relies on it being either ordinarily nonstoichiometric or containing unintentional impurities during growth. Oxygen deficiency is always a factor in the formation of ZnO single crystals.[107] Although Zn-rich environments result in a more conductive film, insufficient oxygen during film growth may result in mixed phases of metallic Zn and ZnO. Oxygen paucity may result in Zn interstitials (Zn_i) as well as oxygen vacancies (V_O). In earlier studies, researchers considered the oxygen vacancies (V_O) as the intrinsic donors[108] whereas some other researchers believed that the formation of zinc interstitials[109] (Zn_i) and zinc antisites (Zn_O) are the primary sources of the shallow donors in ZnO.

Kobayashi *et al.*[110] computed the band structure energy levels by using the empirical tight-binding approximation. The approximation considers the four nearest-neighbor atoms to be equivalent, despite the crystal structure not being cubic. Bloch-type orbitals and a 4 x 4 Hamiltonian matrix were constructed, where each element of the matrix was a 4 x 4 matrix and the crystal eigenstates were a linear combination of the Bloch-type basis states. In Bloch's theorem, the eigenstates for electrons in a lattice can be expanded in terms of Bloch's waves (a Bloch's wave is a wave which is constructed by the product of a plane wave $e^{-i\vec{k}.\vec{r}}$ and a periodic function $u(\vec{r})$). These matrix elements were calculated by fitting the band structure at certain wave

vectors such as the Γ point. Kobayashi *et al.* stated that the oxygen vacancies as well as zinc antisites may produce shallow donors.

Oba *et al.* used plane-wave pseudopotential method within the generalized gradient approximation (GGA) to calculate the formation energies of different defect types in two extreme conditions: the oxygen-rich limit and the zinc-rich limit. In general, the concentration of a certain defect (C_d) is obtained from Boltzmann's distribution:

$$C_d = N_d \ \exp(-\frac{\Delta G_f}{k_B T})$$

with N_d being the number density of possible defect sites, . k_B being the Boltzmann constant and T being the absolute temperature. ΔG_f is the Gibbs free energy of formation, defined by:

$$\Delta G_f = P\Delta V_f - T\Delta S_f + \Delta E_f$$

where ΔV_f is the change in the system volume after the formation of the defect, P is the absolute pressure and ΔS_f is the change in entropy. ΔE_f is the change in total energy of the system (e.g. a supercell for theoretical calculations), containing the chemical potential terms. Considering that the change in the total energy (ΔE_f) corresponds to the defect formation energy ($\Delta E_{formation}$), the formation energy of a defect in a charge state q may be obtained from:

$$\Delta E_{formation}(q) = E_{tot}(q) - n_{Zn}\mu_{Zn} - n_O\mu_O + q\epsilon_f$$

where n_i is the number of atom specie i in the supercell, μ_i is the atomic chemical potential, ϵ_f is the Fermi level and E_{tot} is the total energy of the supercell. The variables μ_O and μ_{Zn} are correlated as:

$$\mu_O + \mu_{Zn} = \mu_{ZnO(bulk)}$$

In case of a zinc-rich environment $\mu_{Zn} = \mu_{Zn(bulk)}$ and $\mu_O = \mu_{ZnO(bulk)} - \mu_{Zn(bulk)}$; whereas in an oxygen-rich environment $\mu_{Zn} = \mu_{ZnO(bulk)} - \mu_{O(bulk)}$ and $\mu_O = \mu_{O(bulk)}$. Oba *et al.* deduced that zinc antisites and zinc interstitials (tetrahedral site) are the only intrinsic defect types which can explain the n-type conductivity of ZnO, based on the electronic structure, despite the fact that oxygen vacancies, according to their calculations, are the dominant species by having the least formation energy. [111]

Similar to Oba *et al.*'s theoretical approach, Kohan *et al.* applied the plane-wave soft-pseudopotential method and used the density functional theory (DFT) in the local density approximation (LDA) to simplify the many-body electronic system to be able to find the total energies from solving the Schrodinger equation; and concluded that native V_O and V_{Zn} (zinc vacancies) are the dominant crystal defects in a ZnO single crystal in a zinc-rich and an oxygen-rich environment, respectively. Whereas Liu *et al.*[112] had considered Zn_i to be responsible for the green luminescence previously, Kohan *et al.* attributed it to transitions between conduction band minimum (CBM) and the V_{Zn} acceptor levels (2.6 eV) and deducted that the transitions between charged V_O levels may result in visible luminescence as well.[113] It's indispensable to note that the above approximations are notorious for underestimating the band gap and making corrections is inevitable.

Contrastively, Lin *et al.* used full-potential linear muffin-tin approximation to claim the origin of the green luminescence to be from CBM transitions to oxygen antisites (O_{Zn}) rather than transitions to V_{Zn} or V_O.[114] Xu *et al.* suggested transitions from the deep donor complex V_O-Zn_i defects to the valence band maximum (VBM) as a possible candidate.[115]

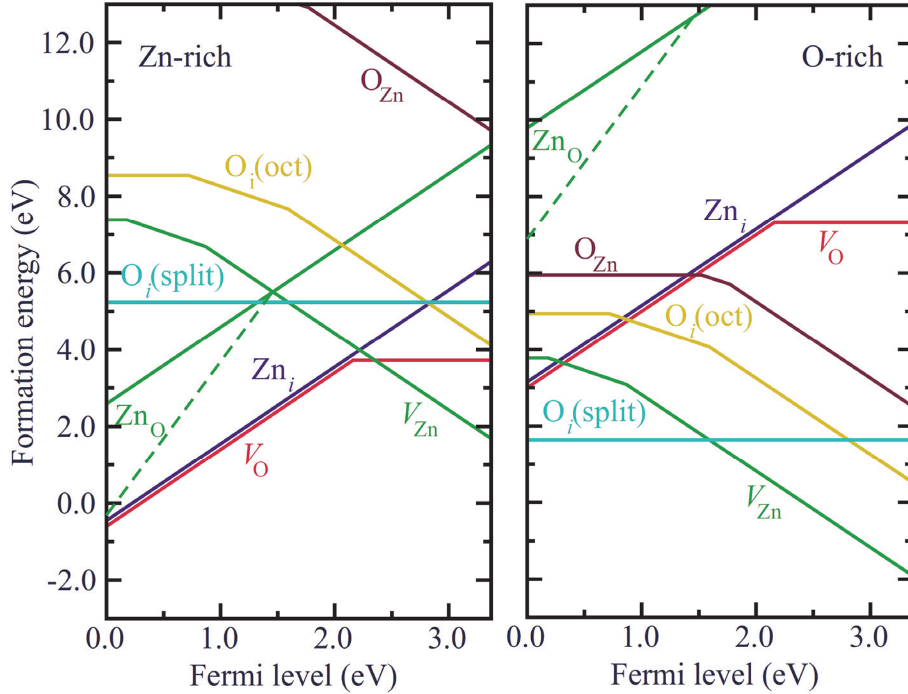

Figure 2.5: Native point-defect formation energies as a function of Fermi level position in zinc-rich (left) and oxygen-rich (right) environments. The lowest-energy charge states are represented on the graph. *Reprinted figure with permission from Anderson Janotti and Chris Van de Walle, Native point defects in ZnO, Physical Review B, 76 (16), p.165202 (2007). Copyright (2007) by the American Physical Society.*

As mentioned before, Van de Walle discussed why native defects cannot primarily contribute to the n-type conductivity and how hydrogen impurities play a significant role as a shallow donor in ZnO, *increasing* the conductivity in contrast with H_2 passivation of other semiconductors. Hydrogen presence is inevitable in most ZnO growth techniques even in ultra-high vacuum methods. Furthermore, in contrast with claims of Zhang *et al.*[116] regarding the low formation enthalpy of Zn_i in Zn-rich and O-rich conditions and the n-type conductivity of ZnO based on the abundance of Zn_i, Janotti and Van de Walle[117] discussed the unlikeliness of the native point defects being the origin of the n-type characteristic of most ZnO crystals by arguing V_O being a rather deep donor and Zn_i having a high formation energy. Despite Zn_i being a shallow donor, according to Janotti and Van de Walle, the formation of Zn_i is high compared to diffusion migration

barriers as low as 0.57 eV; making Zn_i an unstable defect. They provided the formation energy of the point defects as a function of the Fermi level (Figure 2.5). Look *et al.* challenged the claim of Zn_i not being a prominent shallow donor contributor (due to its high formation energy) by presenting the possibility of the formation of complex Zn_i defects according to low temperature photoluminescence and Hall-effect measurements of electron irradiated ZnO. Zn_i is mobile and a potential complex partner is required to stabilize the defect. Nitrogen may substitute for oxygen in case of V_O and form a Zn_i -N_O complex. [118] Look *et al.* also confirmed traces of Al and Ga impurities, contributing to conductivity as background shallow donors, in all of the ZnO samples grown *via* seeded chemical vapor transport (SCVT) method by low temperature photoluminescence. Controversially, Selim *et al.* reported an overall absence of Zn_i in their experiments, even for the Zn-vapor annealed samples, and considered hydrogen atoms situated in oxygen vacancies to be the primary shallow donors.[119] McCluskey and Jokela discussed the possible primary sources of conductivity in an industrially manufactured single crystal ZnO samples by performing secondary ion mass spectrometry (SIMS) and claimed H and group III impurities such as Al, Ga, and B as the primary sources of n-type conductivity in the samples. [120]

Creating p-type ZnO *via* either introducing impurities or creating point defects such as V_{Zn} or O_i is theoretically possible.[121] But due to the low formation enthalpies of "hole killers" as well as the high formation energy of O_i , ZnO cannot become p-type solely depending on native defects (Cross Ref. Zhang).[122] Nitrogen may substitute for oxygen easily in V_O and form a deep acceptor N_O defect.[123] But even then, the p-type behavior may be easily neutralized by inevitable associate hydrogens.[124] A single-hydrogen- defect and two double-hydrogen-defect lines were detected by vibrational spectroscopy on ZnO samples. The former was associated to either interstitial hydrogen (H_i) or H associated with another impurity. The latter were associated with two O-H bonds (one

in parallel with the c-axis and the other one 100^0 away from the c-axis). The double-hydrogen-defect lines are in theoretical agreement with the hydrogenized zinc vacancy ($V_{Zn}H_2$) energy levels.[125]

Interstitial defects such as O_i and Zn_i can be situated in the tetrahedral sites (tet) or the octahedral sites (oct). Denoting d_0 as the Zn-O bond length along the c-axis, a tetrahedral interstitial atom forms bonds with four nearest neighbors (center of a tetrahedron), has a Zn and an O atom as nearest-neighbor with a distance of ~0.833 d_0; whereas an octahedral interstitial atom forms bonds with six equidistant neighbors (three Zn and three O atoms) of length 1.07 d_0.

Hydrogen impurities caused by moisture presence is inevitable in ZnO sol gel fabrication processes. It's crucial to consider the widespread existence of the aforementioned impurities when the characterization of the ZnO layers is concerned. At ambient temperature, water molecules are adsorbed and cannot be fully depleted from ZnO layer surface even with desorption processes. This is due to the positive Gibbs free energy difference of the water molecules adsorbed to the surface.[126] During the sol gel process, moisture may appear on the substrate as well as the semiconductor/semiconductor interface during deposition. The subthreshold swing (SS) measurements suggest defect level creation inside the band gap as a result of oxygen and moisture adsorption.[127]

The oxygen (partial) pressure during growth plays a major role in the defect density near the interface. Lower oxygen pressure increases defects such as dislocations and low-angle grain boundaries.[128] Oxygen vacancy formation is augmented on the surfaces of polar planes (i.e. (0001) and $(000\bar{1})$) of ZnO.[129]

Fu *et al.* reported an intensification of the UV photoluminescence (PL) emission of ZnO-SiO_2 nanocomposites grown *via* sol gel process compared to ZnO. They deduced the formation of

Zn-O-Si bonds at the $ZnO-SiO_2$ interface from the X-ray photoelectron spectroscopy (XPS) and PL spectra and attributed the intensification to both ZnO and $ZnO-SiO_2$.[130]

In comparison to other WBGS, ZnO growth methods are more assorted. A diversity of methods, such as laser induced deposition[131], metalorganic chemical vapor deposition (MOCVD)[132], plasma-enhanced metalorganic chemical vapor deposition (PEMOCVD)[133], vapor phase epitaxy (VPE)[134], atomic layer deposition (ALD)[135], plasma-enhanced atomic layer deposition (PEALD)[136], have been utilized in order to grow ZnO on various substrates. Whereas relatively large single crystal ZnO substrates are attainable[137], polycrystalline and amorphous films and nanostructures are frequent and affordable. The following section aims to provide a brief insight on the synthesis methods of ZnO structures.

Hydrothermal synthesis was one the early methods to be used to grow ZnO crystals. In this method, a supersaturated solution along with its nutrient is placed inside an autoclave, a vessel which can contain high temperature and pressure. By tuning the temperature, crystallization occurs. Laudise *et al.* achieved single crystal ZnO *via* hydrothermal growth process.[138]

Molecular beam epitaxy (MBE) is another growth method for single crystal ZnO. During epitaxial growth, reflected high energy electron diffraction (RHEED) analysis is implemented simultaneously to monitor the growth process. Johnson *et al.* claimed the fabrication of ZnO heterointerfaces *via* MBE with an electron mobility of 260 $cm^2.V^{-1}.s^{-1}$. The ZnO layer indicated an n-type carrier concentration of 9×10^{18} cm^{-3}, and ohmic behavior was observed across the ZnO/GaN and SiC/ZnO heterointerfaces.[139] Later, Ogata *et al.* used metalorganic vapor-phase epitaxy (MOVPE) to deposit high quality ZnO layers on ZnO/Si and ZnO/Sapphire substrates grown by MBE.[140]

In the spray pyrolysis method, thin films will be formed when a solution is sprayed upon a heated surface. Upon contact, chemical reactions may occur and other constituents may evaporate. Aranovich *et al.*[141] investigated the electrical, optical and thermoelectrical properties of ZnO thin films deposited *via* spray pyrolysis. The group used aqueous solutions of zinc dichloride plus hydrogen peroxide and zinc acetate.

Li *et al.*[142] synthesized ZnO nanowires on copper coated silicon (100) substrate *via* vapor-liquid-solid process. The nanowires were mainly (0002) oriented but a tinge of (1000) orientation was also observed. Matsumoto *et al.*[143] reported the growth of single crystals of ZnO *via* vapor transport deposition (VTD) when Zn or $ZnCl_2$ were used as transport agents whereas Huang *et al.*[144] reported the formation of crystalline nanowires using gold as a catalyst.

Pulsed laser deposition (PLD) was utilized to study the piezoelectric properties of textured ZnO coated nanofibers.[145] Izaki *et al.* deposited micrometer-thick ZnO films cathodically from aqueous zinc nitrate electrolyte. The electrochemical grown film indicated an optical band gap of 3.3 eV.[146] Quantum sized ZnO particles were synthesized *via* electrophoretic deposition from colloidal suspension of ZnO. The particles were several nanometers wide in diameter and the particle size could be tuned by the change in aging time or growth temperature. Due to quantum confinement, blue shift was observed in photoluminescence and the shift could be controlled by the particle size.[147] Milimeter-long nanobelts (nanoribbons) were synthesized *via* thermal evaporation of the metal oxide by Pan *et al*. The nanostructures were single crystalline and the diameter of the belts ranged from 30 to 300nm.[148]

Chemical vapor deposition (CVD) process and its derivatives, such as MOCVD and PEMOCVD, are often utilized to fabricate ZnO films. Tiku *et al.*[149] achieved $(11\bar{\bar{2}}0)$ ZnO films on $(01\bar{1}2)$ sapphire at a substrate temperature of 700C using the reaction of Zn vapor and CO_2 and

later, Minegishi *et al.*[150] claimed to have synthesized p-type ZnO for the very first time *via* CVD. Claims over fabrication of p-type ZnO have been challenged regularly by peer researchers and the issue is still controversial. Kim *et al.* investigated the trapped oxygen in the grain boundaries of plasma-enhanced chemical vapor deposition (PECVD) grown polycrystalline ZnO. They observed a deviation of stoichiometry of the crystalline thin films, with a higher oxygen quantity.[151]

Sputtering is a common and straightforward method to deposit films. Direct-current reactive magnetron sputtering (dc-RMS) has been used by various groups, with different $Ar:O_2$ ratios. Singh *et al.* observed an increase in the grain size when the oxygen total or partial pressure was increased. The paucity of total oxygen in the lowest overall pressure and the lowest oxygen ratio resulted in a mixed phase of Zn and randomly oriented grains of nanocrystalline (NC) ZnO. Otherwise, single-phase highly c-axis oriented ZnO films were observed.[152] Kannan *et al*. used dc-RMS to fabricate stable humidity sensors. The resistivity of the NC-ZnO changed 4 orders of magnitude from 6.3% to 84% with change in relative humidity (RH). The grains of NC-ZnO were distorted and randomly oriented.[153] Suchea *et al.* used dc-RMS (with Zn target) and dc-MS (with ZnO target) to realize NC-ZnO at room temperature. Decrease of oxygen concentration resulted in a significant compressive stress in the film synthesized using the metallic target.[154] Fortunato *et al*. obtained highly stoichiometric, hence resistive ZnO films containing small and dense NC-ZnO with sputtering power density manipulation in radio-frequency magnetron sputtering (rf-MS).[155] Kumar *et al.* have observed an increase in crystallinity in c-axis orientation of the film with increasing substrate's temperature while sputtering.[156] This is in agreement with Mandal *et al*.'s work. Both groups have observed a red shift of the band gap of the samples, and the relaxation of the NC-ZnO at higher substrate temperatures.[157] The dc magnetron sputtering (dc-MS) was used by Fang *et al.* for the deposition of conductive Al-doped ZnO thin films. Annealing the film in

vacuum resulted in the reduction of oxygen atomic ratio and a higher carrier concentration, whereas re-annealing the sample in an ambient air restored the stoichiometry, equalized the surface and decreased the mean grain size.[158] Yang *et al*. deposited Al-doped NC-ZnO *via* rf-MS and reported an increase in grain size when the deposition power was raised.[159] Li *et al*. used dc-RMS (with Zn target) and dc-MS (with ZnO:3wt%Al_2O_3 target) to grow ZnO and Al-doped ZnO thin films. No metallic Zn or Al_2O_3 peaks were observed in XRD patterns while the intensities of the peaks for ZAO were an order of magnitude larger than ZnO peaks. However, the ZAO films indicated more strain and more roughness compared to the ZnO samples. Strain decreased with the substrate temperature being increased during deposition. However, the grain size of NC-ZnO did not change significantly.[160] Lee *et al*. have made a comprehensive comparative study for deposition of NC-ZnO using dc and rf magnetron sputtering with argon or argon/oxygen mixture. They found that the films deposited by rf magnetron sputtering exhibit lower resistivity than the one by dc magnetron sputtering. It was conjectured that grain boundary scattering is the major mechanism for reducing carrier mobility, thus the electrical conductivity.[161]

Solution process is a cost effective synthesis method which can be executed in the ambient temperature. Contrary to many methods which require low pressure, solution process can be realized in the atmospheric pressure. Bahnemann *et al.* synthesized colloidal ZnO suspensions in water, acetonitrile and 2-propanol. The ZnO sol contained transparent colloidal spherically – shaped particles with diameters in the range of 50Å. During particle growth, quantum confinement was observed due to the size of the particles being in the Angstrom range. After the final stage, particles contained 2000~3000 ZnO molecules and indicated many photophysical properties of bulk ZnO.[162]

Delving briefly into the history of semiconductor devices and field effect transistors, Howard[163] argues that patents of Lilienfeld (1934) and Heil (1935) indicate the first relevant structures of a field effect device, but lack a comprehensive understanding of the key aspects and the operation of semiconductors in these then-advanced devices. Shockley (1939) on the other hand, Howard conveys, discusses the depletion of the metal-semiconductor contact region from charge carriers and presents an appreciation of the switching capability of his structure (representing the first metal-semiconductor field effect transistor or MESFET) and should be considered as the first researcher who has invented the concept of field effect devices. Shockley, Bardeen and Brattain, at Bell Telephone Laboratories, collaborated on invention, enhancement and exploration of the first functioning transistor in early 1946.[164] Bipolar junction transistors (BJTs) were first developed by Teal *et al.*[165]in 1951 and were one of the most successful electronic devices in terms of efficiency and fabrication cost for decades to come. Nonetheless, the necessity of size reduction and power consumption in transistors limits the use of BJTs in processing applications and electronic displays. As researchers strived to remain allegiant to Gordon Moore's prediction of larger integrated circuits being crammed on a chip in years to come (also known as the Moore's Law)[166], the semiconductor-related characteristics such as device size, fabrication expenses, industry revenue, and processing speed remained semi-linear when plotted on a semi-log scale vs. each technology generation (which spans two to three years).[167,168,169] Field effect transistors (FETs), specially metal-oxide-semiconductor field effect transistors (MOSFETs) alleviated the plight of BJTs' limitations, *e.g.* their low-power operation restriction was attenuated by introducing insulating dielectrics into the structure. As a result, MOSFETs are widely employed in modern electronics and state-of-the-art devices embody FETs for different applications. Non-toxicity and direct wide band gap of ZnO has further enhanced the use of field effect devices in

broad organic/inorganic applications and contemporary interdisciplinary studies on topics such as nanogenerators[170], nanopiezotronics[171] and nanosized gas-sensors[172], bio-sensors[173] and ion-sensors[174] indicate the significance of this semiconductor. Thin film transistors (TFTs) are field effect devices which have extensive applications in large area display electronics such as organic light emitting diodes (OLEDs) and liquid crystal displays (LCD), flexible electronics, switching devices, and logic circuits. Worldwide revenue of TFT LCD industry has increased from $1B in 1989 to $110B in 2012.[175]

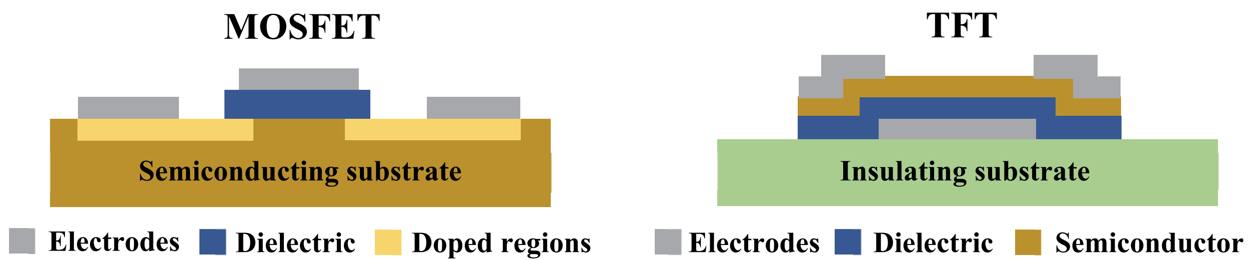

Figure 2.6: Cross-section schematics of typical MOSFETs and TFTs.

Despite fundamental similarities between TFTs and MOSFETs, such as the number of terminals and modulation of conductivity by gate and body voltage biases, several differences exist. One of the main differences between TFTs and MOSFETs is their device structures (Figure 2.6). In basic MOSFETs, oppositely doped semiconductors are applied in order to fabricate a device with controlled functionality *via* a gate contact voltage bias. Since the semiconductor body is not conductive without a gate bias (normally off), the device it is referred to as an enhancement-mode device (non-zero gate bias required for conduction). Whereas the active semiconductor body is doped with either donors (n-type) or acceptors (p-type), source and drain contact regions are heavily doped with opposite type dopants. For an accessible comparison, a MOSFET with p-type semiconductor body and n-type source and drain contacts is considered, namely an n-MOSFET.

The contrast of the carrier types prevents conduction from source to drain (n-type) through the semiconductor body (p-type). When a positive gate-source voltage bias (V_{GS}) is applied, the positively charged carriers in the p-type semiconductor body are repelled and a depletion region is formed under the gate oxide of the MOSFET. As V_{GS} increases, the minority charge carriers (negatively charged carriers) are drawn towards the gate. When V_{GS} reaches a certain limit (threshold voltage), a layer filled with minority carriers is formed (inversion layer) under the gate oxide region and source-to-drain conduction is achieved through the inversion layer carriers. As a result, the n-MOSFET can be turned on if V_{GS} higher than the threshold voltage (V_{TH}) is applied. In basic TFTs, however, the same semiconductor body with a certain carrier type covers the regions under the source and drain metallic contacts and the gate oxide. In case of a heavily n-type doped TFT, the semiconductor body is conductive when $V_{GS} = 0$ (normally on) and the device it is referred to as a depletion-mode device (non-zero gate bias required for charge carrier depletion). If negative V_{GS} is applied, the carriers are repelled from the gate oxide and with V_{GS} below the V_{TH}, they will be depleted from the semiconductor body. Consequently, the TFT will be turned off if a V_{GS} lower than V_{TH} is applied.

The aforementioned basic ideal enhancement-mode n-MOSFET contains three conditions, referred to as accumulation ($V_{GS} < 0$), depletion ($0 < V_{GS} < V_{TH}$) and inversion ($V_{TH} < V_{GS}$) conditions; whereas the basic ideal heavily n-type depletion-mode TFT has two conditions: depletion ($V_{GS} < V_{TH}$) and accumulation ($V_{TH} < V_{GS}$). And since ZnO is intrinsically heavily n-type, ZnO TFTs are mainly of the depletion-mode type transistors.

Another distinction between TFTs and MOSFETs is the crystal size and quality of the semiconductors employed in fabrication processes. Conventionally, MOSFETs contain doped single crystal semiconductors and are fabricated on high quality substrates; TFTs predominantly

embody amorphous or polycrystalline semiconductors and they can be fabricated on various substrates since amorphous or polycrystalline structures are usually substrate-insensitive, causing TFTs perfect for large area electronics.[176] ZnO TFT fabrications have been reported on numerous gate dielectrics substrates such as silicon dioxide (SiO_2)[177], silicon nitride (SiN_x)[178], hafnium dioxide (HfO_2), hafnium silicon oxide ($HfSiO_x$)[179], aluminum oxide (Al_2O_3)[180], Al_2O_3 and TiO_2 superlattice (ATO)[181], some reported achieving transparent devices. This exhibits the exceptional versatility of ZnO in comparison to other competitive direct wide bang gap semiconductors such as GaN and SiC which require fine lattice matching, sometimes *via* buffer layers, during growth. The downside to ZnO TFTs is the mediocre channel mobility in these devices. Reports indicate the channel mobility dependence on substrate quality[182] and since crystal orientation greatly influences channel mobility, annealing temperature plays a major role in device enhancement.[183]

Table 2.4 lists the characteristics of ZnO TFTs reported by various groups[184] and compares them with the values obtained from the fabricated ZnO TFT in this dissertation, the 8L sample. In the preparation of the 8L sample, the spin-coating process was performed 8 times, resulting in a thin film containing 8 layers of ZnO with total thickness of approximately 190 microns.

Table 2.4 Comparison of ZnO TFT characteristics, deposited *via* different methods.

Deposition technique	Temperature (°C)	Channel mobility ($cm^2.V^{-1}.s^{-1}$)	On/off ratio	V_{TH} (V)	I_{Sat} (μA)
Ion beam [185]	600–800	0.3–2.5	10^6	10 to 20	70
Sol gel [186]	700	0.2	10^7	N/A	14
Pulsed laser [187]	450	0.031–0.97	10^6	1.0 to 2.5	80
rf magnetron sputtering [188]	room temperature	20–70	$5x10^5$	1.8	1000
This work (8L)	800	0.58	10^7	-34.5	86

In order to prepare ZnO TFTs, ZnO layers are first deposited *via* the sol-gel spin-coating method. A precursor is prepared, spin coated on a substrate and spin coated at 3000 rpm for 30 s. Then the substrate is calcined on a hotplate, at approximately 300 ºC for 5 minutes, to evaporate the solvents in the precursor. The process is repeated until the desired thickness is achieved. Eventually, the deposited film is annealed in an oven in ambient for an hour, to achieve a nanocrystalline ZnO thin film. Figure 2.7 shows the flow diagram for this process.

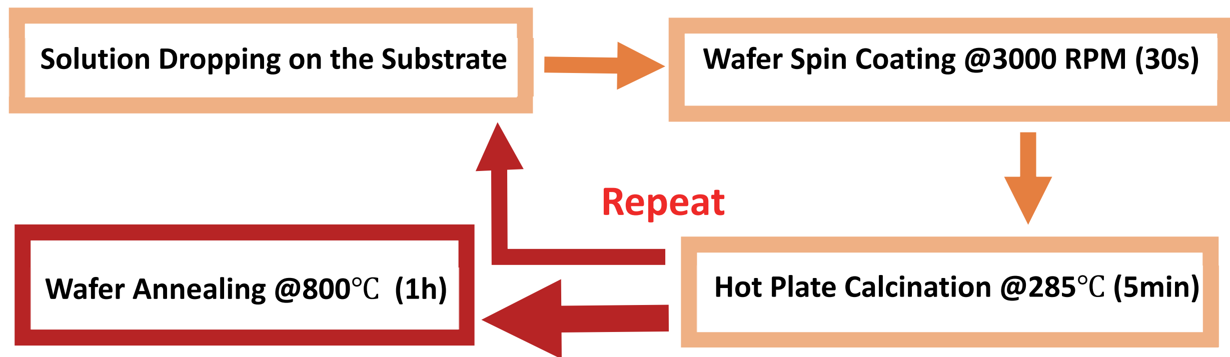

Figure 2.7: Flow diagram of the sol-gel deposition process.

Afterwards, the metallic contact is deposited on the film to form the transistor terminals. To do so, photolithography is realized by spin-coating photoresist on the film, followed by soft baking at 100 °C for 30 seconds. Then, the sample is exposed to the UV light through a mask blocking parts of the UV light. The photoresist exposed to the UV becomes solvable in the developer solution. However, if the inverse of the mask is intended for the pattern, reverse photolithography is achieved by the supplementary steps of baking the substrate again and exposing the whole sample to the UV light (flood UV exposure). The sample is then developed, and the solvable photoresist is removed, leaving the desired pattern. The metallic contacts can then be deposited. In this experiment, metal deposition was realized by a homemade DC magnetron

sputtering system in which the sample is put inside a closed chamber and the air is pumped out *via* a high vacuum pump. The chamber is then filled with the noble gas argon. For the sputtering process to occur, the argon atoms are ionized, and voltage bias is applied to the metal “targets” desired to be sputtered on the sample. The argon ions obtain energy by accelerating towards the metallic target. The collision of argon ions with the target causes the atoms to be sputtering off of the target and be deposited on the sample above the target. After metal deposition, the sample is put in acetone for the lift-off process in which the patterned photoresist is solved and etched away from the sample. As a result, the inverse of the photoresist pattern, containing no photoresist, retains the metal due to metal adhesion to substrate’s surface. Figure 2.8 shows the flow diagram for the reverse photolithography process.

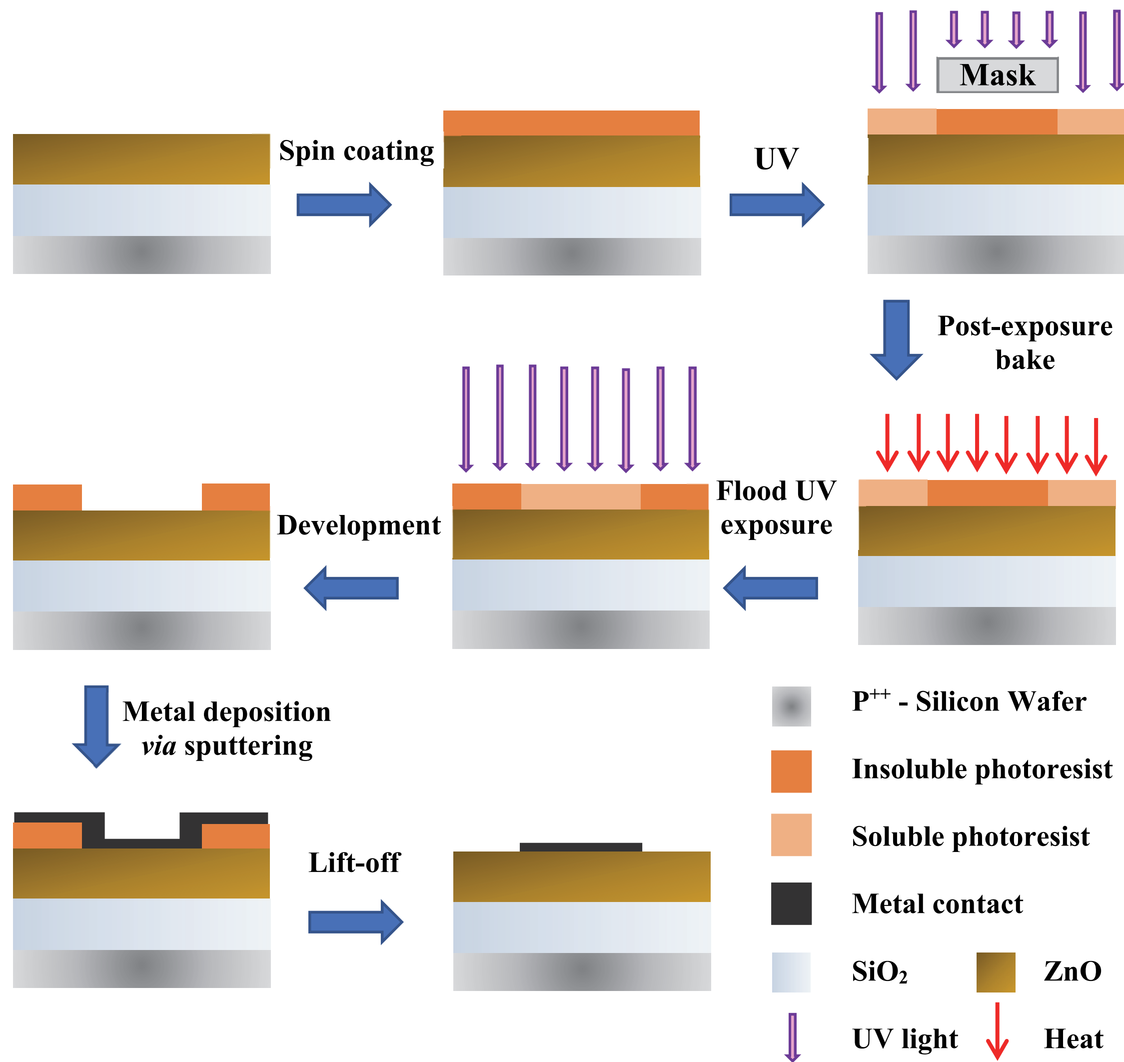

Figure 2.8 Flow diagram for the reverse photolithography process.

References

[1] Chen, Y., Bagnall, D.M., Koh, H.J., Park, K.T., Hiraga, K., Zhu, Z. and Yao, T., 1998. Plasma assisted molecular beam epitaxy of ZnO on c-plane sapphire: growth and characterization. Journal of Applied Physics, 84(7), pp.3912-3918.

[2] Harris, Gary Lynn, ed. Properties of silicon carbide. No. 13. Iet, 1995. p.31.

[3] Gil, Bernard, ed. III-nitride semiconductors and their modern devices. Vol. 18. OUP Oxford, 2013.

[4] Huang, M.H., Mao, S., Feick, H., Yan, H., Wu, Y., Kind, H., Weber, E., Russo, R. and Yang, P., 2001. Room-temperature ultraviolet nanowire nanolasers. science, 292(5523), pp.1897-1899.

[5] Look, D.C., 2001. Recent advances in ZnO materials and devices. Materials Science and Engineering: B, 80(1), pp.383-387.

[6] Pearton, S.J., Norton, D.P., Ip, K., Heo, Y.W. and Steiner, T., 2005. Recent progress in processing and properties of ZnO. Progress in materials science, 50(3), pp.293-340.

[7] Özgür, Ü., Alivov, Y.I., Liu, C., Teke, A., Reshchikov, M., Doğan, S., Avrutin, V.C.S.J., Cho, S.J. and Morkoc, H., 2005. A comprehensive review of ZnO materials and devices. Journal of applied physics, 98(4)

[8] Carlotti, G., Socino, G., Petri, A. and Verona, E., 1987. Acoustic investigation of the elastic properties of ZnO films. Applied Physics Letters, 51(23), pp.1889-1891.

[9] Karzel, H., Potzel, W., Köfferlein, M., Schiessl, W., Steiner, M., Hiller, U., Kalvius, G.M., Mitchell, D.W., Das, T.P., Blaha, P. and Schwarz, K., 1996. Lattice dynamics and hyperfine interactions in ZnO and ZnSe at high external pressures. Physical Review B, 53(17), p.11425.

[10] Kucheyev, S.O., Bradby, J.E., Williams, J.S., Jagadish, C. and Swain, M.V., 2002. Mechanical deformation of single-crystal ZnO. Applied Physics Letters, 80(6), pp.956-958.

[11] Gil, B., 2014. Physics of Wurtzite Nitrides and Oxides. Springer International Publishing, Cham, p. 15.

[12] Kisi, E.H. and Elcombe, M.M., 1989. u parameters for the wurtzite structure of ZnS and ZnO using powder neutron diffraction. Acta Crystallographica Section C: Crystal Structure Communications, 45(12), pp.1867-1870.

[13] Gerward, L. and Olsen, J.S., 1995. The high-pressure phase of zincite. Journal of Synchrotron radiation, 2(5), pp.233-235.

[14] Momma, K. and Izumi, F., 2011. VESTA 3 for three-dimensional visualization of crystal, volumetric and morphology data. Journal of Applied Crystallography, 44(6), pp.1272-1276.

[15] Heiland, G. and Ibach, H., 1966. Pyroelectricity of zinc oxide. Solid State Communications, 4(7), pp.353-356.

[16] Hutson, A.R., 1960. Piezoelectricity and conductivity in ZnO and CdS. Physical Review Letters, 4(10), p.505.

[17] Fujimura, N., Nishihara, T., Goto, S., Xu, J., & Ito, T. (1993). Control of preferred orientation for ZnOx films: control of self-texture. Journal of Crystal Growth, 130(1-2), 269-279.

[18] Jin, B.J., Im, S. and Lee, S.Y., 2000. Violet and UV luminescence emitted from ZnO thin films grown on sapphire by pulsed laser deposition. Thin Solid Films, 366(1), pp.107-110.

[19] Liu, H., Tse, J.S. and Mao, H.K., 2006. Stability of rocksalt phase of zinc oxide under strong compression: Synchrotron x-ray diffraction experiments and first-principles calculation studies. Journal of applied physics, 100(9), pp.93509-93509.

[20] Jaffe, J.E. and Hess, A.C., 1993. Hartree-Fock study of phase changes in ZnO at high pressure. Physical Review B, 48(11), p.7903.

[21] Jaffe, J.E., Snyder, J.A., Lin, Z. and Hess, A.C., 2000. LDA and GGA calculations for high-pressure phase transitions in ZnO and MgO. Physical Review B, 62(3), p.1660.

[22] L.-G. Liu and W. A. Bassett, Elements, Oxides, and Silicates: High-Pressure Phases with Implications for the Earth's Interior. Oxford University, New York, 1986.

[23] CRC Handbook of Chemistry and Physics, 58th ed. CRC, Boca Raton, 1977.

[24] Varshni, Y.P., 1967. Temperature dependence of the energy gap in semiconductors. physica, 34(1), pp.149-154.

[25] Wang, L. and Giles, N.C., 2003. Temperature dependence of the free-exciton transition energy in zinc oxide by photoluminescence excitation spectroscopy. Journal of Applied Physics, 94(2), pp.973-978.

[26] Birman, J.L., 1959. Polarization of fluorescence in CdS and ZnS single crystals. Physical Review Letters, 2(4), p.157.

[27] Thomas, D.G., 1960. The exciton spectrum of zinc oxide. Journal of Physics and Chemistry of Solids, 15(1-2), pp.86-96.

[28] Rössler, U., 1969. Energy bands of hexagonal II-VI semiconductors. Physical Review, 184(3), p.733.

[29] Rowe, J.E., Cardona, M. and Pollak, F.H., 1968. Valence band symmetry and deformation potentials of ZnO. Solid State Communications, 6(4), pp.239-242.

[30] Liang, W.Y. and Yoffe, A.D., 1968. Transmission spectra of ZnO single crystals. Physical Review Letters, 20(2), p.59.

[31] Hopfdeld, J.J., 1960. Fine structure in the optical absorption edge of anisotropic crystals. Journal of Physics and Chemistry of Solids, 15(1), pp.97-107.

[32] Reynolds, D.C., Look, D.C., Jogai, B., Litton, C.W., Cantwell, G. and Harsch, W.C., 1999. Valence-band ordering in ZnO. Physical Review B, 60(4), p.2340.

[33] Lambrecht, W.R., Rodina, A.V., Limpijumnong, S., Segall, B. and Meyer, B.K., 2002. Valence-band ordering and magneto-optic exciton fine structure in ZnO. Physical review B, 65(7), p.075207.

[34] Schröer, P., Krüger, P. and Pollmann, J., 1993. First-principles calculation of the electronic structure of the wurtzite semiconductors ZnO and ZnS. Physical Review B, 47(12), p.6971.

[35] Vogel, D., Krüger, P. and Pollmann, J., 1995. Ab initio electronic-structure calculations for II-VI semiconductors using self-interaction-corrected pseudopotentials. Physical Review B, 52(20), p.R14316.

[36] Shih, B.C., Xue, Y., Zhang, P., Cohen, M.L. and Louie, S.G., 2010. Quasiparticle band gap of ZnO: High accuracy from the conventional G 0 W 0 approach. Physical review letters, 105(14), p.146401.

[37] Hedin, L., 1965. New method for calculating the one-particle Green's function with application to the electron-gas problem. Physical Review, 139(3A), p.A796.

[38] Hybertsen, M.S. and Louie, S.G., 1986. Electron correlation in semiconductors and insulators: Band gaps and quasiparticle energies. Physical Review B, 34(8), p.5390.

[39] Ochi, M., Arita, R. and Tsuneyuki, S., 2017. Correlated Band Structure of a Transition Metal Oxide ZnO Obtained from a Many-Body Wave Function Theory. Physical Review Letters, 118(2), p.026402.

[40] Usuda, M., Hamada, N., Kotani, T. and van Schilfgaarde, M., 2002. All-electron GW calculation based on the LAPW method: Application to wurtzite ZnO. Physical Review B, 66(12), p.125101.

[41] Yu, J., Wagner, L.K. and Ertekin, E., 2015. Towards a systematic assessment of errors in diffusion Monte Carlo calculations of semiconductors: Case study of zinc selenide and zinc oxide. The Journal of chemical physics, 143(22), p.224707.

[42] Zwicker, G. and Jacobi, K., 1985. Experimental band structure of ZnO. Solid state communications, 54(8), pp.701-704.

[43] Numerical Data and Functional Relationships in Science and Technology, edited by K. H. Hellwege and O. Madelung, Landolt-Börnstein, New Series, Group III, Vols. 17a and 22a (Springer, Berlin, 1982)

[44] Ley, L., Pollak, R.A., McFeely, F.R., Kowalczyk, S.P. and Shirley, D.A., 1974. Total valence-band densities of states of III-V and II-VI compounds from x-ray photoemission spectroscopy. Physical Review B, 9(2), p.600.

[45] Minami, T., Nanto, H. and Takata, S., 1984. Highly conductive and transparent aluminum doped zinc oxide thin films prepared by RF magnetron sputtering. Japanese Journal of Applied Physics, 23(5A), p.L280.

[46] Minami, T., Sato, H., Nanto, H. and Takata, S., 1985. Group III impurity doped zinc oxide thin films prepared by RF magnetron sputtering. Japanese Journal of Applied Physics, 24(10A), p.L781.

[47] Hu, J. and Gordon, R.G., 1991. Textured fluorine-doped ZnO films by atmospheric pressure chemical vapor deposition and their use in amorphous silicon solar cells. Solar cells, 30(1-4), pp.437-450.

[48] Mollwo, E., 1954. Die wirkung von wasserstoff auf die leitfähigkeit und lumineszenz von zinkoxydkristallen. Zeitschrift für Physik A Hadrons and Nuclei, 138(3), pp.478-488.

[49] Thomas, D.G. and Lander, J.J., 1956. Hydrogen as a donor in zinc oxide. The Journal of Chemical Physics, 25(6), pp.1136-1142.

[50] Van de Walle, C.G., 2000. Hydrogen as a cause of doping in zinc oxide. Physical review letters, 85(5), p.1012.

[51] Park, S.Y., Kim, B.J., Kim, K., Kang, M.S., Lim, K.H., Lee, T.I., Myoung, J.M., Baik, H.K., Cho, J.H. and Kim, Y.S., 2012. Low-Temperature, Solution-Processed and Alkali Metal Doped ZnO for High-Performance Thin-Film Transistors. Advanced Materials, 24(6), pp.834-838.

[52] Park, C.H., Zhang, S.B. and Wei, S.H., 2002. Origin of p-type doping difficulty in ZnO: The impurity perspective. Physical Review B, 66(7), p.073202.

[53] Aven, M., in II-VI Semiconducting Compounds edited by D.G. Thomas (Benjamin, New York, 1967), p. 1232.

[54] Ryu, Y.R., Kim, W.J. and White, H.W., 2000. Fabrication of homostructural ZnO p–n junctions. Journal of Crystal growth, 219(4), pp.419-422.

[55] Lander, J.J., 1960. Reactions of lithium as a donor and an acceptor in ZnO. Journal of Physics and Chemistry of Solids, 15(3-4), pp.324-334.

[56] Wardle, M.G., Goss, J.P. and Briddon, P.R., 2005. Theory of Li in ZnO: A limitation for Li-based p-type doping. Physical Review B, 71(15), p.155205.

[57] Zeng, Y.J., Ye, Z.Z., Xu, W.Z., Li, D.Y., Lu, J.G., Zhu, L.P. and Zhao, B.H., 2006. Dopant source choice for formation of p-type ZnO: Li acceptor. Applied Physics Letters, 88(6), p.062107.

[58] Lee, J., Cha, S., Kim, J., Nam, H., Lee, S., Ko, W., Wang, K.L., Park, J. and Hong, J., 2011. p-Type Conduction Characteristics of Lithium-Doped ZnO Nanowires. Advanced materials, 23(36), pp.4183-4187.

[59] Shin, S.H., Kim, Y.H., Lee, M.H., Jung, J.Y., Seol, J.H. and Nah, J., 2014. Lithium-Doped Zinc Oxide Nanowires–Polymer Composite for High Performance Flexible Piezoelectric Nanogenerator. ACS nano, 8(10), pp.10844-10850.

[60] Lin, S.S., Lu, J.G., Ye, Z.Z., He, H.P., Gu, X.Q., Chen, L.X., Huang, J.Y. and Zhao, B.H., 2008. p-type behavior in Na-doped ZnO films and ZnO homojunction light-emitting diodes. Solid State Communications, 148(1), pp.25-28.

[61] Dietz, R.E., Kamimura, H., Sturge, M.D. and Yariv, A., 1963. Electronic structure of copper impurities in ZnO. Physical Review, 132(4), p.1559.

[62] Dingle, R., 1969. Luminescent transitions associated with divalent copper impurities and the green emission from semiconducting zinc oxide. Physical Review Letters, 23(11), p.579.

[63] Muller, G., 1976. Optical and electrical spectroscopy of zinc oxide crystals simultaneously doped with copper and donors. physica status solidi (b), 76(2), pp.525-532.

[64] Hou, D.L., Ye, X.J., Meng, H.J., Zhou, H.J., Li, X.L., Zhen, C.M. and Tang, G.D., 2007. Magnetic properties of n-type Cu-doped ZnO thin films. Applied Physics Letters, 90(14), p.142502.

[65] Buchholz, D.B., Chang, R.P.H., Song, J.Y. and Ketterson, J.B., 2005. Room-temperature ferromagnetism in Cu-doped ZnO thin films. Applied Physics Letters, 87(8), p.082504.

[66] Tiwari, A., Snure, M., Kumar, D. and Abiade, J.T., 2008. Ferromagnetism in Cu-doped ZnO films: Role of charge carriers. Applied Physics Letters, 92(6), p.062509.

[67] Shukla, G., 2009. Magnetic and optical properties of epitaxial n-type Cu-doped ZnO thin films deposited on sapphire substrates. Applied Physics A: Materials Science & Processing, 97(1), pp.115-118.

[68] Kobayashi, A., Sankey, O.F. and Dow, J.D., 1983. Deep energy levels of defects in the wurtzite semiconductors AlN, CdS, CdSe, ZnS, and ZnO. Physical Review B, 28(2), p.946.

[69] Park, C.H., Zhang, S.B. and Wei, S.H., 2002. Origin of p-type doping difficulty in ZnO: The impurity perspective. Physical Review B, 66(7), p.073202.

[70] Aoki, T., Hatanaka, Y. and Look, D.C., 2000. ZnO diode fabricated by excimer-laser doping. Applied Physics Letters, 76(22), pp.3257-3258

[71] Kim, K.K., Kim, H.S., Hwang, D.K., Lim, J.H. and Park, S.J., 2003. Realization of p-type ZnO thin films via phosphorus doping and thermal activation of the dopant. Applied Physics Letters, 83(1), pp.63-65.

[72] Ryu, Y.R., Zhu, S., Look, D.C., Wrobel, J.M., Jeong, H.M. and White, H.W., 2000. Synthesis of p-type ZnO films. Journal of Crystal Growth, 216(1), pp.330-334.

[73] Ryu, Y.R., Lee, T.S. and White, H.W., 2003. Properties of arsenic-doped p-type ZnO grown by hybrid beam deposition. Applied Physics Letters, 83(1), pp.87-89.

[74] Xiu, F.X., Yang, Z., Mandalapu, L.J., Zhao, D.T., Liu, J.L. and Beyermann, W.P., 2005. High-mobility Sb-doped p-type ZnO by molecular-beam epitaxy. Applied Physics Letters, 87(15), p.152101.

[75] Chu, S., Lim, J.H., Mandalapu, L.J., Yang, Z., Li, L. and Liu, J.L., 2008. Sb-doped p-Zn O/ Ga-doped n-Zn O homojunction ultraviolet light emitting diodes. Applied Physics Letters, 92(15), p.152103.

[76] Limpijumnong, S., Zhang, S.B., Wei, S.H. and Park, C.H., 2004. Doping by large-size-mismatched impurities: the microscopic origin of arsenic-or antimony-doped p-type zinc oxide. Physical review letters, 92(15), p.155504.

[77] Sato, Y. and Sato, S., 1996. Preparation and some properties of nitrogen-mixed ZnO thin films. Thin Solid Films, 281, pp.445-448.

[78] Minegishi, K., Koiwai, Y., Kikuchi, Y., Yano, K., Kasuga, M. and Shimizu, A., 1997. Growth of p-type zinc oxide films by chemical vapor deposition. Japanese Journal of Applied Physics, 36(11A), p.L1453.

[79] Joseph, M., Tabata, H. and Kawai, T., 1999. p-type electrical conduction in ZnO thin films by Ga and N codoping. Japanese Journal of Applied Physics, 38(11A), p.L1205.

[80] Look, D.C., Reynolds, D.C., Litton, C.W., Jones, R.L., Eason, D.B. and Cantwell, G., 2002. Characterization of homoepitaxial p-type ZnO grown by molecular beam epitaxy. Applied physics letters, 81(10), pp.1830-1832.

[81] Tsukazaki, A., Ohtomo, A., Onuma, T., Ohtani, M., Makino, T., Sumiya, M., Ohtani, K., Chichibu, S.F., Fuke, S., Segawa, Y. and Ohno, H., 2005. Repeated temperature modulation epitaxy for p-type doping and light-emitting diode based on ZnO. Nature materials, 4(1), p.42.

[82] Jiao, S.J., Zhang, Z.Z., Lu, Y.M., Shen, D.Z., Yao, B., Zhang, J.Y., Li, B.H., Zhao, D.X., Fan, X.W. and Tang, Z.K., 2006. ZnO p-n junction light-emitting diodes fabricated on sapphire substrates. Applied physics letters, 88(3), p.031911.

[83] Wei, Z.P., Lu, Y.M., Shen, D.Z., Zhang, Z.Z., Yao, B., Li, B.H., Zhang, J.Y., Zhao, D.X., Fan, X.W. and Tang, Z.K., 2007. Room temperature p-n ZnO blue-violet light-emitting diodes. Applied physics letters, 90(4), p.042113.

[84] Lyons, J.L., Janotti, A. and Van de Walle, C.G., 2009. Why nitrogen cannot lead to p-type conductivity in ZnO. Applied Physics Letters, 95(25), p.252105.

[85] Liu, L., Xu, J., Wang, D., Jiang, M., Wang, S., Li, B., Zhang, Z., Zhao, D., Shan, C.X., Yao, B. and Shen, D.Z., 2012. p-Type conductivity in n-doped ZnO: the role of the N Zn− V O complex. Physical Review Letters, 108(21), p.215501.

[86] Yong, D.Y., He, H.Y., Tang, Z.K., Wei, S.H. and Pan, B.C., 2015. H-stabilized shallow acceptors in N-doped ZnO. Physical Review B, 92(23), p.235207.

[87] Reynolds, J.G., Reynolds Jr, C.L., Mohanta, A., Muth, J.F., Rowe, J.E., Everitt, H.O. and Aspnes, D.E., 2013. Shallow acceptor complexes in p-type ZnO. Applied Physics Letters, 102(15), p.152114.

[88] Tang, K., Zhu, S., Xu, Z., Shen, Y., Ye, J. and Gu, S., 2017. Formation of V Zn-N O acceptors with the assistance of tellurium in nitrogen-doped ZnO films. Journal of Alloys and Compounds, 699, pp.484-488.

[89] Ohgaki, T., Ohashi, N., Sugimura, S., Ryoken, H., Sakaguchi, I., Adachi, Y. and Haneda, H., 2008. Positive Hall coefficients obtained from contact misplacement on evident n-type ZnO films and crystals. Journal of Materials Research, 23(9), pp.2293-2295.

[90] Bierwagen, O., Ive, T., Van de Walle, C.G. and Speck, J.S., 2008. Causes of incorrect carrier-type identification in van der Pauw–Hall measurements. Applied Physics Letters, 93(24), p.242108.

[91] Adachi, Sadao. Properties of semiconductor alloys: group-IV, III-V and II-VI semiconductors. Vol. 28. John Wiley & Sons, 2009. p.150.

[92] Makino, T., Segawa, Y., Kawasaki, M. and Koinuma, H., 2005. Optical properties of excitons in ZnO-based quantum well heterostructures. Semiconductor science and technology, 20(4), p.S78.

[93] Makino, T., Segawa, Y., Kawasaki, M., Ohtomo, A., Shiroki, R., Tamura, K., Yasuda, T. and Koinuma, H., 2001. Band gap engineering based on Mg x Zn 1− x O and Cd y Zn 1− y O ternary alloy films. Applied Physics Letters, 78(9), pp.1237-1239.

[94] Das, S.C., Green, R.J., Podder, J., Regier, T.Z., Chang, G.S. and Moewes, A., 2013. Band gap tuning in ZnO through Ni doping via spray pyrolysis. The Journal of Physical Chemistry C, 117(24), pp.12745-12753.

[95] Adler, D. and Feinleib, J., 1970. Electrical and optical properties of narrow-band materials. Physical Review B, 2(8), p.3112.

[96] Agrawal, S., Parveen, A. and Azam, A., 2017. Microwave assisted synthesis of Co doped NiO nanoparticles and its fluorescence properties. Journal of Luminescence, 184, pp.250-255.

[97] Ahn, K.S., Deutsch, T., Yan, Y., Jiang, C.S., Perkins, C.L., Turner, J. and Al-Jassim, M., 2007. Synthesis of band-gap-reduced p-type ZnO films by Cu incorporation. Journal of Applied Physics, 102(2), p.023517.

[98] Ferhat, M., Zaoui, A. and Ahuja, R., 2009. Magnetism and band gap narrowing in Cu-doped ZnO. Applied Physics Letters, 94(14), p.142502.

[99] Chen, Y., Xu, X.L., Zhang, G.H., Xue, H. and Ma, S.Y., 2009. A comparative study of the microstructures and optical properties of Cu-and Ag-doped ZnO thin films. Physica B: Condensed Matter, 404(20), pp.3645-3649.

[100] Sernelius, B.E., Berggren, K.F., Jin, Z.C., Hamberg, I. and Granqvist, C.G., 1988. Band-gap tailoring of ZnO by means of heavy Al doping. Physical Review B, 37(17), p.10244.

[101] Makino, T., Segawa, Y., Yoshida, S., Tsukazaki, A., Ohtomo, A. and Kawasaki, M., 2004. Gallium concentration dependence of room-temperature near-band-edge luminescence in n-type ZnO: Ga. Applied Physics Letters, 85(5), pp.759-761.

[102] Nenavathu, B.P., Rao, A.K., Goyal, A., Kapoor, A. and Dutta, R.K., 2013. Synthesis, characterization and enhanced photocatalytic degradation efficiency of Se doped ZnO nanoparticles using trypan blue as a model dye. Applied Catalysis A: General, 459, pp.106-113.

[103] Tampo, H., Matsubara, K., Yamada, A., Shibata, H., Fons, P., Yamagata, M., Kanie, H. and Niki, S., 2007. High electron mobility Zn polar ZnMgO/ZnO heterostructures grown by molecular beam epitaxy. Journal of Crystal Growth, 301, pp.358-361.

[104] Tsukazaki, A., Yuji, H., Akasaka, S., Tamura, K., Nakahara, K., Tanabe, T., Takasu, H., Ohtomo, A. and Kawasaki, M., 2008. High Electron Mobility Exceeding 104 cm2 V-1 s-1 in MgxZn1-xO/ZnO Single Heterostructures Grown by Molecular Beam Epitaxy. Applied physics express, 1(5), p.055004.

[105] Falson, J., Kozuka, Y., Uchida, M., Smet, J.H., Arima, T.H., Tsukazaki, A. and Kawasaki, M., 2016. MgZnO/ZnO heterostructures with electron mobility exceeding 1× 106 cm2/Vs. Scientific reports, 6, p.26598.

[106] Wang, P., Shan, X., Guo, L., Ma, S., Chen, H., He, J. and Yang, Y., 2016. Monte Carlo investigation of high-field electron transport characteristics in ZnMgO/ZnO Heterostructures. IEEE Transactions on Electron Devices, 63(1), pp.517-523.

[107] M. H. Sukkar and H. L. Tuller, in Advances in Ceramics, edited by M. F. Yan and A. H. Heuer ~American Ceramic Society, Columbus, 1982, Vol. 7, p. 71.

[108] Mahan, G.D., 1983. Intrinsic defects in ZnO varistors. Journal of applied physics, 54(7), pp.3825-3832.

[109] Tuller, H.L., 2004. Highly conductive ceramics. MATERIALS ENGINEERING-NEW YORK-, 25, p. 118.

[110] Kobayashi, A., Sankey, O.F. and Dow, J.D., 1983. Deep energy levels of defects in the wurtzite semiconductors AIN, CdS, CdSe, ZnS, and ZnO. Physical Review B, 28(2), p.946.

[111] Oba, F., Nishitani, S.R., Isotani, S., Adachi, H. and Tanaka, I., 2001. Energetics of native defects in ZnO. Journal of Applied Physics, 90(2), pp.824-828.

[112] Liu, M., Kitai, A.H. and Mascher, P., 1992. Point defects and luminescence centres in zinc oxide and zinc oxide doped with manganese. Journal of Luminescence, 54(1), pp.35-42.

[113] Kohan, A.F., Ceder, G., Morgan, D. and Van de Walle, C.G., 2000. First-principles study of native point defects in ZnO. Physical Review B, 61(22), p.15019.

[114] Lin, B., Fu, Z. and Jia, Y., 2001. Green luminescent center in undoped zinc oxide films deposited on silicon substrates. Applied Physics Letters, 79(7), pp.943-945.

[115] Xu, P.S., Sun, Y.M., Shi, C.S., Xu, F.Q. and Pan, H.B., 2003. The electronic structure and spectral properties of ZnO and its defects. Nuclear Instruments and Methods in Physics Research Section B: Beam Interactions with Materials and Atoms, 199, pp.286-290.

[116] Zhang, S.B., Wei, S.H. and Zunger, A., 2001. Intrinsic n-type versus p-type doping asymmetry and the defect physics of ZnO. Physical Review B, 63(7), p.075205.

[117] Janotti, A. and Van de Walle, C.G., 2007. Native point defects in ZnO. Physical Review B, 76(16), p.165202.

[118] Look, D.C., Farlow, G.C., Reunchan, P., Limpijumnong, S., Zhang, S.B. and Nordlund, K., 2005. Evidence for native-defect donors in n-type ZnO. Physical Review Letters, 95(22), p.225502.

[119] Selim, F.A., Weber, M.H., Solodovnikov, D. and Lynn, K.G., 2007. Nature of native defects in ZnO. Physical review letters, 99(8), p.085502.

[120] McCluskey, M.D. and Jokela, S.J., 2007. Sources of n-type conductivity in ZnO. Physica B: Condensed Matter, 401, pp.355-357.

[121] Erhart, P., Albe, K. and Klein, A., 2006. First-principles study of intrinsic point defects in ZnO: Role of band structure, volume relaxation, and finite-size effects. Physical Review B, 73(20), p.205203.

[122] Zhang, S.B., Wei, S.H. and Zunger, A., 2001. Intrinsic n-type versus p-type doping asymmetry and the defect physics of ZnO. Physical Review B, 63(7), p.075205.

[123] Lyons, J.L., Janotti, A. and Van de Walle, C.G., 2009. Why nitrogen cannot lead to p-type conductivity in ZnO. Applied Physics Letters, 95(25), p.252105.

[124] Nickel, N.H. and Fleischer, K., 2003. Hydrogen local vibrational modes in zinc oxide. Physical review letters, 90(19), p.197402.

[125] Lavrov, E.V., Weber, J., Börrnert, F., Van de Walle, C.G. and Helbig, R., 2002. Hydrogen-related defects in ZnO studied by infrared absorption spectroscopy. Physical Review B, 66(16), p.165205.

[126] Erol, A., Okur, S., Comba, B., Mermer, Ö. and Arıkan, M.C., 2010. Humidity sensing properties of ZnO nanoparticles synthesized by sol–gel process. Sensors and Actuators B: Chemical, 145(1), pp.174-180.

[127] Yapabandara, K., Mirkhani, V., Sultan, M.S., Ozden, B., Khanal, M.P., Park, M., Wang, S., Hamilton, M.C., Chung, Y., Kim, D.J. and Sk, M.H., 2017. Study of device instability of bottom-gate ZnO transistors with sol–gel derived channel layers. Journal of Vacuum Science & Technology B, Nanotechnology and Microelectronics: Materials, Processing, Measurement, and Phenomena, 35(3), p.03D104.

[128] Choopun, S., Vispute, R.D., Noch, W., Balsamo, A., Sharma, R.P., Venkatesan, T., Iliadis, A. and Look, D.C., 1999. Oxygen pressure-tuned epitaxy and optoelectronic properties of laser-deposited ZnO films on sapphire. Applied Physics Letters, 75(25), pp.3947-3949.

[129] Li, G.R., Hu, T., Pan, G.L., Yan, T.Y., Gao, X.P. and Zhu, H.Y., 2008. Morphology−function relationship of ZnO: polar planes, oxygen vacancies, and activity. The Journal of Physical Chemistry C, 112(31), pp.11859-11864.

[130] Fu, Z., Yang, B., Li, L., Dong, W., Jia, C. and Wu, W., 2003. An intense ultraviolet photoluminescence in sol–gel ZnO–SiO2 nanocomposites. Journal of Physics: Condensed Matter, 15(17), p.2867.

[131] Solanki, R. and Collins, G.J., 1983. Laser induced deposition of zinc oxide. Applied Physics Letters, 42(8), pp.662-663.

[132] Roth, A.P. and Williams, D.F., 1981. Semiconducting zinc oxide films prepared by metal organic chemical vapor deposition from diethyl zinc. Journal of The Electrochemical Society, 128(12), pp.2684-2686.

[133] Shiosaki, T., Yamamoto, T., Yagi, M. and Kawabata, A., 1981. Plasma-enhanced metalorganic chemical vapor deposition of c-axis oriented and epitaxial films of ZnO at low substrate temperatures. Applied Physics Letters, 39(5), pp.399-401.

[134] Takahashi, N., Kaiya, K., Nakamura, T., Momose, Y. and Yamamoto, H., 1999. Growth of ZnO on sapphire (0001) by the vapor phase epitaxy using a chloride source. Japanese journal of applied physics, 38(4B), p.L454.

[135] Yamada, A., Sang, B. and Konagai, M., 1997. Atomic layer deposition of ZnO transparent conducting oxides. Applied Surface Science, 112, pp.216-222.

[136] Park, S.H.K., Hwang, C.S., Kwack, H.S., Lee, J.H. and Chu, H.Y., 2006. Characteristics of ZnO thin films by means of plasma-enhanced atomic layer deposition. Electrochemical and solid-state letters, 9(10), pp.G299-G301.

[137] Ohshima, E., Ogino, H., Niikura, I., Maeda, K., Sato, M., Ito, M. and Fukuda, T., 2004. Growth of the 2-in-size bulk ZnO single crystals by the hydrothermal method. Journal of Crystal Growth, 260(1), pp.166-170.

[138] Laudise, R.A. and Ballman, A.A., 1960. Hydrothermal synthesis of zinc oxide and zinc sulfide1. The Journal of Physical Chemistry, 64(5), pp.688-691.

[139] Johnson, M.A.L., Fujita, S., Rowland, W.H., Hughes, W.C., Cook, J.W. and Schetzina, J.F., 1996. MBE growth and properties of ZnO on sapphire and SiC substrates. Journal of electronic materials, 25(5), pp.855-862.

[140] Ogata, K., Kawanishi, T., Maejima, K., Sakurai, K., Fujita, S. and Fujita, S., 2002. ZnO growth using homoepitaxial technique on sapphire and Si substrates by metalorganic vapor phase epitaxy. Journal of crystal growth, 237, pp.553-557.

[141] Aranovich, J., Ortiz, A. and Bube, R.H., 1979. Optical and electrical properties of ZnO films prepared by spray pyrolysis for solar cell applications. Journal of vacuum science & technology, 16(4), pp.994-1003.

[142] Li, S.Y., Lee, C.Y. and Tseng, T.Y., 2003. Copper-catalyzed ZnO nanowires on silicon (100) grown by vapor–liquid–solid process. Journal of Crystal Growth, 247(3), pp.357-362.

[143] Matsumoto, K., Konemura, K. and Shimaoka, G., 1985. Crystal growth of ZnO by vapor transport in a closed tube using Zn and ZnCl 2 as transport agents. Journal of crystal growth, 71(1), pp.99-103.

[144] Huang, M.H., Wu, Y., Feick, H., Tran, N., Weber, E. and Yang, P., 2001. Catalytic growth of zinc oxide nanowires by vapor transport. Advanced Materials, 13(2), pp.113-116.

[145] Ianno, N.J., McConville, L. and Shaikh, N., 1992. Characterization of pulsed laser deposited zinc oxide. In MRS Proceedings (Vol. 276, p. 59). Cambridge University Press.

[146] Izaki, M. and Omi, T., 1996. Transparent zinc oxide films prepared by electrochemical reaction. Applied Physics Letters, 68(17), pp.2439-2440.

[147] Wong, E.M. and Searson, P.C., 1999. ZnO quantum particle thin films fabricated by electrophoretic deposition. Applied Physics Letters, 74(20), pp.2939-2941.

[148] Pan, Z.W., Dai, Z.R. and Wang, Z.L., 2001. Nanobelts of semiconducting oxides. Science, 291(5510), pp.1947-1949.

[149] Tiku, S.K., Lau, C.K. and Lakin, K.M., 1980. Chemical vapor deposition of ZnO epitaxial films on sapphire. Applied Physics Letters, 36(4), pp.318-320.

[150] Minegishi, K., Koiwai, Y., Kikuchi, Y., Yano, K., Kasuga, M. and Shimizu, A., 1997. Growth of p-type zinc oxide films by chemical vapor deposition. Japanese Journal of Applied Physics, 36(11A), p.L1453.

[151] Kim, Y.J. and Kim, H.J., 1999. Trapped oxygen in the grain boundaries of ZnO polycrystalline thin films prepared by plasma-enhanced chemical vapor deposition. Materials Letters, 41(4), pp.159-163.

[152] P. Singh, A. K. Chawla, D. Kaur and R. Chandra, Effect of oxygen partial pressure on the structural and optical properties of sputter deposited ZnO nanocrystalline thin films, Materials Letters 61 (2007) 2050–2053.

[153] Padmanathan Karthick Kannan, Ramiah Saraswathi, John Bosco Balaguru Rayappan, A highly sensitive humidity sensor based on DC reactive magnetron sputtered zinc oxide thin film, Sensors and Actuators A 164 (2010) 8–14.

[154] M. Suchea, S. Christoulakis, N. Katsarakis, T. Kitsopoulos, G. Kiriakidis, Comparative study of zinc oxide and aluminum doped zinc oxide transparent thin films grown by direct current magnetron sputtering, Thin Solid Films 515 (2007) 6562–6566.

[155] E. M. Fortunato, P. M. Barquinha, A. C. M. B. G. Pimentel, A. M. Gonçalves, A. J. Marques, L. M. Pereira and R. F. Martins, Fully transparent ZnO thin-film transistor produced at room temperature, Advanced Materials, 17(5), 590-594, (2005).

[156] R. Kumar, N. Khare, V. Kumar and G.L. Bhalla , Effect of intrinsic stress on the optical properties of nanostructured ZnO thin films grown by RF magnetron sputtering, Applied Surface Science 254 (2008) 6509–6513.

[157] S. Mandal, R.K. Singha, A. Dhar and S.K. Ray, Optical and structural characteristics of ZnO thin films grown by RF magnetron sputtering, Materials Research Bulletin 43 (2008) 244–250.

[158] G. J. Fang, D. J. Li and B.-L. Yao, Effect of Vacuum Annealing on the Properties of Transparent Conductive AZO Thin Films Prepared by DC Magnetron Sputtering, phys. stat. sol. (a) 193, No. 1, 139–152 (2002).

[159] W. Yang, Z. Liu, D. –L. Peng, F. Zhang, H. Huang, Y. Xie, Z. Wu, Room-temperature deposition of transparent conducting Al-doped ZnO films by RF magnetron sputtering method, Applied Surface Science 255 (2009) 5669–5673.

[160] X. -Y. Li, H.-J. Li, Z. -J. Wang, H. Xia and Z. -Y. Xiong, J. –X. Wang and B. -C. Yang, Effect of substrate temperature on the structural and optical properties of ZnO and Al-doped ZnO thin films prepared by dc magnetron sputtering, Optics Communications 282 (2009) 247–252.

[161] J. Lee, W. Gao, Z. Li, M. Hodgson, J. Metson, H. Gong, and U. Pal, "Sputtered deposited nanocrystalline ZnO films: A correlation between electrical, optical and microstructural properties", Appl. Phys. A 80, 1641 (2005).

[162] D. W. Bahnemann, C. Kormann and M. R. Hoffmann, J. Phys. Chem. 91, 3789 (1987)

[163] Howard, W.E., 2003. Thin Film Transistors—A Historical Perspective. Marcel Dekker, Inc., New York, NY, p.1.

[164] Bardeen, J., 2003. Semiconductor research leading to the point contact transistor. Great Solid State Physicists of the 20th Century. Edited by GONZALO JULIO A & LOPEZ CARMEN ARAGO. Published by World Scientific Publishing Co. Pte. Ltd., 2003. ISBN# 9789812795267, pp. 234-260, pp.234-260.

[165] Teal, G.K., Sparks, M. and Buehler, E., 1951. Growth of germanium single crystals containing p− n junctions. Physical Review, 81(4), p.637.

[166] Present, I., 2000. Cramming more components onto integrated circuits. Readings in computer architecture, 56.

[167] Moore, G.E., 1995, May. Lithography and the future of Moore's law. In Proc. Spie (Vol. 2437, No. 8, pp. 2-17).

[168] Bondyopadhyay, P.K., 1998. Moore's law governs the silicon revolution. Proceedings of the IEEE, 86(1), pp.78-81.

[169] Borkar, S., 1999. Design challenges of technology scaling. IEEE micro, 19(4), pp.23-29.

[170] Wang, Z.L. and Song, J., 2006. Piezoelectric nanogenerators based on zinc oxide nanowire arrays. Science, 312(5771), pp.242-246.

[171] Wang, Z.L., 2007. Nanopiezotronics. Advanced Materials, 19(6), pp.889-892.

[172] Dilonardo, E., Alvisi, M., Cassano, G. and Penza, M., 2017. Enhanced gas sensing properties of chemiresistors based on ZnO nanorods electrodecorated with Au and Pd nanoparticles. MRS Advances, 2(18), pp.1001-1007.

[173] Baruah, S., Maibam, B. and Kumar, S., 2017. Zinc Oxide: A Novel Material for Biosensors (A review). Imperial Journal of Interdisciplinary Research, 3(3)

[174] Ibupoto, Z.H., Khun, K. and Willander, M., 2013. A selective iodide ion sensor electrode based on functionalized ZnO nanotubes. Sensors, 13(2), pp.1984-1997.

[175] Kuo, Y., 2013. Thin film transistor technology—Past, present, and future. The Electrochemical Society Interface, 22(1), pp.55-61.

[176] Correia, A.P.P., Barquinha, P.M.C. and da Palma Goes, J.C., 2015. A Second-Order ΣΔ ADC Using Sputtered IGZO TFTs. Springer.

[177] Ohya, Y., Niwa, T., Ban, T. and Takahashi, Y., 2001. Thin film transistor of ZnO fabricated by chemical solution deposition. Japanese Journal of Applied Physics, 40(1R), p.297.

[178] Masuda, S., Kitamura, K., Okumura, Y., Miyatake, S., Tabata, H. and Kawai, T., 2003. Transparent thin film transistors using ZnO as an active channel layer and their electrical properties. Journal of Applied Physics, 93(3), pp.1624-1630.

[179] Carcia, P.F., McLean, R.S. and Reilly, M.H., 2006. High-performance ZnO thin-film transistors on gate dielectrics grown by atomic layer deposition. Applied physics letters, 88(12), p.123509.

[180] Park, S.H.K., Ryu, M., Hwang, C.S., Yang, S., Byun, C., Lee, J.I., Shin, J., Yoon, S.M., Chu, H.Y., Cho, K.I. and Lee, K., 2008, May. 42.3: Transparent ZnO Thin Film Transistor for the Application of High Aperture Ratio Bottom Emission AM-OLED

Display. In SID Symposium Digest of Technical Papers (Vol. 39, No. 1, pp. 629-632). Blackwell Publishing Ltd.

[181] Fortunato, E.M., Barquinha, P.M., Pimentel, A.C., Gonçalves, A.M., Marques, A.J., Martins, R.F. and Pereira, L.M., 2004. Wide-bandgap high-mobility ZnO thin-film transistors produced at room temperature. Applied Physics Letters, 85(13), pp.2541-2543.

[182] Kao, C.J., Kwon, Y.W., Heo, Y.W., Norton, D.P., Pearton, S.J., Ren, F. and Chi, G.C., 2005. Comparison of ZnO metal–oxide–semiconductor field effect transistor and metal–semiconductor field effect transistor structures grown on sapphire by pulsed laser deposition. Journal of Vacuum Science & Technology B: Microelectronics and Nanometer Structures Processing, Measurement, and Phenomena, 23(3), pp.1024-1028.

[183] Ong, B.S., Li, C., Li, Y., Wu, Y. and Loutfy, R., 2007. Stable, solution-processed, high-mobility ZnO thin-film transistors. Journal of the American Chemical Society, 129(10), pp.2750-2751.

[184] Fortunato, E., Barquinha, P., Pimentel, A., Goncalves, A., Marques, A., Pereira, L. and Martins, R., 2005. Recent advances in ZnO transparent thin film transistors. Thin solid films, 487(1), pp.205-211.

[185] Masuda, S., Kitamura, K., Okumura, Y., Miyatake, S., Tabata, H. and Kawai, T., 2003. Transparent thin film transistors using ZnO as an active channel layer and their electrical properties. Journal of Applied Physics, 93(3), pp.1624-1630.

[186] Nishii, J., Hossain, F.M., Takagi, S., Aita, T., Saikusa, K., Ohmaki, Y., Ohkubo, I., Kishimoto, S., Ohtomo, A., Fukumura, T. and Matsukura, F., 2003. High mobility thin film transistors with transparent ZnO channels. Japanese journal of applied physics, 42(4A), p.L347.

[187] Ohya, Y., Niwa, T., Ban, T. and Takahashi, Y., 2001. Thin film transistor of ZnO fabricated by chemical solution deposition. Japanese Journal of Applied Physics, 40(1R), p.297.

[188] Fortunato, E., Pimentel, A., Pereira, L., Goncalves, A., Lavareda, G., Aguas, H., Ferreira, I., Carvalho, C.N. and Martins, R., 2004. High field-effect mobility zinc oxide thin film transistors produced at room temperature. Journal of non-crystalline solids, 338, pp.806-809.

Chapter 3

Growth and Characterization of ZnO Channel Layers

3.1 Sol-gel Spin-Coating Growth Method

This chapter focuses on the growth method applied to deposit and the methods implemented to characterize the ZnO channel layers used to fabricate ZnO TFTs. ZnO was grown using the sol-gel spin-coating method by dropping the solution on the substrate followed by calcining the wafer. In order to prepare the sol-gel precursor, first, monoethanolamine (stabilizer) was diluted by isopropanol (solvent) and zinc acetate dihydrate [$Zn(CH_3COO)_2 .2H_2O$] was dissolved in the mixture. The molar ratio of Zn ions to monoethanolamine was kept at 1:1 and the Zn concentration was kept at 0.3 mol / L. The solution was stirred (600 rpm) at 80 ºC and for 2 h and then aged for 24 h in ambient temperature to yield a clear, homogenous and stable precursor. As the conductive substrate, two heavily-boron-doped silicon wafers (0.01 – 0.02 ohm.cm) were cleaned by acetone, methanol and deionized (DI) water, followed by hydrofluoric (HF) acid to remove possible redundant surface oxide. The wafers were then dry oxidized in order to achieve the bottom gate oxide layers. The precursor was then dropped on the oxidized wafers and rotated at 3000 rpm for 30 s. The coated wafers were then calcined at 285 ºC for 5 minutes in order to remove the organic residuals through evaporation. In order to study films with different thicknesses, as well as the effect of number of layers on film characteristics, the spin-coating and

calcination processes were repeated several times to achieve desired thicknesses. 5 sample wafers were prepared with different number of layers: 1 layer (1L), 2 layers (2L), 3 layers (3L), 4 layers (4L), 8 layers (8L). The wafers were diced into 4 quadrants to be annealed in 4 different temperatures: 600 ℃, 700 ℃, 800 ℃ and 900 ℃. The wafers were annealed in ambient air for 1 h to accommodate the formation of ZnO nanocrystallines through coalescence. The film thicknesses were measured with a profiler. Table 3.1 lists the range of the films' thicknesses. 1 cm by 1 cm pieces from each quadrant, close to the center of the original wafer, were chosen for Raman spectroscopy and photoluminescence measurements.

Table 3.1 Thickness range for ZnO samples with different number of layers annealed at different temperatures.

Number of layers →	1L	2L	3L	4L	8L
Anneal. Temper. ↓	Thickness (nm)				
600 ℃	33~40	60~65	76~79	105~115	180~185
700 ℃	25~30	50~55	75~79	90~115	155~175
800 ℃	30~50	50~63	75~85	90~105	183~196
900 ℃	40~49	60~70	75~85	100~115	200~225

Raman spectroscopy and photoluminescence were conducted by a homemade system with a blue laser (442 nm) for Raman scattering and a UV laser (325 nm) as an excitation source. A thermoelectrically cooled charge-coupled device (CCD) was used to collect the outgoing signals.

3.2 Raman Spectroscopy

Raman spectroscopy is a characterization method used to identify the crystal vibrational modes in a material. In this method, a monochromatic light source is used to excite a molecule from a vibrational state into a virtual excited state located between electronic states. The molecule then de-excites to a different vibrational state close to the initial state by emitting a photon, containing the energy difference between the initial and final vibrational states. Since these vibrational modes in the crystal structure interact with particles and quasiparticles, and can be created or annihilated, it's plausible to view these modes as quasiparticles. Photons of a specific wavelength interact with these quasiparticles, named as phonons, and are scattered either elastically or inelastically. In case of an elastic scattering in this photon-phonon interaction, namely Rayleigh scattering (named after Lord Rayleigh), the wavelength of the outgoing photon will be unaltered. In case of an inelastic scattering, namely Raman scattering (named after the discoverer of the phenomenon, Chandrasekhara Venkata Raman), the energy of the outgoing photon may be larger or smaller than the energy of the incoming photon. If the incoming photon interacts inelastically with a phonon at the ground state (near the Γ point in the Brillouin zone with the wave vector $\vec{k} = 0$), the collision will definitely result in a reduction in the outgoing photon's energy (Stokes scattering) resulting in the outgoing phonon jumping to an excited state. The inelastic collision of a photon with a phonon in an excited state however, may result in an energy loss of the photon similar to the previous case, or an energy loss of the excited phonon, lowering the state of the outgoing phonon and increasing the energy of the outgoing photon (anti-Stokes scattering). In the low temperature range, the probability of the incoming photon interacting with an excited phonon is several orders of magnitude smaller than the probability of its interaction with a ground state phonon. At relatively high temperatures, the population of thermodynamically excited states

is higher compared to the population of the same states at a lower temperature due to Maxwell-Boltzmann's distribution law

$$\frac{N_i}{N} = \frac{e^{-\beta E_i}}{\sum_j e^{-\beta E_j}}.$$

N_i is the number of the phonons in state i, β is defined as $\beta \equiv (k_B T)^{-1}$ where k_B is Boltzmann's constant and T is the absolute temperature and N is the total number of phonons. The sum in the denominator is over all vibrational mode energies. The population of the first excited state phonons (N_1) to the population of the ground state phonons (N_0) can be derived by

$$\frac{N_1}{N_0} = \frac{e^{-\beta E_1}}{e^{-\beta E_0}} = e^{-\beta \Delta E}$$

where $\Delta E = E_1 - E_0 > 0$. The energy difference (Raman shift) of the incoming and outgoing photons may be contributed to the creation or annihilation of phonons. As the temperature increases, β decreases, the population ratio gets closer to unity and therefore, an amplification is observed in anti-Stokes scattering. Since the energy differences between the vibrational modes of a material are unique, they may be considered as the fingerprints of that substance. The characterized material can be in gas, liquid or solid phases. In solid phases of the matter, the appearance of different modes may depend on the polarization of the incoming light and the orientation of the crystal structure.

In contrast with Raman scattering, in infra-red spectroscopy (IR), incident photons with frequencies equal to vibrational frequencies of different modes are absorbed. Whereas in Raman spectroscopy Raman shifts are analyzed, in IR spectroscopy the vibrational energies are directly obtained *via* absorption/transmittance (Figure 3.1).

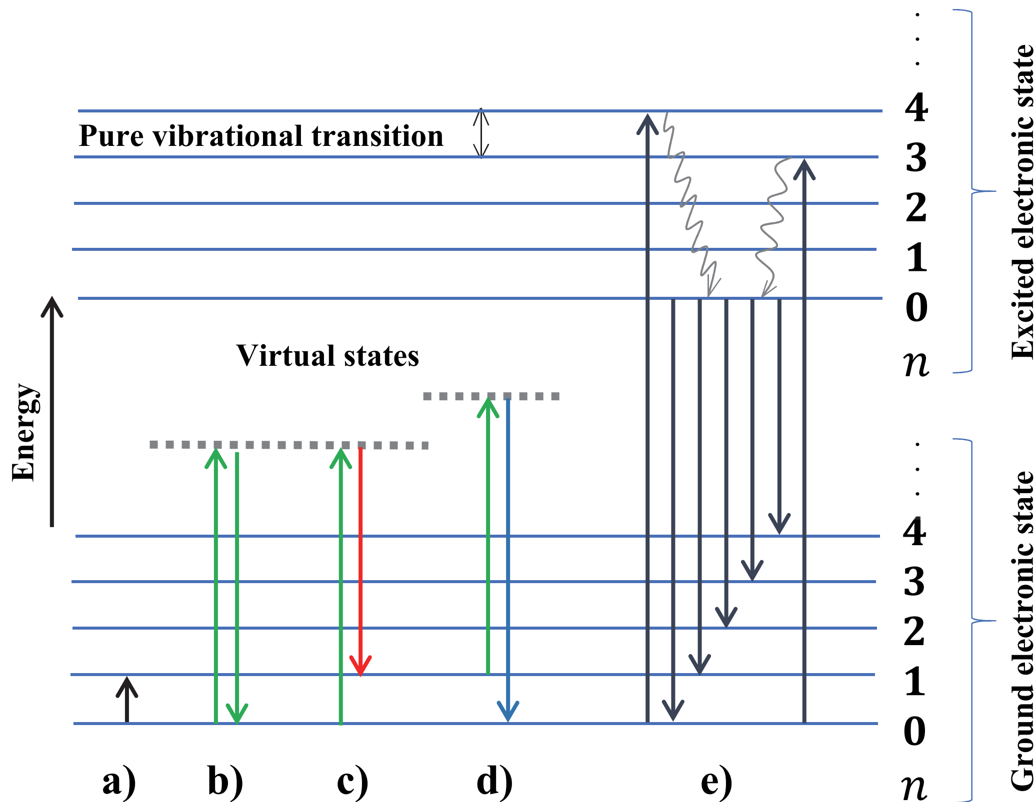

Figure 3.1: Infra-red transition (a), Rayleigh scattering (b), Stokes (c) and anti-Stokes (d) Raman scattering, and fluorescence (e) among electronic and vibrational energy levels.

The propagation direction of a plain electromagnetic wave is obtained by the direction of the Poynting vector $\vec{S}$ from $\vec{S} = \frac{1}{\mu_0}\vec{E} \times \vec{B}$ where μ_0 is the permeability of vacuum. The direction of importance, however, is the direction of the electric field $\vec{E}$. In Raman spectroscopy, in order to be consistent in calculating the energy shifts (vibrational mode transitions), a single wavelength is utilized for the incoming wave. To achieve this, monochromatic lasers are used as the incoming light source where the laser goes through a filter. The filter blocks unwanted wavelengths, as well as linearly polarizing the electric field in a certain direction. The dependence of the magnitude of the electric field as a function of time can be considered as a simple harmonic oscillator (SHO) and expressed as $E = E_0 \cos 2\pi f t$.

To achieve a basic understanding of Raman and Rayleigh scattering, the photon- phonon interaction and vibrational excitation can be approached with a combination of classical and quantum mechanical perspective.

In a classical approach, let us consider a diatomic molecule where the atoms can be considered as point masses (nucleus radii of the atoms become negligible compared to the molecule diameter) with a dipole moment P . The dipole moment is a function of the instantaneous interacting photons' electric field and the polarizability of the molecule (α). In general, polarizability is an intrinsic property of the material. Considering the oscillations of the magnitude of the electric field of the incoming wave, the dipole moment of the molecule can be written as $P = \alpha E = \alpha E_0 \cos 2\pi f t$. If the molecule has an initial vibrational frequency f_m the "small" nuclear displacement can be expressed as $x = x_0 \cos 2\pi f_m t$ with x_0 being the amplitude of this displacement. The condition for the existence of Raman scattering is whether the polarizability of the molecule alters with displacement. If the dependence is non-zero, polarizability can be approximated by Taylor expansion

$$\alpha = \alpha_0 + x(\frac{\partial \alpha}{\partial x})_0 + \frac{1}{2} x^2 (\frac{\partial^2 \alpha}{\partial x^2})_0 + \cdots$$

where α_0 is the initial polarizability of the molecule in the absence of an interaction (and hence, the equilibrium position x_0), and $(\frac{\partial \alpha}{\partial x})_0$ is the change of the polarizability with respect to displacement at x_0. The dipole moment can then be rewritten as

$$P = \alpha\, (E_0 \cos 2\pi f t) = (E_0 \cos 2\pi f t) \left(\alpha_0 + x \left(\frac{\partial \alpha}{\partial x} \right)_0 + \frac{1}{2} x^2 \left(\frac{\partial^2 \alpha}{\partial x^2} \right)_0 + \cdots \right) .$$

By replacing displacement x with its oscillatory form and only keeping the first order correction term, the dipole moment can be written as

$$P = \alpha_0 \, (E_0 \cos 2\pi f t) + (\frac{\partial \alpha}{\partial x})_0 \, (x_0 \cos 2\pi f_m t) \, (E_0 \cos 2\pi f t) + \cdots$$

Evidently, the "correction terms" to the initial value do not exist if the polarizability of the material stays unaltered with nucleus displacements, *i.e.* $(\frac{\partial \alpha}{\partial x})_0 = 0$. In other words, in case of a zero change in polarizability with small displacements, the material is Raman- inactive. Using the trigonometric identities, in the second term, the multiplication of the two oscillatory functions can be expressed as two separate single oscillatory functions with distinct frequencies

$$\cos 2\pi f_m t \cos 2\pi f t) = \frac{1}{2} \, [\cos 2\pi t (f + f_m) + \cos 2\pi t (f - f_m)]$$

and hence,

$$P = E_0 \, \alpha_0 \cos 2\pi f t + \frac{1}{2} E_0 \, x_0 \, (\frac{\partial \alpha}{\partial x})_0 [\cos 2\pi t (f + f_m) + \cos 2\pi t (f - f_m)] \; .$$

Therefore, we can consider the first term to be the inelastic interaction representing the Rayleigh scattering where the outgoing photon frequency is unaltered. The second term contains two oscillatory functions, representing two waves, one with higher frequency and one with lower frequency compared to the initial value. The higher frequency represents higher energy of the outgoing wave (noting that a photon's energy is linearly dependent on its frequency $E = hf$ where h is the Planck's constant) and was referred to as the anti-Stokes mode. The second oscillatory function with lower frequency represents the Stokes Raman scattering. The signal for Stokes Raman scattering is more intense compared to the anti-Stokes Raman scattering and easier to observe. In fact, Chandrasekhara Raman was able to observe the Stokes mode with his eyes by using the sun as his light source, a telescope as the collecting lens.[1] Thereby, Stokes mode is commonly used among researchers for Raman spectroscopy.

The quantum mechanical aspect of the Raman scattering comes into play when vibrational mode transitions are deliberated. The vibration frequencies of a certain material are unique because

quantum mechanics (QM) dictates certain frequencies to be allowed due to the quantization of the vibrational energies of the material. In diatomic molecule previously mentioned, for instance, if the masses are m1 and m2 for each atom, and the distances of the nuclei from the center of mass (CM) are r1 and r2 respectively, in order to simulate the molecular vibrations into a simple physical problem, we can consider the chemical bond to be analogous to a spring with a constant K. If we consider the classical approach, the classical Lagrangian $L = T - V$ for the system (T representing the kinetic energy and V representing the potential energy) can then be derived and it can be observed that there are no limitations on the vibrational frequencies. In one-dimensional diatomic molecule Lagrangian, one can turn the two-body problem into a single body with a "reduced mass" defined as $\mu \equiv (\frac{1}{m_1} + \frac{1}{m_2})^{-1}$ with displacement X from the CM and obtain

$$L = \frac{\mu \dot{X}^2}{2} - \frac{KX^2}{2}$$

where $\dot{X}$ is defined as the time derivative of the displacement. By inserting the Lagrangian into the Euler-Lagrange equation

$$\frac{d}{dt}\frac{\partial L}{\partial \dot{X}} - \frac{\partial L}{\partial X} = 0$$

the simple harmonic oscillator (SHO) equation can be obtained

$$\mu \ddot{X} + KX = 0 \,.$$

The solutions for this differential equation are a sum of imaginary exponential functions of time. The solution for displacement $X(t)$ can be expressed as a sum of real oscillatory functions. Eventually, we can express $X(t)$ as a single oscillatory function $X(t) = X_0 \cos(2\pi f t + \theta_0)$ where θ_0 and X_0 are the phase constant and the oscillation amplitude, respectively, defined by the initial

boundary conditions; and $f = \frac{1}{2\pi}\sqrt{\frac{K}{\mu}}$ is the oscillation frequency. No limitations were forced in this derivation. Namely, the vibrational frequencies can be continuous.

If we consider the QM approach, however, the Hamiltonian of the system (the Schrodinger equation), which should be considered for a two-body wave-particle system, can be rewritten into a single wave-function since the wave-particles overlap each other and can be treated as a single wave- function ψ. The Hamiltonian operator for a single wave-particle with a reduced mass μ and total momentum P oscillating with angular frequency ω, which resembles the simple quantum harmonic oscillator (QHO) system, can then be expressed as

$$\hat{H} = \left(\frac{\hat{P}^2}{2\mu} + \frac{\mu\omega^2\hat{X}^2}{2}\right).$$

By expressing all the operators in position-space, *i.e.* $\hat{P} \equiv -i\hbar\frac{\partial}{\partial x}$ and $\hat{X} \equiv x$, and considering the isolated oscillator as a closed system, *i.e.* $\psi(\vec{r},t) \equiv e^{\frac{-iEt}{\hbar}}\psi(\vec{r})$, the Hamiltonian ($\hat{H} \equiv i\hbar\frac{\partial}{\partial t}$) can be expressed as

$$\hat{H}\,|\psi> = \left(\frac{-\hbar^2}{2\mu}\frac{\partial^2}{\partial x^2} + \frac{\mu\omega^2 x^2}{2}\right)|\psi> = E|\psi> .$$

Note the dissimilarity between the above equation (the general differential equation governing the one-dimensional QHO) and the general differential equation governing the SHO in one dimension $\left(\frac{d^2}{dt^2} + \omega^2\right)x = 0$ (where the angular frequency ω is a real number).

For a simpler representation, by defining the dimensionless variables $y \equiv x\sqrt{\frac{\mu\omega}{\hbar}}$ and $\epsilon \equiv \frac{E}{\hbar\omega}$, the Schrodinger equation becomes $\left(\frac{\partial^2}{\partial y^2} - y^2 + 2\epsilon\right)\psi = 0$. This QHO Schrodinger equation can be solved by spectral method (considering the solution as a sum of basis functions in series form).[2] The solution for a bound eigenstate ψ in position-space is a product of a compressed

exponential decay function $e^{-\frac{\alpha x^2}{2}}$ where $\alpha \equiv \frac{\mu\omega}{\hbar}$, discrete normalization coefficients $\left(\alpha/\pi\right)^{1/4}\ (2^n\, n!)^{-1/2}$ and a discrete set of polynomials called Hermite polynomials which the nth order can be derived from $H_n(y) = (-1)^n\, e^{y^2}\, \frac{\partial^n}{\partial y^n}(e^{-y^2})$ where $y \equiv x\sqrt{\alpha}$. Therefore, the "eigenstate" wave-function for the nth order QHO is

$$\psi_n(x) = \left(\alpha/\pi\right)^{1/4} .\ (2^n\, n!)^{-1/2} .\ e^{-\frac{\alpha x^2}{2}}\ .\ H_n\left(x\sqrt{\alpha}\right).$$

By setting $n = 0$ and $H_0(y) = 1$, we can obtain the ground state as $\psi_0(x) = \left(\alpha/\pi\right)^{1/4}\ e^{-\frac{\alpha x^2}{2}}$ and its corresponding energy as $E_0 = \frac{1}{2}\hbar\omega$, since $\epsilon = \frac{1}{2}$.

Several differences are discernible between the classical method and the quantum mechanical approach. The ground state $\psi_0(x)$ is simply a Gaussian distribution and unlike the classical approach, the position probability density $|\psi_0(x)|^2$ does not cease to exist beyond the oscillation amplitude or any finite point in position space. This implies that a negative kinetic energy in QHO is not inconceivable. The nodes in the standing waves of SHO are the nodes of the oscillatory functions and the oscillator's position is terminated at the boundaries, whereas the origin of the nodes for the stationary states of QHO, is the roots of the Hermite polynomials $H_n(y)$. Outside the classical boundary (mandated by the total energy of the oscillator), $e^{-\frac{\alpha x^2}{2}} H_n(y)$ is only terminated at infinity and therefore, the quantum oscillator has a non-zero probability of being outside the classical boundary. The ground state energy E_0 is in disagreement with the classical approach as well, in the sense that the minimum energy is non-zero and a minimum value is enforced. But the main difference, which is of concern when considering a Raman shift, is the discreteness of the energy states in QHO which originates from the form of the differential equation. Along solving the differential equations, the solutions for the SHO are continuous

exponential (however imaginary) functions, whereas the solution for the QHO is in series form (dictating discreteness). Accordingly, the energy states can be denoted as $E_n = \left(n + \frac{1}{2}\right)\hbar\omega$, representing n as the order of oscillation and the minimum energy interval $\Delta E = \hbar\omega$ between energy states. The former equation is obtained during solving the QHO Schrodinger equation *via* the spectral method, by setting the recursive coefficients to zero after n terms (in order to avert the divergence catastrophe) and combining the results of the even and odd parities of possible bound eigenstates. Hence, a requirement for legitimate transitions from first state υ' to the final state υ'' is the transition energy difference of an integer factor N of $\hbar\omega$ (*i.e.* ${}^{\Delta E}/_{\hbar\omega} = \Delta\upsilon = \pm N$). In QM, another requirement for a possible transition in general, is that the value of the transition moment integral

$$\overleftrightarrow{\mathrm{M}}_{\upsilon',\upsilon''} \equiv \int_{-\infty}^{+\infty} \psi'^{*}\, \overleftrightarrow{\mu}\, \psi''\, dV \quad .$$

must be non-zero; where ψ' and ψ'' are the initial and final transition states, $\overleftrightarrow{\mu}$ is the transition moment operator and $\overleftrightarrow{\mathrm{M}}_{\upsilon',\upsilon''}$ is the transition dipole moment. For instance, in infra-red (IR) spectroscopy, $\overleftrightarrow{\mu}$ translates to the electric dipole moment of the molecule $\vec{\mu} = \sum_n q_n \vec{x}_n$ (with point charge q_m being at position vector $\vec{x}_m$) and in Raman spectroscopy, it translates to the polarizability tensor $\overleftrightarrow{\alpha}_{\upsilon',\upsilon''}$. The symmetry of the integrand changes with the symmetry of $\overleftrightarrow{\mu}$; and since ψ' and ψ'' are orthonormal eigenstates, the symmetry of the integrand defines whether the value of the transition dipole moments is non-zero. The polarizability tensor $\overleftrightarrow{\alpha}_{\upsilon',\upsilon''} = \alpha_{\upsilon',\upsilon''} - i\alpha'_{\upsilon',\upsilon''}$ is comprised of a symmetric component α and an antisymmetric component α' . In case of complex wavefunctions and systems which are not symmetric under time reversal, such as magnetic phenomena, there will be non-zero antisymmetric components in the polarizability tensor.[3] In normal Raman scattering, however, the polarizability tensor is symmetric

($\left[\alpha_{x_i x_j}\right]_{v', v''} = \left[\alpha_{x_j x_i}\right]_{v', v''}$) . Therefore, if one of the six transition moment integrals is non-zero, namely

$$[\alpha_{xx}]_{v', v''} = \int_{-\infty}^{+\infty} \psi'^{*} \, \alpha_{xx} \, \psi'' \, dV \neq 0$$

$$[\alpha_{xy}]_{v', v''} = \int_{-\infty}^{+\infty} \psi'^{*} \, \alpha_{xy} \, \psi'' \, dV \neq 0$$

$$\vdots$$

the vibration transition is Raman-active. In the aforementioned integrals (Raman spectrum selection rules), the integrand's symmetry is dependent on the symmetry of the product of electric dipole moments μ_{x_i} where x_i represents space coordinates x, y and z. For example, the symmetry of α_{xy} is related to the symmetry of $\mu_x \mu_y$. The symmetric and antisymmetric terms can be obtained from

$$\alpha_{x_i x_j} = \frac{2}{\hbar} \sum_{i \neq j} \frac{\omega_{ji}}{{\omega_{ji}}^2 - \omega^2} \, Re \left(\left\langle i \,\middle|\, \mu_{x_i} \,\middle|\, j \right\rangle \left\langle j \,\middle|\, \mu_{x_j} \,\middle|\, i \right\rangle \right) = \alpha_{x_j x_i}$$

$$\alpha'_{x_i x_j} = -\frac{2}{\hbar} \sum_{i \neq j} \frac{\omega}{{\omega_{ji}}^2 - \omega^2} \, Im \left(\left\langle i \,\middle|\, \mu_{x_i} \,\middle|\, j \right\rangle \left\langle j \,\middle|\, \mu_{x_j} \,\middle|\, i \right\rangle \right) = -\, \alpha'_{x_j x_i}$$

where x_i and x_j are permutations of space coordinates x, y and z ; $|i\rangle$ and $|i\rangle$ represent the ground and j^{th} excited state of the molecule; ω is the angular frequency of the incident plane wave and the angular frequency shift is $\omega_{ji} = \omega_j - \omega_i$. If the *polarizability ellipsoid* (a surface obtained from plotting $1/\sqrt{\alpha_{x_i x_j}}$ in three dimensions) is visualized, the Raman-active vibrational modes are the ones in which at least one of the ellipsoid properties (orientation, shape or size) of changes from one extreme displacement to the other. Figure 3.2 indicates how the polarizability ellipsoid evolves as the atoms are displaced in different vibrational modes of a linear (CO_2) and a non-linear

(H_2O) triatomic molecule. For a CO_2 molecule, the second and third modes' ellipsoids (ν_2 and ν_3) have the same variations at the extremums ($+\delta x$ and $-\delta x$), resulting in these modes to be Raman-inactive; whereas in an H_2O molecule at least one ellipsoid property at $+\delta x$ contrasts with the one at $-\delta x$, resulting in all modes to be Raman-active in H_2O.

Since most of the population of phonons reside in the ground state ($n = 0$) and the next most populous state is the first excited state ($n = 1$), the probability of transitions occurring between these two states, and consequently the signal intensity of this shift, is notably higher than transitions between other states.

Since the wurtzite ZnO crystal has a unit cell with $N = 4$ atoms, the $3N = 12$ vibrational modes are divided into 3 acoustic modes (1 longitudinal and 2 transverse) and $3N - 3 = 9$ optical modes (3 longitudinal and 6 transverse). These modes may be written as the irreducible normal modes $\Gamma_{Opt} = A_1 + 2B_1 + E_1 + 2E_2$ for the wurtzite structure (C_{6v}^4 symmetry). B_1 modes are both Raman and IR inactive (silent modes). A_1 and E_1 modes are polar and are both Raman and IR active, splitting into transverse optical (TO) and longitudinal optical (LO) modes; *e.g.* A_1 (TO), A_1 (LO), E_1 (TO) and E_1 (LO) modes. E_2 modes are non-polar, with a high (E_2^H) and a low (E_2^L) frequency; also referred to as E_2(high) and E_2(low). The E_2^L (E_2^H) mode has been attributed to the vibration of the zinc (oxygen) sublattice.[4]

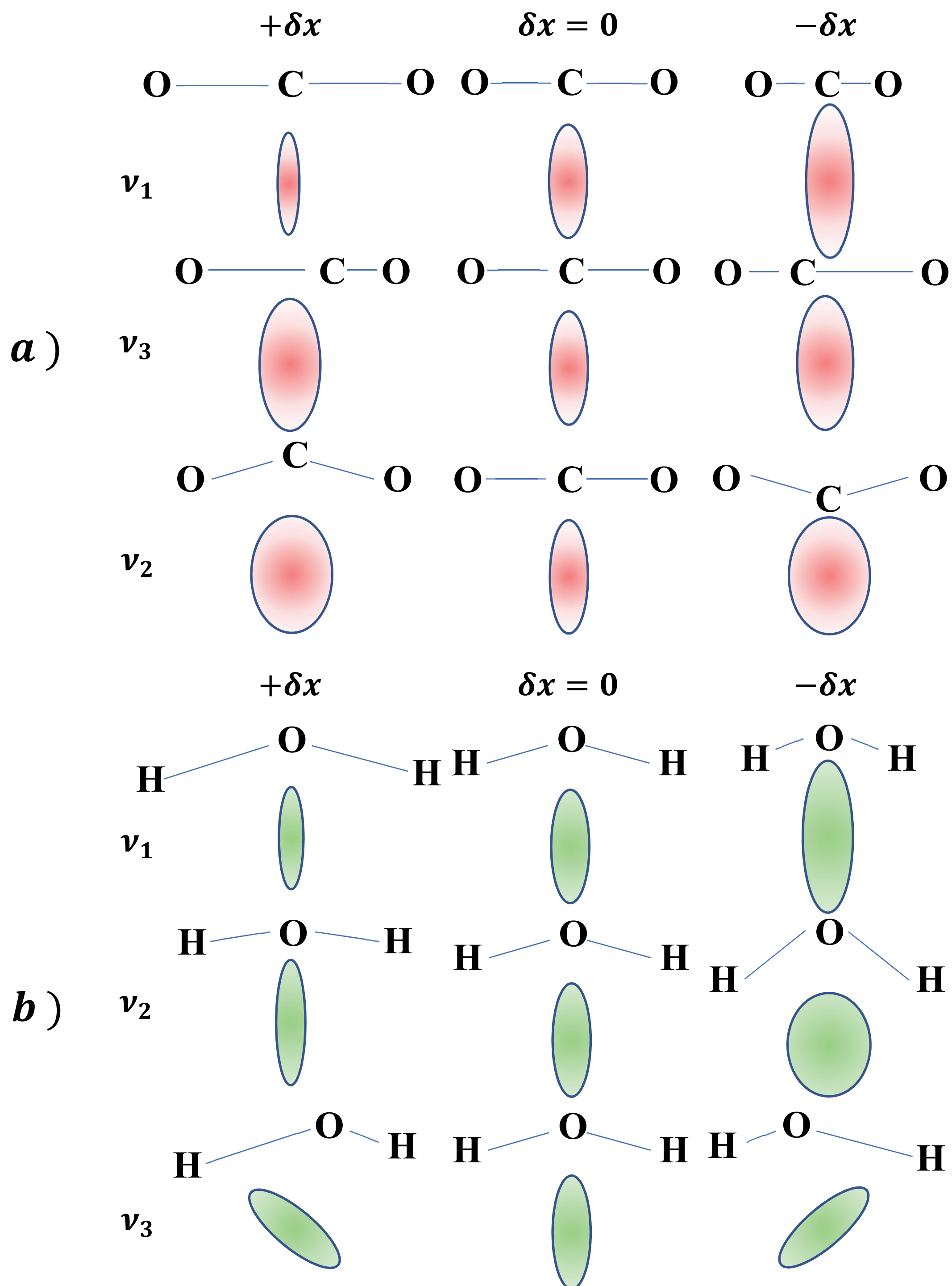

Figure 3.2: Polarizability ellipsoids' evolutions during displacements in different vibrational modes ν_1, ν_2 and ν_3 in (a) CO_2 and (b) H_2O molecules.

The propagation/polarization orientations of the incident/scattered rays in Raman scattering are of great importance. In Porto's notation $A(B,C)D$ indicates the propagation orientation of the incident ray to be A, the propagation orientation of the scattered ray to be D, the polarization orientation of the incident ray to be B, and the polarization orientation of the scattered ray to be C.

Damen *et al.* studied the vibrational modes of wurtzite ZnO. Table 3.2 presents the experimental Raman shifts, and the required configurations to observe the vibrational modes, obtained by Damen *et al.*[5] The Raman shift obtained from bulk single crystal ZnO sample, purchased from Eagle-Picher Technologies LLC, are in agreement with the presented values (Figure 3.3). Despite the fact that E_1(TO) is forbidden in the $Z(-,-)\bar{Z}$ configuration, the presence of this mode is probably due to the breakdown of the selection rule.[6] Damen *et al.* attributed the peaks around the 204, 330 and 538 cm^{-1} to multi-phonon processes.

Table 3.2 Experimental Raman shifts and configurations required to observe the phonon modes in bulk single-crystal wurtzite ZnO. The bar over a direction (*e.g.* $\bar{X}$) represents the opposite of that direction (*e.g.* X).

Mode (Symmetry)	Raman shift (cm^{-1})	Configurations
E_2^L	101	$X(Y,Y)\bar{X}$; $X(Y,Y)Z$; $Z(Y,Y)\bar{Z}$; $Z(Y,X)\bar{Z}$
E_2^H	437	$X(Y,Y)\bar{X}$; $X(Y,Y)Z$; $Z(Y,Y)\bar{Z}$; $Z(Y,X)\bar{Z}$
E_1 (TO)	407	$X(Z,Y)\bar{X}$; $X(Y,Z)Y$
E_1 (LO)	583	$X(Y,Z)Y$
A_1 (TO)	380	$X(Y,Y)\bar{X}$; $X(Z,Z)\bar{X}$
A_1 (LO)	574	$Z(Y,X)\bar{Z}$

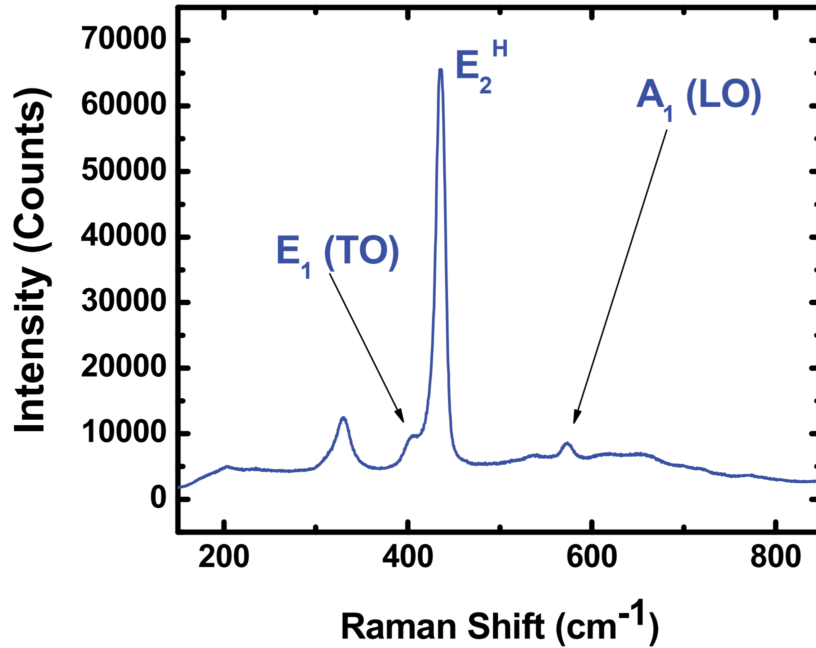

Figure 3.3: The Raman shift of bulk ZnO. The E_2^H , E_1(TO) and A_1(LO) modes can be observed.

Whereas the first order Raman scattering (one phonon process) deals with phonons near the Γ point (where the wave vector $\vec{k} = 0$), the second (or higher) order Raman scattering (multi-phonon processe) can occur for phonons throughout the entire Brillouin zone.[7]

Table 3.3 summarizes the values reported by various experimental groups, along with the E_2^H mode Raman shift obtained from the sol-gel derived ZnO film fabricated in this work. The table contains the six optical normal modes of ZnO, as well as the commonly observed peaks, believed to be related to multi-phonon processes (higher order vibrational modes).

Calzolari and Nardelli [8] used the Perdew-Burke- Ernzerhof [9] (PBE) method with Hubbard-like corrections (PBE+U) to calculate the Raman shifts, where U is a parameter describing the on-

site Coulomb interactions.[10] Their calculated results for E_2^L, A_1(TO), E_1(TO) and E_2^H modes (106, 384, 408 and 436 cm^{-1}, respectively) were in agreement with other reported experimental values.

The E_2 mode frequencies (101 and 437 cm^{-1}) are reported for a stress-free wurtzite ZnO lattice. These values will have a shift if the lattice is under stress. In case of a compressive stress, the E_2 frequencies will increase whereas under a tensile stress, a decrease in the E_2 frequencies will be observed.[11] Stress may arise from the lattice mismatch and distortion[12], or the mismatch of thermal expansion coefficients of the substrate and the deposited film.[13]

Raman spectroscopy was performed in order to investigate the dependence of the crystal quality of the ZnO films, grown by the sol-gel spin coating method, on the annealing temperature. E_2^H peak was observed in all samples. Figure 3.4 depicts the dependence of the E_2^H peak on the annealing temperature. For the sample with higher number of deposited layers (Figure 3.4(e)), the difference is more apparent with the magnitude of the peak becoming larger as the annealing temperature increases. For this set of data collection, the following settings were used: 2400 gratings per mm and 5000 ms exposure time.

The magnitude enhancement of the E_2^H peak of the 8-layer sample, compared to other samples, can be attributed to the higher thickness of the film whereas in thinner samples, the background signal is comparable to the signal from E_2^H mode. As the annealing temperature increases, the grain size becomes larger and the number of received signals from vibrational modes (*i.e.* oxygen sublattice vibration) rises. Due to the non-linearity across the charge-coupled device (CCD), the E_2^H values were corrected.

Table 3.3 Raman shift values reported by experimental groups.

Sample Dim. [Ref.]	E_2^L	A_1(TO)	E_1(TO)	E_2^H	A_1(LO)	E_1(LO)	$E_2^H - E_2^L$	$2\times E_2^L$	Misc. Multi-Phonon
Powder[14]	–	383	410	438	540	584	–	–	–
Powder[15]	100	380	–	437	580	–	–	204	331
Bulk[16]	98	378	409.5	437.5	576	588	–	–	–
Nanotubes[17]	–	376	–	438	532	579	335	–	661, 780, 1073, 1149
Powder[18]	98	380	410	438	574	–	334	203	483
Powder[19]	99	384	410	439	569	586	–	–	616, 660, 810
Bulk[20]	99	378	410	438	574	590	333	203	284, 618, 666, 812
Commercial Powder[21]	–	380	–	437	–	584	330	–	540
Commercial Powder[22]	–	379	410	436	–	–	329	–	1150
Bulk[23]	–	384	426	438	–	580	332	–	321, 537
Nanotubes	–	383	423	437	–	578	331	–	316, 534, 505, 549
Conventional sol-gel film (300nm)[24]	–	–	–	437	–	–	–	–	–
Novel sol-gel film (2μm)	–	380	–	435	577	–	330	–	–
This work	–	–	–	436.8	–	–	–	–	–

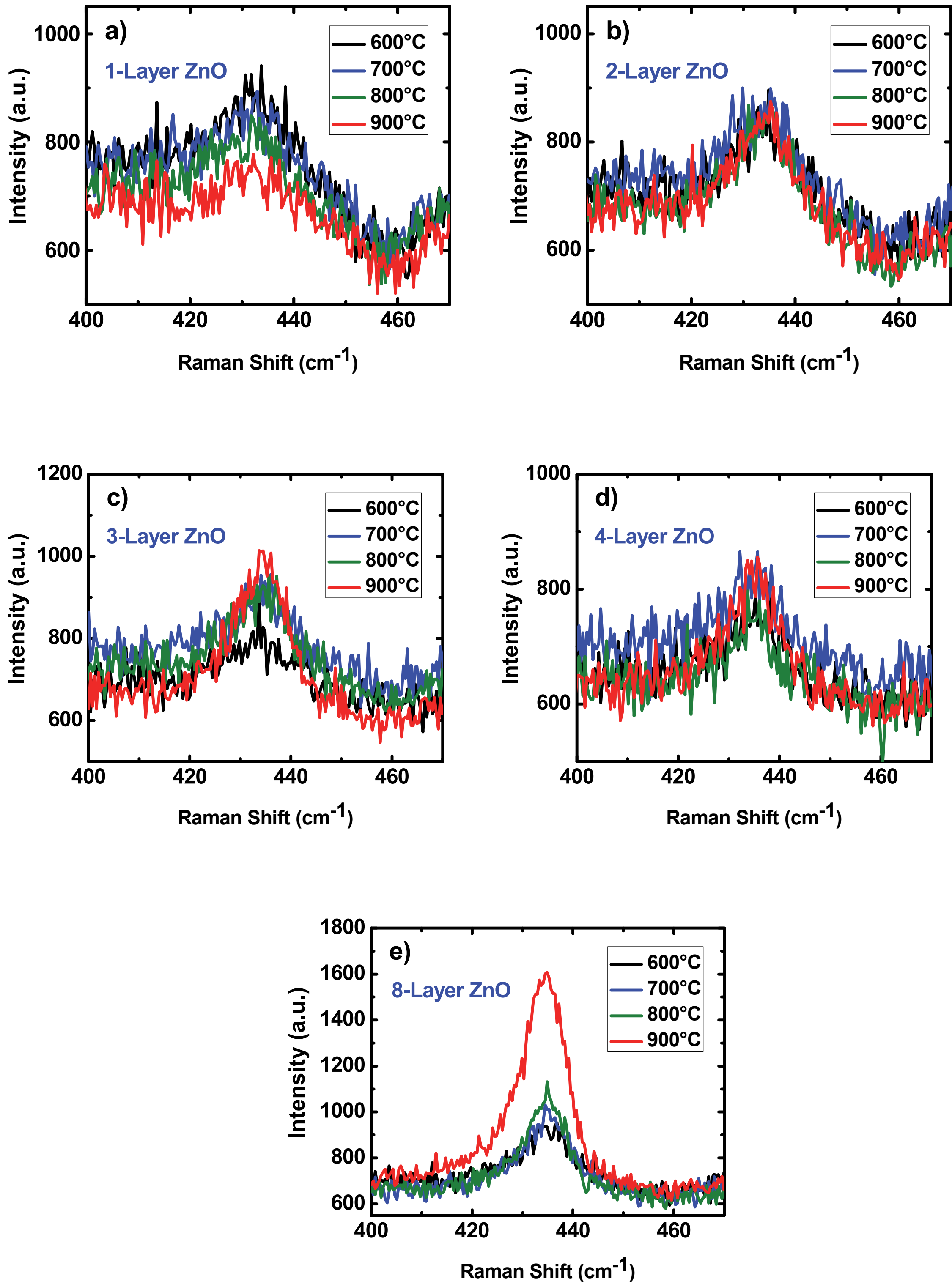

Figure 3.4: The dependence of Raman spectra of ZnO layers deposited *via* sol-gel spin-coating method on the annealing temperature for (a) 1 layer, (b) 2 layers, (c) 3 layer, (d) 4 layers and (e) 8 layers.

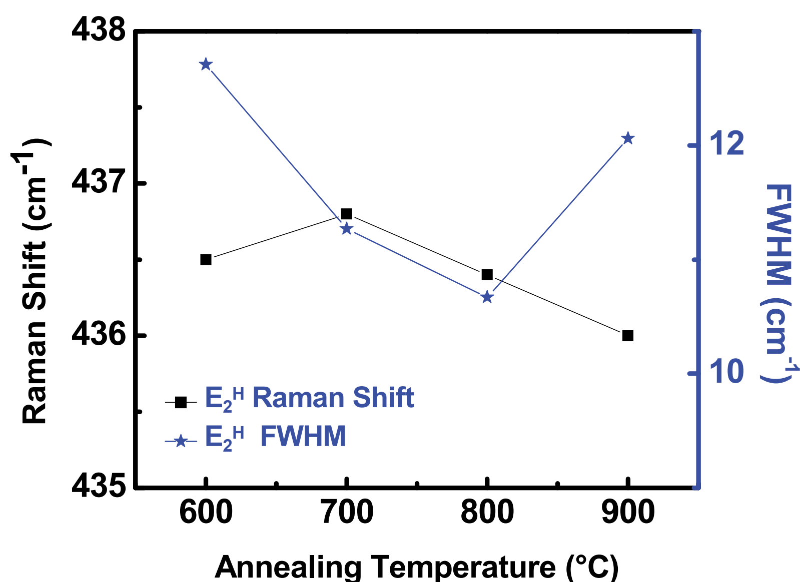

Figure 3.5: The dependence of E_2^H Raman shift and the FWHM of the peak on the annealing temperature for the 8-layer ZnO.

Figure 3.5 compares the position and the full width at half maximum (FWHM) of the E_2^H peak of the 8-layer samples annealed at different temperatures. Although the positions and the FWHM of the peaks seem to differ, the range of the difference is within the experimental error limit. Therefore, although the increase of the magnitude of the E_2^H peak is sometimes attributed to the enhancement of crystal quality,[25] a strong conclusion about crystal quality difference between the samples cannot be stated solely based on this data set.

3.3 Photoluminescence

Whereas Raman spectroscopy is used to identify chemical bonds through vibrational modes of a material, photoluminescence spectroscopy is a crude characterization method to outline its electronic structure properties. Photoluminescence is a type of luminescence generated by photo-excitation. The incident photons from a light source may alter the electronic state of a

molecule which then relaxes to a final state *via* one or several relaxation mechanisms. De-excitation of the molecule may occur *via* emitting phonons or photons, corresponding to vibrational or electronic de-excitations, respectively. In photoluminescence spectroscopy (referred to as PL hereafter), a material is exposed to a monochromatic light and the re-emitted photons with different wavelengths are collected by a spectrometer. In WBGSs, the incident wavelength is in the UV range to overcome the band gap and the re-emitted photons contain information about the formation of different donor-acceptor pairs (DAP) or the existence of electronic states inside the band gap due to crystal defects such as dopants, vacancies or interstitial atoms. Photoluminescence spectroscopy usually spans the wavelengths (or their corresponding energies) in the UV, visible and IR range. PL is a viable characterization method for direct band gap semiconductors.

Room temperature PL on ZnO exhibits a narrow UV luminescence which is dedicated to ZnO near band edge (NBE) excitonic emissions, followed by a presumable visible luminescence. Narrower and more intense excitonic emission indicates a higher crystal quality[26] due to less non-radiative recombination and defect transition. Despite the visible luminescence from defects being undesirable in many applications, engineering these defects or associating ZnO luminescence with other materials may bring about visual applications and display devices.[27]

Low temperature (~4K) PL from ZnO samples indicate UV emission spikes caused by recombination of DAP and their longitudinal optical phonon replicas.[28] Room temperature PL, however, is not able to resolve the DAP related spikes. Investigation of the visible luminescence in ZnO is accompanied by the comparison of point defect energy levels in the gap. Various point defects exist in wurtzite ZnO structures, such as charged vacancies and interstitials, which contribute to the luminescence of ZnO from the violate to the IR spectral range. The visible luminescence of ZnO has been rather complicated and controversial. Red luminescence has been

attributed to positively charged oxygen vacancy (V_O^+), negatively charged oxygen interstitial (O_i^-) , zinc interstitial (Zn_i) , zinc vacancy (V_{Zn}) and lattice disorders along the c-axis [29,30,31] whereas orange luminescence has been attributed to transitions from the conduction band minimum (CBM) to O_i or from Zn_i to O_i .[32] The yellow luminescence has been ascribed to related transitions from the C.B. to either native (O_i)[33,34] or extrinsic (lithium impurities)[35,36] defects. The origin of the green luminescence has been the most controversial, complicated and discussed topic among researchers. Vanheusden *et al.*[37] attributed the green emission to transitions from the conduction band to V_O^+. The green luminescence has been attributed to several other recombination mechanisms such as hydrogen outdiffusion in thin ZnO films[38], deep V_O donor level transitions to the valence band[39], V_{Zn} on non-polar nanostructure surfaces[40], and transitions from V_{Zn} + V_O divacancies (V_{ZnO})[41] and V_{Zn} complexes.[42] The green luminescence has also been ascribed to unintentional copper (Cu) contamination in samples.[43,44,45] Blue and violet luminescence may correspond to electron transitions from CBM to V_{Zn}^-,[46] Zn_i to the maximum of the valence band maximum (VBM)[47] , Zn_i to V_{Zn} [48] and extended Zn_i to VBM.[49] Fu *et al.*[50] observed the intensity of UV luminescence increase in ZnO-SiO_2 nanocomposites. They ascribed the luminescence to the creation of levels due to the formation of Zn–O–Si bonds at the ZnO/SiO_2 interfaces. Figure 3.6 illustrates[51] some of the defect energy states in the band gap reported by different groups. The figure includes impurities such as lithium (Li) and hydrogen interstitials (H_i) as well as native defects such as oxygen antisites (O_{Zn}).

Figure 3.7 shows the photoluminescence (PL) of the bulk single crystal ZnO sample (refer to Figure 3.3 for Raman). The spectrum can be divided into the UV PL and the visible PL. The visible PL indicates a broad green luminescence centered at 510nm in addition to a blue

luminescence centered at 470 nm. In addition to the peak centered at 377 nm, the UV PL seems to contain another peak centered at 390 nm. Both peaks will be discussed shortly.

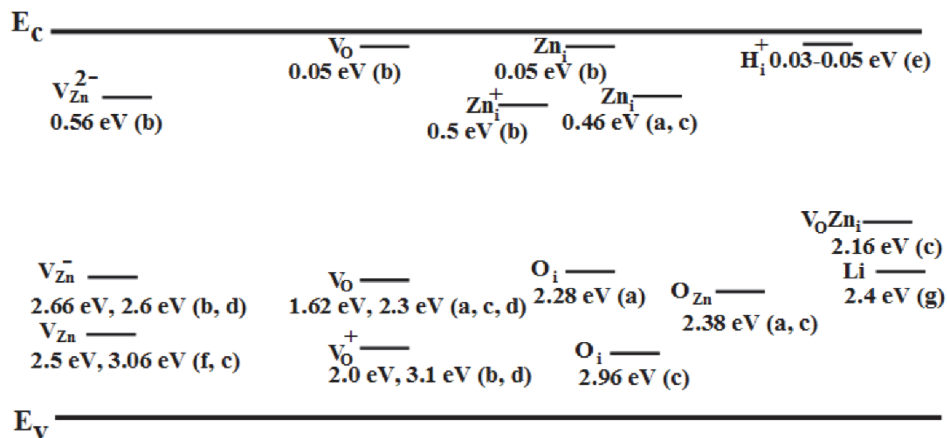

Figure 3.6: Energy states created by native point defects as reported by (a) Djurišić *et al.*[52], (b) Lima *et al.*[53], (c) Lin *et al.*[54], (d) Nikitenko *et al.*[55], (e) Van de Walle[56], (f) Janotti and Van de Walle[57], and (g) Zwingel.[58] *Reprinted figure under MDPI's Open Access Policy. Figure by Magnus Willander, Omer Nur, Jamil Rana Sadaf, Muhammad Israr Qadir, Saima Zaman, Ahmed Zainelabdin, Nargis Bano, and Ijaz Hussain, Luminescence from zinc oxide nanostructures and polymers and their hybrid devices, Materials 3, No. 4, pp. 2643-2667 (2010). Copyright (2010) by the Molecular Diversity Preservation International.*

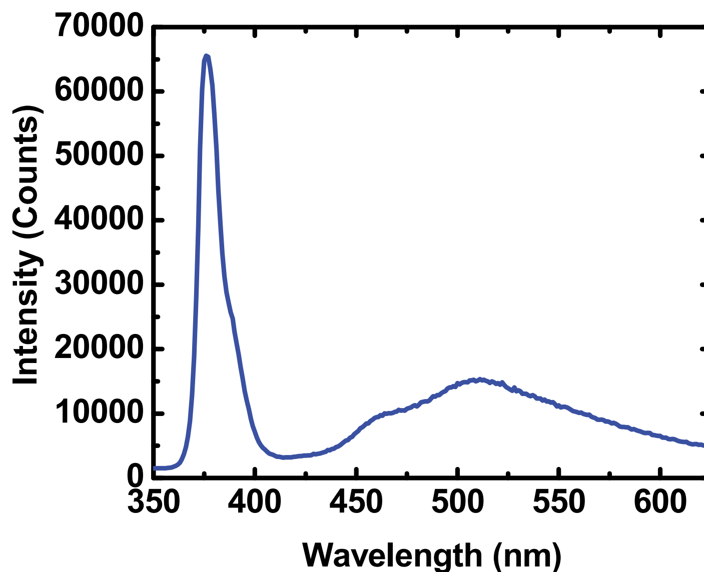

Figure 3.7: PL spectrum of bulk ZnO.

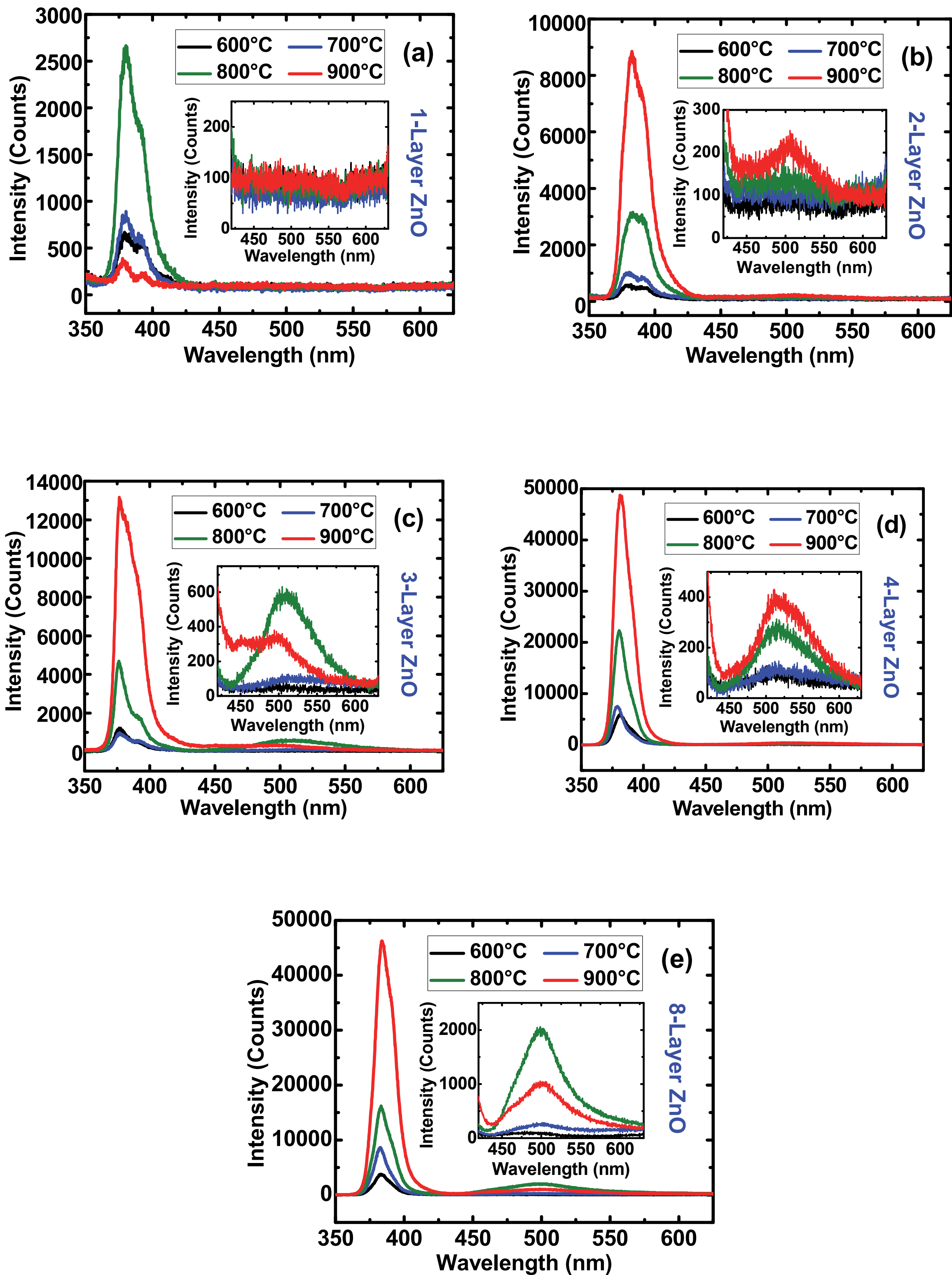

Figure 3.8: PL spectra of ZnO films for different annealing temperatures: (a) 1 layer, (b) 2 layers, (c) 3 layer, (d) 4 layers and (e) 8 layers. The insets depict the visible region.

PL of ZnO channel layers deposited *via* spin-coating was obtained with the 2400 grating per mm setting. For the exposure time interval, 200 ms was chosen to avoid saturation in the UV region. For a higher data resolution, wavelength step-size was chosen to be 0.2 nm. Figure 3.8 shows the PL spectra in the visible and UV range and the insets represent the magnified visible portion of the films' PL. The UV PL for the single layer ZnO (Figure 3.8 (a)) depicted 2 distinct peaks. These 2 peaks become less distinct as the number of layers increases. The peak around 380 nm (3.26 eV) is the near band edge (NBE) emission. The peak around 390 nm (3.18 eV) has been attributed to the exciton-exciton "P" emission where a photon, an electron and a hole are produced as the result of an exciton-exciton scattering.[59,60,61] Figure 3.9 shows the peak position for the NBE emission (Xc1) and the exciton-exciton "P" emission (Xc2) as a function of annealing temperature and Figure 3.10 shows the peak positions as a function of the number of layers. The UV luminescence exhibits an increase in magnitude as the number of layers increases. Since the penetration depth of UV laser with a 325 nm wavelength is in the range of 40nm[62] to 60 nm[63], the magnitude of the UV emission of the 4-layer sample compares to the UV emission of the 8-layer sample.

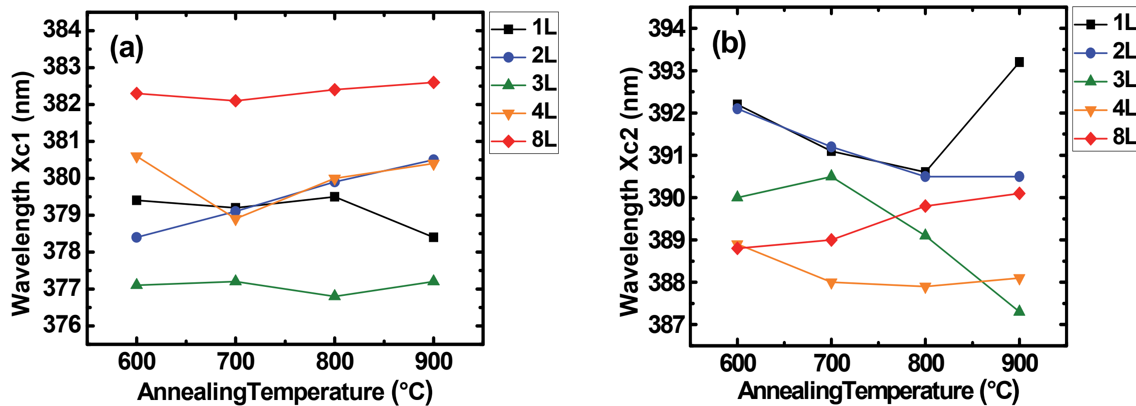

Figure 3.9: Peak position center, Xc, for (a) the NBE emission, Xc1, and (b) the exciton-exciton "P" emission, Xc2, as a function of annealing temperature.

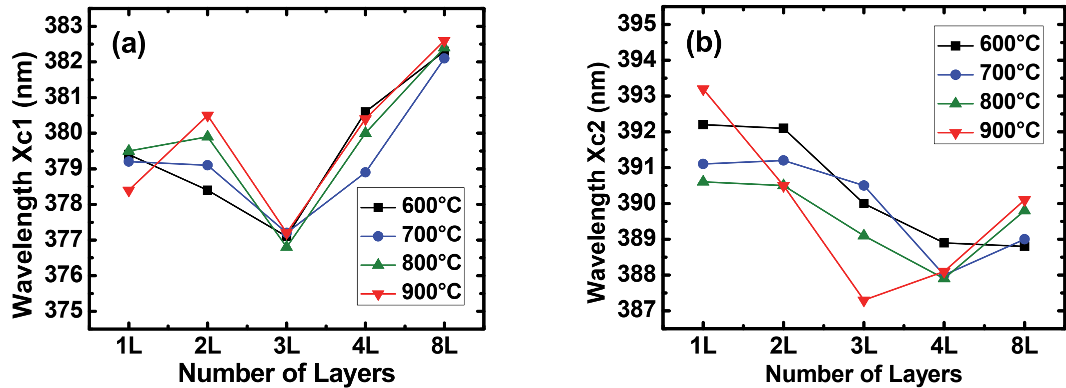

Figure 3.10: Peak position center, Xc, for (a) the NBE emission, Xc1, and (b) the exciton-exciton "P" emission, Xc2, as a function of the number of layers.

To further analyze the PL spectra, the ratio of the area under the curve for the UV emission over the visible emission (A(UV)/A(Vis)) was calculated to obtain a qualitative perspective over the crystal quality of the samples. Lower A(UV)/A(Vis) is assumed to be an indication of higher number of defects[64] due to the visible emission of midgap states originating from point defects formerly discussed. Figure 3.10 shows A(UV)/A(Vis) evolution as a function of the annealing temperature and the number of ZnO layers.

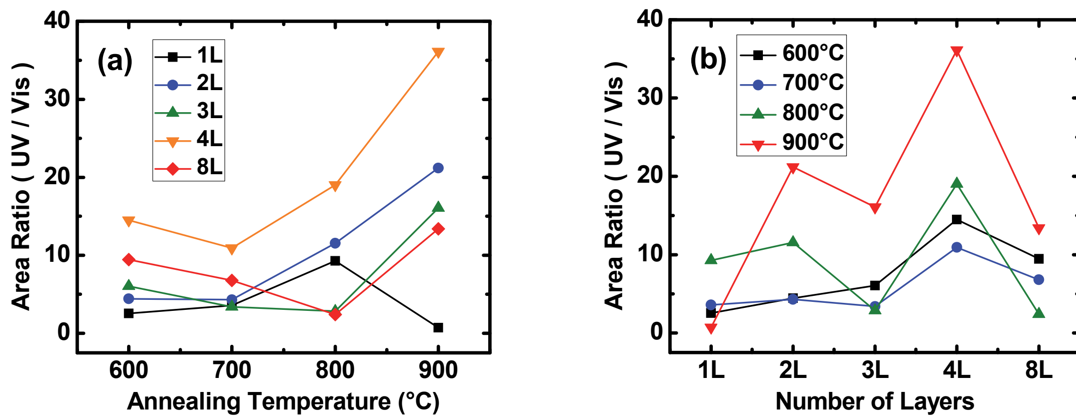

Figure 3.11: Ratio of the integrated area under the UV PL over the visible PL as a function of (a) annealing temperature and (b) number of layers.

3.4 Scanning Electron Microscopy

To fabricate thin film transistors (TFTs), the annealing temperature of 800 ℃ was chosen based on the fact that for the higher annealing temperature (*i.e.* 900 ℃), the increase in the grain size results in the formation of gaps between the grains according to Scanning Electron Microscopy (SEM) images. The ZnO film becomes non-continuous and hence, the reduction of carrier mobility.[65] Figure 3.12 shows the SEM images (SEM, JSM-7000F, JEOL, JAPAN) from the samples with different annealing temperatures. As the annealing temperature increases, the grain size becomes larger and the grain boundaries become less significant. However, for the sample with 900 ℃ annealing temperature, the films continuity is drastically affected.

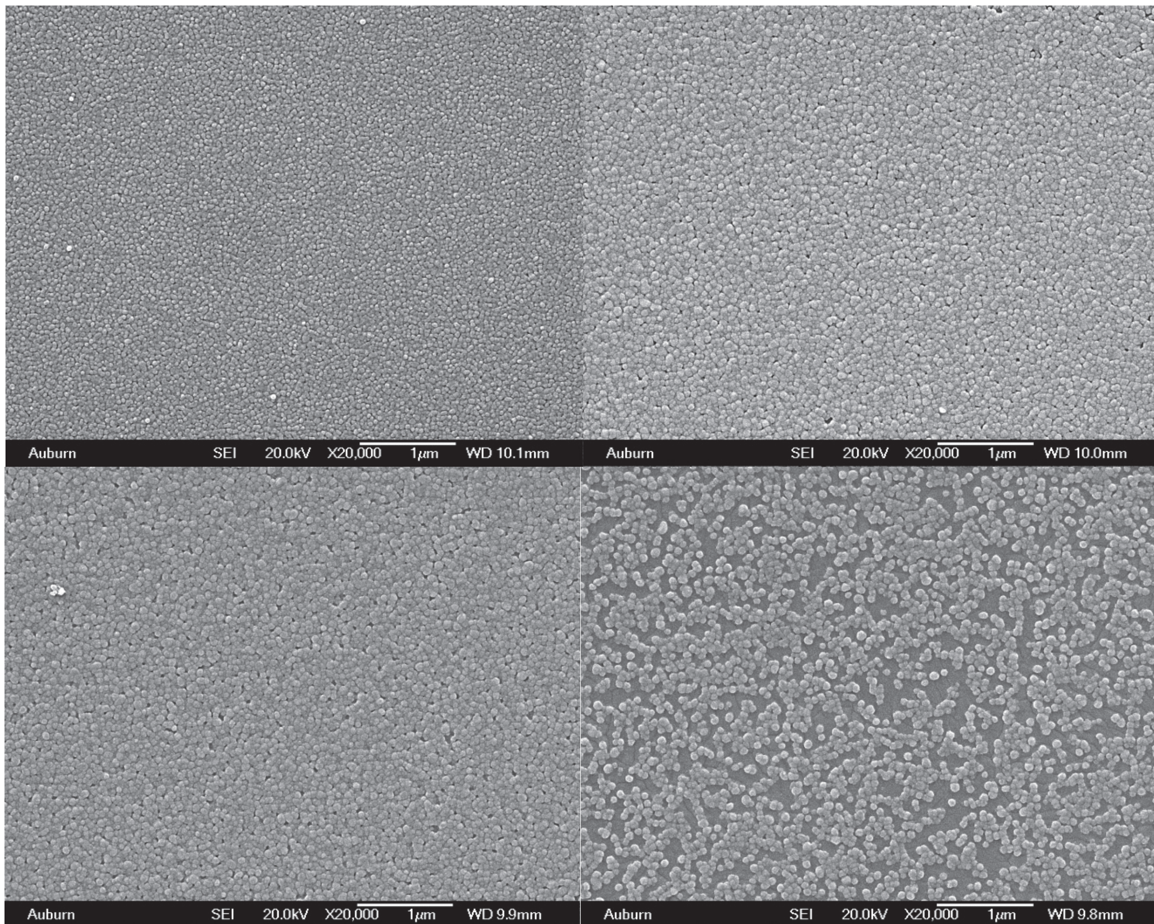

Figure 3.12: SEM images of the 2-layer ZnO film annealed at 600 ℃ (top left), 700 ℃ (top right), 800 ℃ (bottom left), and 900 ℃ (bottom right).

References

[1] Ferraro, J.R., 2003. Introductory raman spectroscopy. Academic press.

[2] Saxon, D.S., 2013. Elementary quantum mechanics. Courier Corporation.

[3] Barron, L.D. and Buckingham, A.D., 1975. Rayleigh and Raman optical activity. Annual Review of Physical Chemistry, 26(1), pp.381-396.

[4] Koyano, M., QuocBao, P., HongHa, L., NgocLong, N. and Katayama, S.I., 2002. Photoluminescence and Raman Spectra of ZnO Thin Films by Charged Liquid Cluster Beam Technique. physica status solidi (a), 193(1), pp.125-131.

[5] Damen, T.C., Porto, S.P.S. and Tell, B., 1966. Raman effect in zinc oxide. Physical Review, 142(2), p.570.

[6] Ashkenov, N., Mbenkum, B.N., Bundesmann, C., Riede, V., Lorenz, M., Spemann, D., Kaidashev, E.M., Kasic, A., Schubert, M., Grundmann, M. and Wagner, G., 2003. Infrared dielectric functions and phonon modes of high-quality ZnO films. Journal of Applied Physics, 93(1), pp.126-133.

[7] Gao, H., Yan, F., Zhang, H., Li, J., Wang, J. and Yan, J., 2007. First and second order Raman scattering spectroscopy of nonpolar a-plane GaN. Journal of applied physics, 101(10), p.103533.

[8] Calzolari, A. and Nardelli, M.B., 2013. Dielectric properties and Raman spectra of ZnO from a first principles finite-differences/finite-fields approach. Scientific reports, 3, p.2999.

[9] Perdew, J.P., Burke, K. and Ernzerhof, M., 1996. Generalized gradient approximation made simple. Physical review letters, 77(18), p.3865.

[10] Available online: https://wiki.fysik.dtu.dk/gpaw/tutorials/hubbardu/hubbardu.html, April 2018.

[11] Kuball, M., 2001. Raman spectroscopy of GaN, AlGaN and AlN for process and growth monitoring/control. Surface and Interface Analysis, 31(10), pp.987-999.

[12] Mukaida, H., Okumura, H., Lee, J.H., Daimon, H., Sakuma, E., Misawa, S., Endo, K. and Yoshida, S., 1987. Raman scattering of SiC: Estimation of the internal stress in 3C-SiC on Si. Journal of applied physics, 62(1), pp.254-257.

[13] Ager III, J.W. and Drory, M.D., 1993. Quantitative measurement of residual biaxial stress by Raman spectroscopy in diamond grown on a Ti alloy by chemical vapor deposition. Physical Review B, 48(4), p.2601.

[14] Wang, R.P., Xu, G. and Jin, P., 2004. Size dependence of electron-phonon coupling in ZnO nanowires. Physical Review B, 69(11), p.113303.

[15] Zeferino, R.S., Flores, M.B. and Pal, U., 2011. Photoluminescence and Raman scattering in Ag-doped ZnO nanoparticles. Journal of applied physics, 109(1), p.014308.

[16] Bairamov, B.H., Heinrich, A., Irmer, G., Toporov, V.V. and Ziegler, E., 1983. Raman study of the phonon halfwidths and the phonon—plasmon coupling in ZnO. physica status solidi (b), 119(1), pp.227-234.

[17] Tong, Y., Liu, Y., Shao, C., Liu, Y., Xu, C., Zhang, J., Lu, Y., Shen, D. and Fan, X., 2006. Growth and optical properties of faceted hexagonal ZnO nanotubes. The Journal of Physical Chemistry B, 110(30), pp.14714-14718.

[18] Zhao, J., Yan, X., Yang, Y., Huang, Y. and Zhang, Y., 2010. Raman spectra and photoluminescence properties of In-doped ZnO nanostructures. Materials Letters, 64(5), pp.569-572.

[19] Šćepanović, M., Grujić-Brojčin, M., Vojisavljević, K., Bernik, S. and Srećković, T., 2010. Raman study of structural disorder in ZnO nanopowders. Journal of Raman Spectroscopy, 41(9), pp.914-921.

[20] Cuscó, R., Alarcón-Lladó, E., Ibáñez, J., Artús, L., Jiménez, J., Wang, B. and Callahan, M.J., 2007. Temperature dependence of Raman scattering in ZnO. Physical Review B, 75(16), p.165202.

[21] Windisch Jr, C.F., Exarhos, G.J., Yao, C. and Wang, L.Q., 2007. Raman study of the influence of hydrogen on defects in ZnO. Journal of applied physics, 101(12), p.123711.

[22] Dong, Z.W., Zhang, C.F., Deng, H., You, G.J. and Qian, S.X., 2006. Raman spectra of single micrometer-sized tubular ZnO. Materials Chemistry and Physics, 99(1), pp.160-163.

[23] Xing, Y.J., Xi, Z.H., Xue, Z.Q., Zhang, X.D., Song, J.H., Wang, R.M., Xu, J., Song, Y., Zhang, S.L. and Yu, D.P., 2003. Optical properties of the ZnO nanotubes synthesized via vapor phase growth. Applied Physics Letters, 83(9), pp.1689-1691.

[24] Huang, Y., Liu, M., Li, Z., Zeng, Y. and Liu, S., 2003. Raman spectroscopy study of ZnO-based ceramic films fabricated by novel sol–gel process. Materials Science and Engineering: B, 97(2), pp.111-116.

[25] Al Asmar, R., Atanas, J.P., Ajaka, M., Zaatar, Y., Ferblantier, G., Sauvajol, J.L., Jabbour, J., Juillaget, S. and Foucaran, A., 2005. Characterization and Raman investigations on high-quality ZnO thin films fabricated by reactive electron beam evaporation technique. Journal of Crystal Growth, 279(3-4), pp.394-402.

[26] Fu, Z., Lin, B., Liao, G. and Wu, Z., 1998. The effect of Zn buffer layer on growth and luminescence of ZnO films deposited on Si substrates. Journal of crystal growth, 193(3), pp.316-321.

[27] Son, D.I., Kwon, B.W., Park, D.H., Seo, W.S., Yi, Y., Angadi, B., Lee, C.L. and Choi, W.K., 2012. Emissive ZnO-graphene quantum dots for white-light-emitting diodes. Nature nanotechnology, 7(7), pp.465-471.

[28] Meyer, B.K., Alves, H., Hofmann, D.M., Kriegseis, W., Forster, D., Bertram, F., Christen, J., Hoffmann, A., Straßburg, M., Dworzak, M. and Haboeck, U., 2004. Bound exciton and donor–acceptor pair recombinations in ZnO. physica status solidi (b), 241(2), pp.231-260.

[29] Cai, J.H., Ni, G., He, G. and Wu, Z.Y., 2008. Red luminescence in ZnO films prepared by a glycol-based Pechini method. Physics Letters A, 372(22), pp.4104-4108.

[30] Gomi, M., Oohira, N., Ozaki, K. and Koyano, M., 2003. Photoluminescent and structural properties of precipitated ZnO fine particles. Japanese journal of applied physics, 42(2R), p.481.

[31] Djurišić, A.B., Leung, Y.H., Tam, K.H., Ding, L., Ge, W.K., Chen, H.Y. and Gwo, S., 2006. Green, yellow, and orange defect emission from ZnO nanostructures: Influence of excitation wavelength. Applied Physics Letters, 88(10), p.103107.

[32] Ahn, C.H., Kim, Y.Y., Kim, D.C., Mohanta, S.K. and Cho, H.K., 2009. A comparative analysis of deep level emission in ZnO layers deposited by various methods. Journal of Applied Physics, 105(1), p.013502.

[33] Liu, M., Kitai, A.H. and Mascher, P., 1992. Point defects and luminescence centres in zinc oxide and zinc oxide doped with manganese. Journal of Luminescence, 54(1), pp.35-42.

[34] Wu, X.L., Siu, G.G., Fu, C.L. and Ong, H.C., 2001. Photoluminescence and cathodoluminescence studies of stoichiometric and oxygen-deficient ZnO films. Applied Physics Letters, 78(16), pp.2285-2287.

[35] Zwingel, D., 1972. Trapping and recombination processes in the thermoluminescence of Li-doped ZnO single crystals. Journal of Luminescence, 5(6), pp.385-405.

[36] Schirmer, O.F. and Zwingel, D., 1970. The yellow luminescence of zinc oxide. Solid State Communications, 8(19), pp.1559-1563.

[37] Vanheusden, K., Seager, C.H., Warren, W.T., Tallant, D.R. and Voigt, J.A., 1996. Correlation between photoluminescence and oxygen vacancies in ZnO phosphors. Applied physics letters, 68(3), pp.403-405.

[38] Gu, X., Sabuktagin, S., Teke, A., Johnstone, D., Morkoç, H., Nemeth, B. and Nause, J., 2004. Effect of thermal treatment on ZnO substrate for epitaxial growth. Journal of Materials Science: Materials in Electronics, 15(6), pp.373-378.

[39] Kang, H.S., Kang, J.S., Kim, J.W. and Lee, S.Y., 2004. Annealing effect on the property of ultraviolet and green emissions of ZnO thin films. Journal of Applied Physics, 95(3), pp.1246-1250.

[40] Fabbri, F., Villani, M., Catellani, A., Calzolari, A., Cicero, G., Calestani, D., Calestani, G., Zappettini, A., Dierre, B., Sekiguchi, T. and Salviati, G., 2014. Zn vacancy induced green luminescence on non-polar surfaces in ZnO nanostructures. Scientific reports, 4, p.5158.

[41] Li, M., Xing, G., Xing, G., Wu, B., Wu, T., Zhang, X. and Sum, T.C., 2013. Origin of green emission and charge trapping dynamics in ZnO nanowires. Physical Review B, 87(11), p.115309.

[42] Leung, Y.H., Chen, X.Y., Ng, A., Guo, M.Y., Liu, F.Z., Djurišić, A.B., Chan, W.K., Shi, X.Q. and Van Hove, M.A., 2013. Green emission in ZnO nanostructures—

Examination of the roles of oxygen and zinc vacancies. Applied Surface Science, 271, pp.202-209.

[43] Dingle, R., 1969. Luminescent transitions associated with divalent copper impurities and the green emission from semiconducting zinc oxide. Physical Review Letters, 23(11), p.579.

[44] Kuhnert, R. and Helbig, R., 1981. Vibronic structure of the green photoluminescence due to copper impurities in ZnO. Journal of Luminescence, 26(1-2), pp.203-206.

[45] Garces, N.Y., Wang, L., Bai, L., Giles, N.C., Halliburton, L.E. and Cantwell, G., 2002. Role of copper in the green luminescence from ZnO crystals. Applied Physics Letters, 81(4), pp.622-624.

[46] Wu, X.L., Siu, G.G., Fu, C.L. and Ong, H.C., 2001. Photoluminescence and cathodoluminescence studies of stoichiometric and oxygen-deficient ZnO films. Applied Physics Letters, 78(16), pp.2285-2287.

[47] Fang, Z., Wang, Y., Xu, D., Tan, Y. and Liu, X., 2004. Blue luminescent center in ZnO films deposited on silicon substrates. Optical Materials, 26(3), pp.239-242.

[48] Wei, X.Q., Man, B.Y., Liu, M., Xue, C.S., Zhuang, H.Z. and Yang, C., 2007. Blue luminescent centers and microstructural evaluation by XPS and Raman in ZnO thin films annealed in vacuum, N 2 and O 2. Physica B: Condensed Matter, 388(1), pp.145-152.

[49] Zeng, H., Duan, G., Li, Y., Yang, S., Xu, X. and Cai, W., 2010. Blue Luminescence of ZnO nanoparticles based on non-equilibrium processes: defect origins and emission controls. Advanced Functional Materials, 20(4), pp.561-572.

[50] Fu, Z., Yang, B., Li, L., Dong, W., Jia, C. and Wu, W., 2003. An intense ultraviolet photoluminescence in sol–gel ZnO–SiO2 nanocomposites. Journal of Physics: Condensed Matter, 15(17), p.2867.

[51] Willander, M., Nur, O., Sadaf, J.R., Qadir, M.I., Zaman, S., Zainelabdin, A., Bano, N. and Hussain, I., 2010. Luminescence from zinc oxide nanostructures and polymers and their hybrid devices. Materials, 3(4), pp.2643-2667.

[52] Djurišić, A.B., Leung, Y.H., Tam, K.H., Ding, L., Ge, W.K., Chen, H.Y. and Gwo, S., 2006. Green, yellow, and orange defect emission from ZnO nanostructures: Influence of excitation wavelength. Applied Physics Letters, 88(10), p.103107.

[53] Lima, S.A.M., Sigoli, F.A., Jafelicci Jr, M. and Davolos, M.R., 2001. Luminescent properties and lattice defects correlation on zinc oxide. International Journal of Inorganic Materials, 3(7), pp.749-754.

[54] Lin, B., Fu, Z. and Jia, Y., 2001. Green luminescent center in undoped zinc oxide films deposited on silicon substrates. Applied Physics Letters, 79(7), pp.943-945.

[55] Nikitenko, V., 2005. Optics and spectroscopy of point defects in ZnO. In Zinc Oxide—A Material for Micro-and Optoelectronic Applications (pp. 69-81). Springer, Dordrecht.

[56] Van de Walle, C.G., 2000. Hydrogen as a cause of doping in zinc oxide. Physical review letters, 85(5), p.1012.

[57] Janotti, A. and Van de Walle, C.G., 2007. Native point defects in ZnO. Physical Review B, 76(16), p.165202.

[58] Zwingel, D., 1972. Trapping and recombination processes in the thermoluminescence of Li-doped ZnO single crystals. Journal of Luminescence, 5(6), pp.385-405.

[59] Klingshirn, C., 1975. The luminescence of ZnO under high one-and two-quantum excitation. physica status solidi (b), 71(2), pp.547-556.

[60] Bagnall, D.M., Chen, Y.F., Shen, M.Y., Zhu, Z., Goto, T. and Yao, T., 1998. Room temperature excitonic stimulated emission from zinc oxide epilayers grown by plasma-assisted MBE. Journal of crystal growth, 184, pp.605-609.

[61] Miyake, A., Kominami, H., Tatsuoka, H., Kuwabara, H., Nakanishi, Y. and Hatanaka, Y., 2000. Growth of epitaxial ZnO thin film by oxidation of epitaxial ZnS film on Si (111) substrate. Japanese Journal of Applied Physics, 39(11B), p.L1186.

[62] Jeong, I.S., Kim, J.H. and Im, S., 2003. Ultraviolet-enhanced photodiode employing n-ZnO/p-Si structure. Applied physics letters, 83(14), pp.2946-2948.

[63] Wang, D., Seo, H.W., Tin, C.C., Bozack, M.J., Williams, J.R., Park, M., Sathitsuksanoh, N., Cheng, A.J. and Tzeng, Y.H., 2006. Effects of postgrowth annealing treatment on the photoluminescence of zinc oxide nanorods. Journal of Applied Physics, 99(11), p.113509.

[64] Greene, L.E., Law, M., Goldberger, J., Kim, F., Johnson, J.C., Zhang, Y., Saykally, R.J. and Yang, P., 2003. Low-temperature wafer-scale production of ZnO nanowire arrays. Angewandte Chemie International Edition, 42(26), pp.3031-3034.

[65] Wang, S., Mirkhani, V., Yapabandara, K., Cheng, R., Hernandez, G., Khanal, M.P., Sultan, M.S., Uprety, S., Shen, L., Zou, S. and Xu, P., 2018. Electrical characteristics and density of states of thin-film transistors based on sol-gel derived ZnO channel layers with different annealing temperatures. *Journal of Applied Physics*, *123*(16), p.161503.

Chapter 4

Formation of Depletion Layers at ZnO-ZnO Interlayer-Interfaces

4.1 Introduction

Multiple peaks were observed in transconductance of zinc oxide (ZnO) thin film transistors (TFTs), fabricated *via* sol-gel spin-coating technique, consisting multiple layers due to the deposition growth method. Sol-gel spin-coating growth method contains reiterations in the ambient. ZnO surfaces in contact with the ambient, which later evolve into ZnO-ZnO interfaces during the growth process, are discussed and depletion layers created by possible surface adsorption of ambient impurities (such as O_2) caused by surface defects are rationalized. Depletion layers may exist in other n-type metal-oxide high native point defect concentration wide band gap semiconductors deposited by sol-gel spin-coating method since the layer deposition is recurred and the chemical activity of the surface defects may cause chemisorption of O_2. The same effect may occur in other metal oxide wide band gap semiconductors fabricated *via* the same growth method.

After several decades of study, zinc oxide remains a prominent transparent wide band gap semiconductor (WBGS) for its robust structure as well as economic aspects of fabrication methods

compared to other WGBSs due to its substrate-agnostic behavior.[1,2,3] The direct gap of ZnO, combined with its high excitonic binding recombination energy[4], keeps ZnO desirable for optoelectronic applications in the blue and UV spectral region. The increase in the transparent display revenue in the forthcoming decades[5] emboldens the significance of defect and trap analysis of ZnO (and ZnO derivative) channel layers. Among the various defect types in ZnO, the omnipresence of oxygen vacancies (V_O) has been noted the earliest, considered as a color center (F center), and the origin of the yellow color of ZnO.[6,7,8] The negative formation energy as well as high stability, makes oxygen vacancies (V_O) the most frequent native defect type in ZnO.[9] Solution-process derived zinc oxide (ZnO) thin film transistors (TFT) have been widely studied due to the cost-effectiveness, simplicity and agility of the related growth methods. Device characteristics are sometimes simply reported without deep analysis. Furuta *et al.*[10] deposited ZnO *via* rf magnetron sputtering from a ZnO target at different O2 partial pressures. It was reported that in an oxygen-deficient growth-environment, a hump was observed, and the ON voltage was shifted to the left as a result of donor-like traps, at the vicinity of the conduction band, being ionized and contributing to free carriers. The hump-effect seem to be absent in ZnO and ZnO-derivative TFT reports with a single spin-coating process.[11,12,13,14] The anomalies in the mobility and transfer characteristics of ZnO TFTs involving the spin-coating process repetition, however, have either been observed in some reports but scarcely discussed[15,16], or might have been overshadowed by high OFF drain current ($I_{D,OFF}$).[17,18] In this study, the kink-effect present in the transconductance and the mobility of ZnO TFTs studied previously[19], fabricated *via* sol gel spin-coating technique, has been scrutinized and the rationale behind the creation of ZnO-ZnO interlayer-interface depletion layers has been justified.

4.2 Experimental

Three samples (1L, 4L and 8L) with different number of layers (1, 4 and 8 layers, respectively) of ZnO were fabricated *via* the spin-coating technique, with final mean thicknesses of $30\ nm$, $100\ nm$ and $190\ nm$, respectively, measured with a profilometer. The precursor was prepared by dissolving zinc acetate dehydrate in monoethanolamine (MEA) as stabilizer, diluted with isopropanol. The weight ratio of 1:1 (zinc to MEA) was attained and the precursor was stirred at 80 ℃ for 2 hours at $600\ rpm$. The precursor aged in ambient pressure and temperature in a container for 2 days. For part of the experiment, however, to achieve a functional 1-layer TFT, multiple precursors with different aging-times were tried; and for the 1 layer ZnO sample, specifically, the precursor which had aged for 9 days was used for spin-coating. All the precursors were stable, transparent and homogenous at the time of deposition. Highly conductive boron-doped silicon wafers ($0.001 \sim 0.005\ \Omega.m$) were oxidized, cleaned and used as substrates. The precursors were dropped on the substrates and spin-coated at $3000\ rpm$ for $30\ s$. To evaporate the solvents, the wafers were calcined at 300 ℃ for 5 minutes. Precursor dropping, spin-coating and calcination processes were repeated 3 and 7 times for the 4L and 8L, respectively. The samples were then annealed at 800 ℃ for 1 hour to form uniform nanocrystalline ZnO thin films. To fabricate the bottom-gate TFTs, the wafers were cut into 1 cm^2 pieces and cleaned *via* acetone, methanol and deionized water (5 min each) in ultrasonic bath. Photolithography was then performed to achieve Corbino geometry (Figure 4.1 (left)). The outer ring ($R_2 = 200\ \mu m$) was used as the source and the inner circle ($R_1 = 120\ \mu m$) was used as the drain. Due to the Corbino geometry of the devices, the channel width-to-length ratio was defined through $W/L \equiv 2\pi/\ln(R_2/R_1)$.[20] The ZnO layers may contain 1 or multiple ZnO-ZnO interlayer-interfaces (Figure 4.1 (right)). In order to reach the highly-conductive boron-doped silicon body, acting as

the back gate, the bottom SiO_2 layer was scratched with a diamond pen and the silicon body was attached to a conductive supporting plate with silver paint.

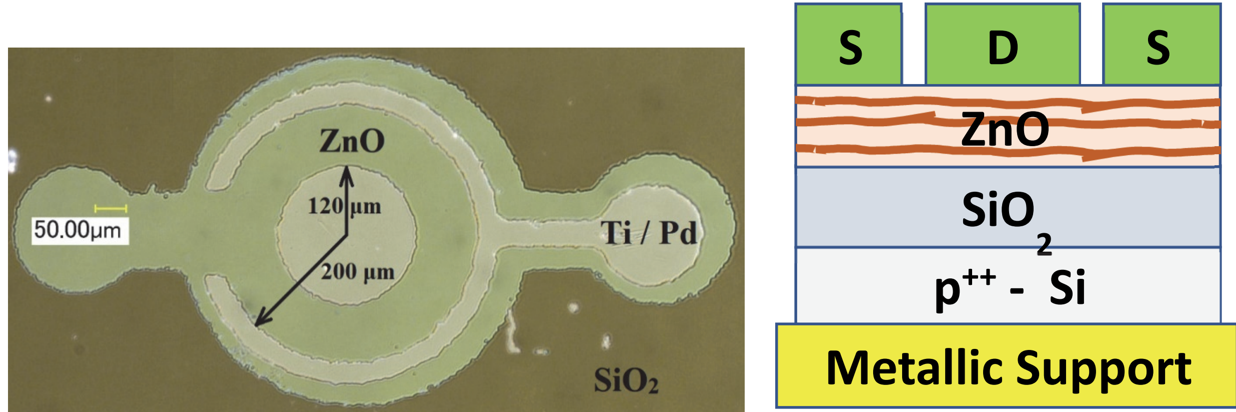

Figure 4.1: Left: Optical image of bottom-gate ZnO TFT with 4 channel layers (4L) with a mean film thickness of 100 nm on a 247 nm dry oxidized SiO_2. Right: The cross-section schematics of the Corbino bottom-gate ZnO TFTs.

The source and drain contacts were deposited *via* magnetron DC sputtering. Titanium was used for the ohmic contact and was passivated by palladium. Mesa structure was formed by photolithography and wet chemical etching, using diluted hydrochloric acid. The ZnO layers were characterized by X-ray diffraction (XRD) with a Bruker D2 Phaser X-ray diffractometer and Raman spectroscopy with the 442 nm line of a He:Cd laser, using a Jobin Yvon spectrometer. Device current-voltage (I-V) and capacitance-voltage (C-V) measurements were performed with Keithly 2400 SourceMeter, and Keithly 590CV analyzer, respectively. For each sample, the data for a representative device is provided.

4.3 Results and Discussion

The ZnO thin films were grown on silicon dioxide and were analyzed with X-ray diffraction (XRD) and Raman spectroscopy. The XRD peak at 34.5 degrees exhibited the c-axis

(0002) orientation of the nanocrystalline thin films (Figure 4.2 (left)). The Raman shift (436.8 cm^{-1}) indicated a strong E_2^{High} peak (Figure 4.2 (right)), corresponding to the oxygen vibration in the wurtzite structure.[21]

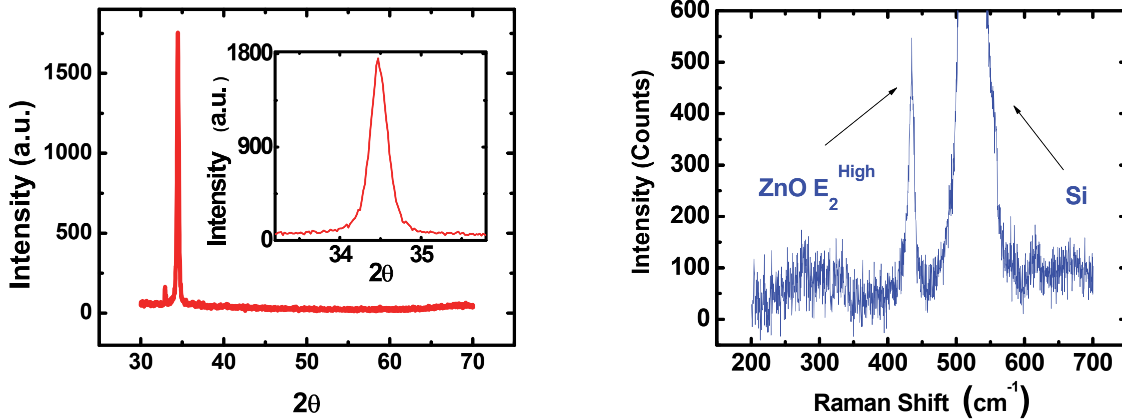

Figure 4.2: Left: X-ray Diffraction pattern obtained from the 4L ZnO sample. The smaller peak at 33 degrees represents the silicon wafer. The inset shows the 34.5 degrees peak at a higher magnification. Right: Raman shift of the 8L sample. The 436.8 cm^{-1} and 520 cm^{-1} correspond to the ZnO E_2^{High} (oxygen vibration) and the single crystal silicon wafer under the transparent silicon dioxide substrate, respectively.

Figure 4.3 presents the transistor output characteristics (I_D-V_{DS}) of the devices and Figure 4.4 shows the drain current (I_D) in a logarithmic scale and the transconductance $g_m \equiv \partial I_D / \partial V_{GS}$, in the linear region as a function of gate-source voltage bias (V_{GS}) for the three samples (1L, 4L and 8L). The devices are normally ON due to large background electron concentration. It is conjectured that the back channel starts to form just underneath the ZnO/ambient interface on top of the device as V_{GS} surpasses the ON voltage (V_{ON}). The transconductance (g_m) for all of the devices increases with an increase in V_{GS}, which is believed to be attributed to the decrease of effective grain boundary potential barrier height[22], as well as the channel charge centroid receding from the ZnO/ambient interface and hence, reduction of surface roughness scattering.[23] Figure

4.4(a) shows g_m of the single layer ZnO sample (1L), where g_m reaches a maximum. As V_{GS} increases, the channel charge centroid migrates toward the bottom gate, and due to carrier scattering caused by defects at the ZnO/SiO_2 interface, a decline in g_m is observed.[22]

In samples with higher number of layers (Figures 4.4(b) and 4.4(c)), however, a second peak is observed in g_m. The kink-effect is even more accentuated in 8L. We attribute the decline of the initial peak at $V_G = -10\ V$ to the Coulombic and defect scattering of the carriers at the ZnO-ZnO interlayer-interfaces, due to the formation of depletion regions caused by trapped charges forming a negative space-charge sheet. In general, reactions at the grain boundaries of metal-oxide semiconductors result in the formation of depletion regions on the surface, with increasing its width as the surface area to volume ratio increases.[24] In a polycrystalline form of ZnO, the interfaces of neighboring ZnO grains form double Schottky barriers at the boundary[25] where oxygen vacancies are in the diamagnetic double positively charged oxygen vacancy (V_O^{++}) states.[26] Annealing the film results in grain growth and the grain boundary effects become less significant as the number of boundaries along the c-axis decreases.

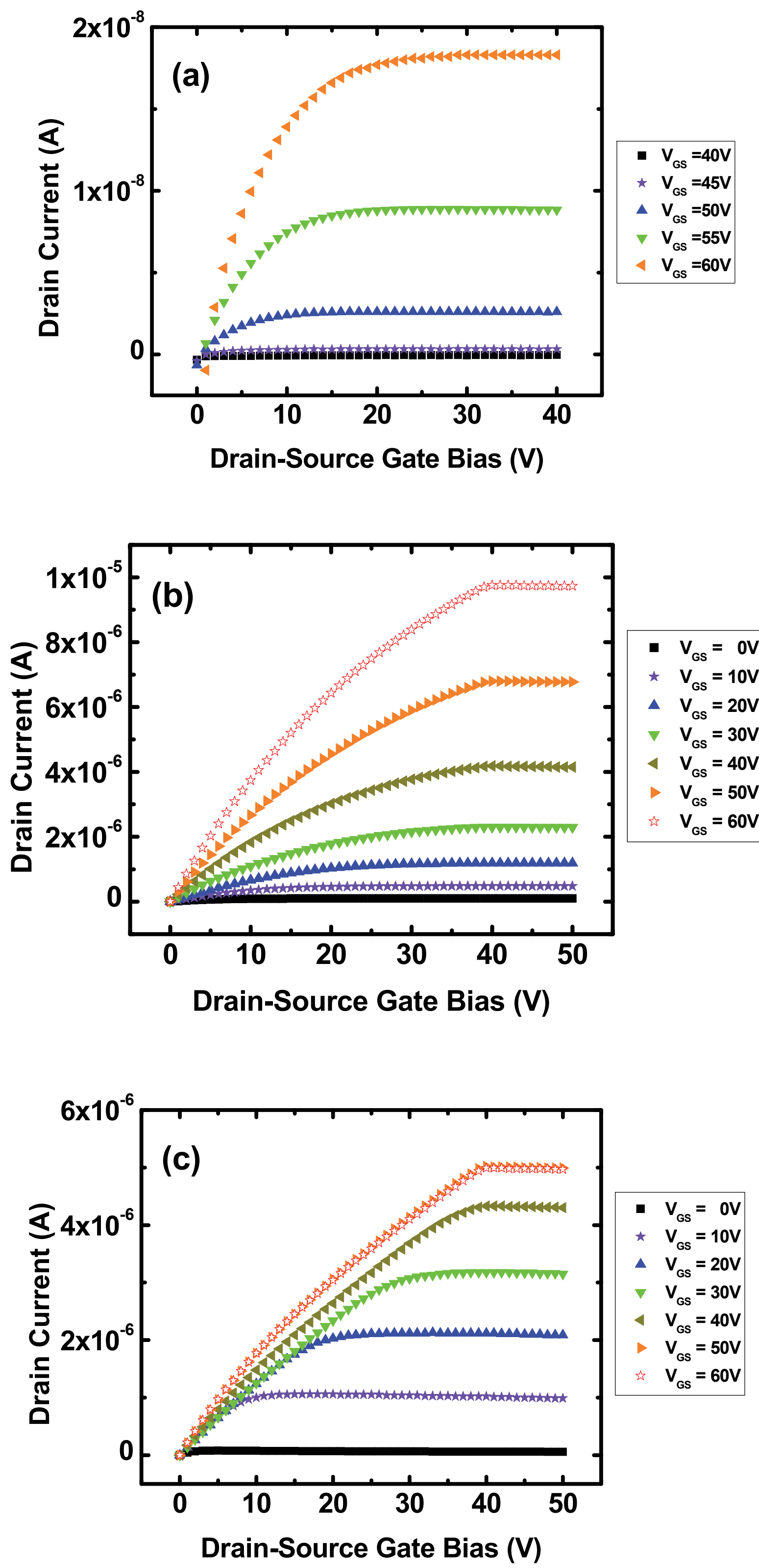

Figure 4.3: Output characteristics of samples 1L (a), 4L (b), and 8L (c).

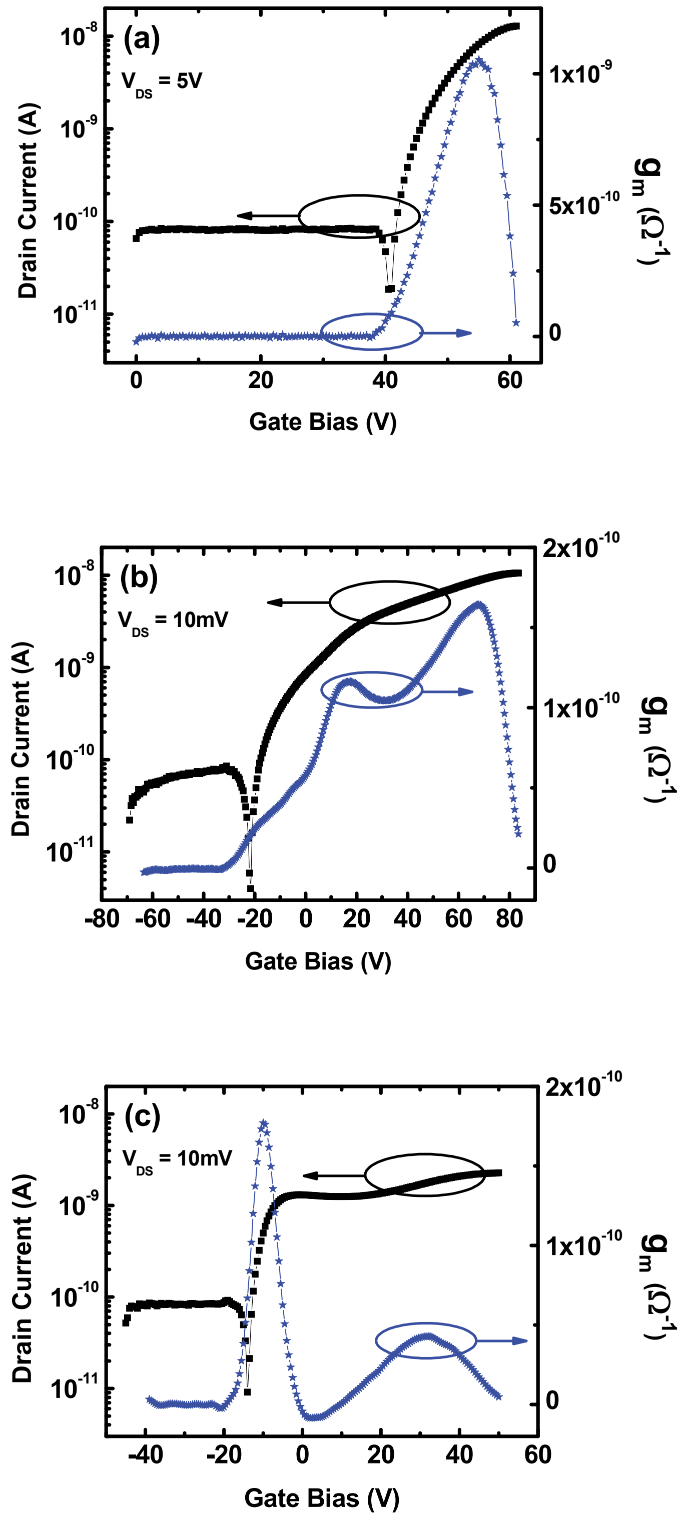

Figure 4.4: Drain current (black squares) and transconductance (blue stars) of samples 1L (a), 4L (b) and 8L (c) as a function of gate-source voltage bias. A kink effect can be observed in the transfer characteristics, as well as local maxima in the multiple layer samples.

The rationale behind the formation of the depletion layers (causing a decline in g_m and creating the first peak) comes from the adsorption of molecules from the ambient on the surface, capturing an electron from the ZnO lattice and becoming negatively charged, and creating a charge sheet. Surface defects, such as oxygen vacancies, act as active adsorption sites for ambient gas molecules.[27] Reversible behavior (physisorption) and irreversible behavior (chemisorption) can be observed during the resistance measurement of ZnO films in vacuum/ambient cycles.[28] During the sol-gel spin-coating growth process, calcination may result in a temporary reduction of physisorbed surface trapped molecules. However, physisorption and chemisorption recur before the next spin-coating process, introducing surface states.

Oxygen is one of the significant surface-adsorbed gases from the ambient. Oxygen reacts with neutral ($V_O^{\times}$) and positively charged oxygen vacancies (V_O^{+}) on the surface, capturing a conduction band electron from the ZnO lattice. This creates deep levels in the band gap and forms strongly bonded chemisorbed ions such as O^-, O^{2-} or O_2^- on the surface.[29] The only stable surface ion below $650\ K$, however, is O_2^-.[30] An O^{2-}/ O^- system reacting with V_O^{++} and V_O^{+} ensues upon photoexcitation, based on radiative and nonradiative recombinations.[31]

Besides oxygen, H_2O may also be chemisorbed and form OH^- on the surface while other gases may capture electrons and form negatively charged species on the surface as $aG + xe = A^{x-}$, where G is the gas molecule and A is the adsorbed specie.[32] Moisture is omnipresent in sol-gel processing. At ambient temperature, water molecules are adsorbed and cannot be fully desorbed from ZnO surface. This is due to the positive Gibbs free energy difference of the water molecules adsorbed to the surface.[33] Subthreshold swing (SS) measurements suggest that the defect levels are created inside the band gap as a result of oxygen and moisture adsorption.[34]

All aforementioned species remain on the surface during the subsequent spin-coating process and will form a two-dimensional depletion layer at the ZnO-ZnO interface. Although annealing increases the grain size decreases the grain boundary surface to volume ratio and eliminates a portion of mid-gap states, the chemisorbed oxygens at these boundaries create extra stable deep level trapping centers at the ZnO-ZnO interfaces.[35] In multiple layered samples, these depletion layers induce Coulomb scattering as the carriers move toward the bottom gate when V_{GS} increases.

When $V_{GS} < V_{ON}$, charge carriers are repelled from the bottom gate into the top metal contacts (source and drain) and ZnO channel layers are fully depleted. When V_{GS} surpasses V_{ON}, carriers are injected into the layers from the top. As V_{GS} increases, the channel charge centroid moves away from the ZnO/ambient interface, followed by reduction in carrier scattering. In multiple-layer samples, as the centroid go through the ZnO-ZnO interface, mobility decreases due to Coulomb scattering. This results in a kink in the transfer characteristics and a local maximum in g_m (Figures 4.4(b) and 4.4(c)). As V_{GS} increases further, the depletion region shrinks due to an increase in the donor concentration N_D ($V_O^{++}/V_O^{+} \rightarrow V_O^{\times}$).[36] Moreover, the conduction band minimum (CBM) just below the potential barrier gets closer to the fermi level as a result of the gate-induced depletion region shrinkage. At a certain critical voltage (V_C) These two factors facilitate tunneling, the carriers penetrate deeper into the channel layers and g_m increases once more before its decline due to the centroid reaching the ZnO/SiO_2 interface. Band bending as a function of V_{GS} at the ZnO/SiO_2 interface was approximated in a previous study.[37] It is believed that the local peak at $V_G = 15\ V$ in the transconductance for 4L sample may be associated with a depletion layer close to the ZnO/SiO_2 interface while a kink observed at $V_G = -15\ V$ may be related to a depletion layer closer to the upper surface (Figures 4.4(b)). This indicates that the

uniformity and the effective area of the O_2^- surface charge density may differ from a depletion layer to another, depending on the time interval the surface is exposed to the ambient during fabrication. As the number of layers increases, *e.g.* the 8L, the possibility of the formation of uniform 2D potential barriers is enhanced (Figures 4.4(c)).

Figure 4.5 presents the normalized capacitance-voltage (C-V) measurements of the samples. The gate bias (V_G) ranges in the C-V measurements which correspond to V_{GS} in the I-V measurements are all shifted to the left due to electrical gate stressing of the I-V measurements.[23] Figure 4.5 (a) shows C-V for 1L sample. Although a kink-like feature is observed at $V_G = 30\ V$, but the data is fairly noisy or possible mobile charges in the insulator or at the ZnO/SiO_2 interface.[38] For 4L, a kink can be seen at $V_G = -20\ V$ (inset of Figure 4.5 (b)), which is believed to be associated with a depletion region in the upper part of the ZnO layer. The location of the kink in C-V can be directly related to that in g_m (Figure 4.4(b)). The corresponding effect of the 2 local peak in g_m of 4L at $V_G = 15\ V$ was subtle in the C-V characteristics and could not be distinguished. The kink-effect is apparent in 8L (Figure 4.5 (c)), occurring at the same V_G range at which the local maximum transconductance occurs (Figure 4.4(c)). In this negative V_G range, one or several depletion regions hinder the carrier injection toward the oxide interface. With a surge in V_G, carriers are able to tunnel through the barriers and accumulate on lower surfaces.

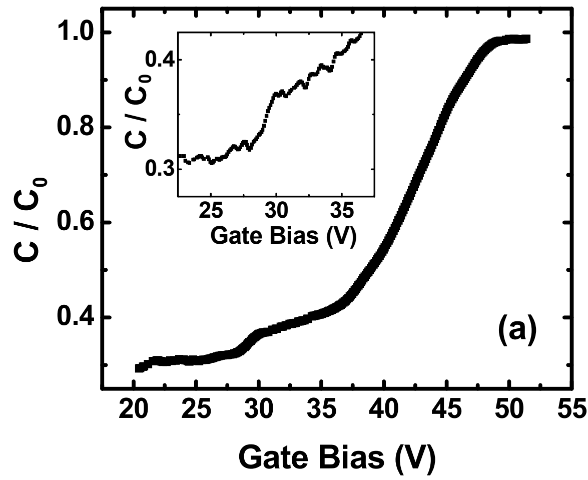

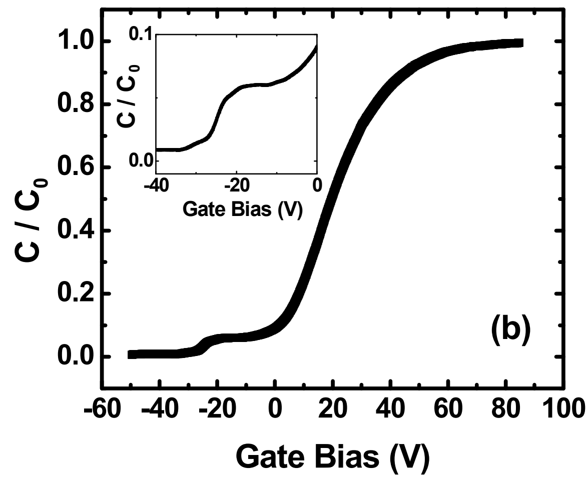

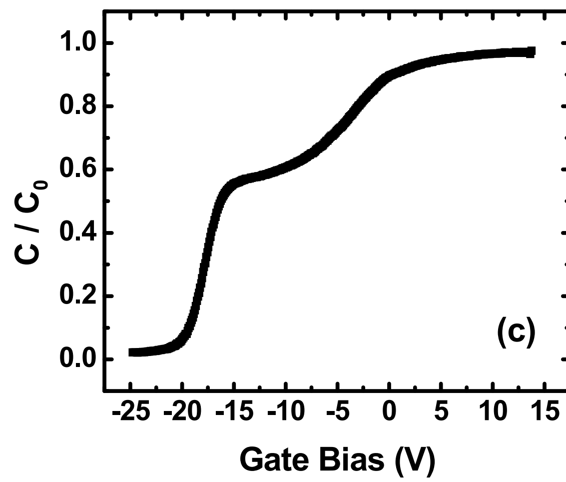

Figure 4.5: Normalized quasi-static capacitance-voltage measurements for samples 1L (a), 4L (b) and 8L (c). The insets exhibit the specific region with a higher magnification to distinguish the kink-effect in 4L (b) from a possible noise in 1L (a).

The carrier concentration (N_D) was calculated to be $2 \times 10^{18}\ cm^{-3}$ *via* linear extrapolation of the inverse of capacitance per unit area squared versus gate bias (V_G) plot of the 4L sample based on the following expression;

$$N_D = -2[q\varepsilon_{ZnO}\varepsilon_0(\frac{\partial}{\partial V_G}\frac{1}{C^2})]^{-1}$$

where C is capacitance per unit area, q is the carrier charge, ε_0 is permittivity of vacuum, and ε_{ZnO} is the static dielectric constant of ZnO ($\varepsilon_{ZnO} \approx 8.656$)[39]. The interlayer-interface built-in potential (φ_{i-i}) was then calculated to be $0.72\ V$ based on the following relation;

$$\varphi_{i-i} \approx \frac{k_B T}{q} \ln\frac{N_D}{n_i}$$

where n_i is the intrinsic carrier concentration ($10^6\ cm^{-3}$ at room temperature)[27], k_B is Boltzman's constant, and T is temperature. Our value for φ_{i-i} obtained in this study is higher than the results reported by Liao *et al*.[40] The width of a single Schottky barrier (W_D) and the screening Debye length (λ_D) can be calculated from the following equations;

$$W_D = (2\varepsilon_{ZnO}\varepsilon_0\varphi_{i-i}/\ qN_D)^{1/2}$$

$$\lambda_D = (k_B T\varepsilon_{ZnO}\varepsilon_0/N_D q^2)^{1/2}$$

where W_D and λ_D are 18.5 nm and 2.46 nm, respectively. The obtained value for W_D explains the normally OFF behavior of the 1L ZnO sample. The ZnO surface of 1L is exposed to the ambient for an extended time (considering the transistor fabrication processes) and more oxygen molecules are chemisorbed at the surface, compared to the ZnO-ZnO interlayer-interfaces of other samples where another layer is deposited on the previous layer in around 5 minutes. Therefore, W_D becomes larger for 1L and the single layer becomes fully depleted at zero gate bias.

Figures 4.6, 4.7, 4.8 and 4.9 present the potential barriers at the interlayer-interfaces in the energy band diagram, as well as the cross-section schematics of the device at different gate biases.

Depletion layer formation caused by surface oxygen chemisorption has been studied in other metal oxides such as TiO_2 and SnO_2.[41,42] Hence, the interlayer-interface barriers observed in this study may exist in the aforementioned WBGS thin films deposited *via* the sol gel spin coating method as well.[43,44]

4.4 Conclusion

In this experiment, ZnO TFTs with different number of spin-coated channel layers were fabricated. A kink or additional local maxima were observed from the transfer curve and corresponding transconductance of the TFT with multi-layered channel layers, respectively. A model was presented to explain the observed phenomena by considering formation of the depletion layer at the ZnO-ZnO interlayer-interfaces due to the oxygen chemisorption on the surface during the fabrication process. The deep level traps created due to the oxygen chemisorption are not removed by annealing at 800 ℃. The effects become more apparent as the number of layers increase. It was hypothesized that transconductance increases as the channel charge centroid moves away from the ZnO/ambient interface toward the bottom gate, followed by the decline in transconductance as the charge centroid go through the ZnO-ZnO interlayer-interface depletion regions due to Coulomb scattering. Subsequently, the transconductance increases once more as the channel charge centroid moves away from the depletion regions and the depletion width becomes smaller, and then decreases as the centroid hits the ZnO/SiO_2 interface.

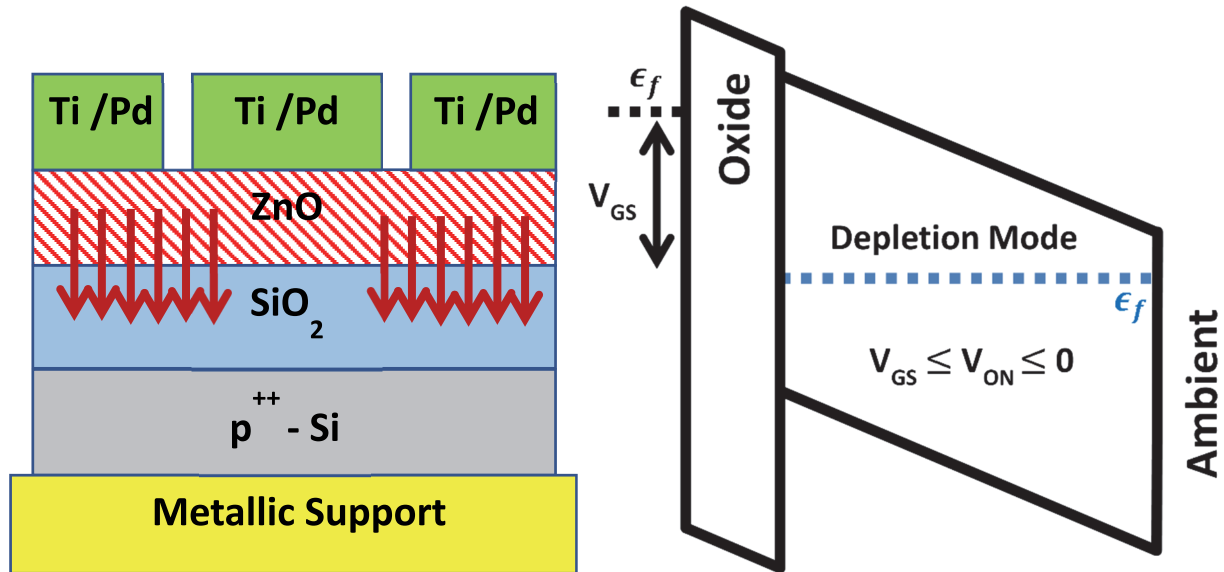

Figure 4.6: Device cross-section schematics of representation the ZnO-ZnO interlayer-interfaces with gate bias at depletion mode (left). The red arrows represent the electric field applied by the bottom gate, fully depleting the active layer (hatched area). Energy band diagram representation of the channel layer with gate bias lower than V_{ON} (right).

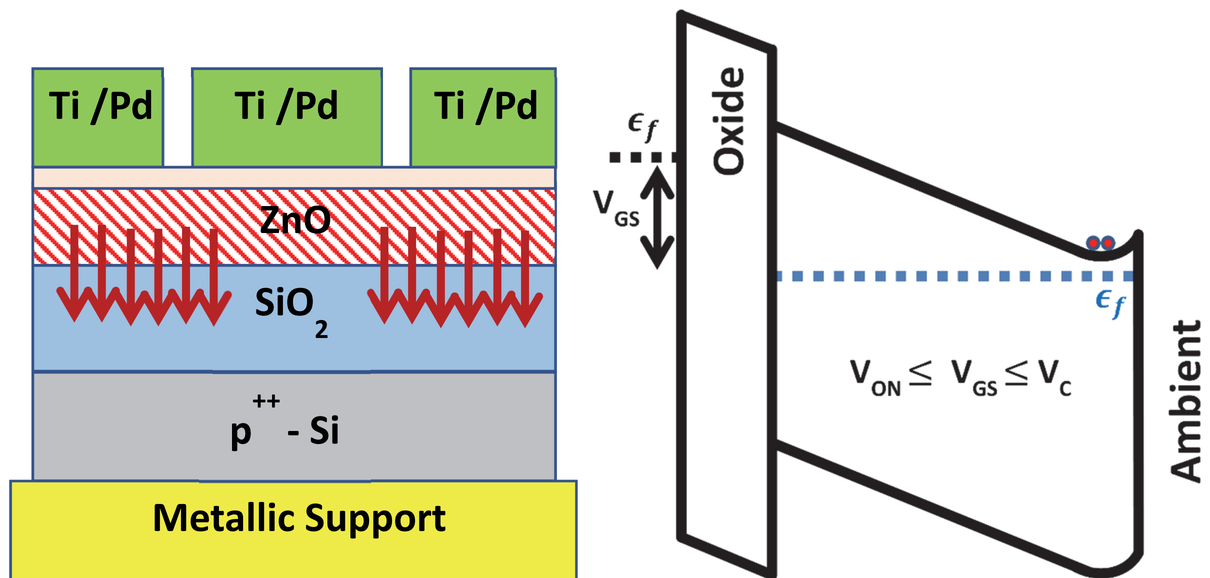

Figure 4.7: Device cross-section schematics of representation the ZnO-ZnO interlayer-interfaces with gate bias just above V_{ON} (left). The red arrows represent the electric field applied by the bottom gate, partially depleting the active layer (hatched area). Energy band diagram representation of the channel layer with gate bias just above V_{ON}, allowing carriers to form a back channel (right).

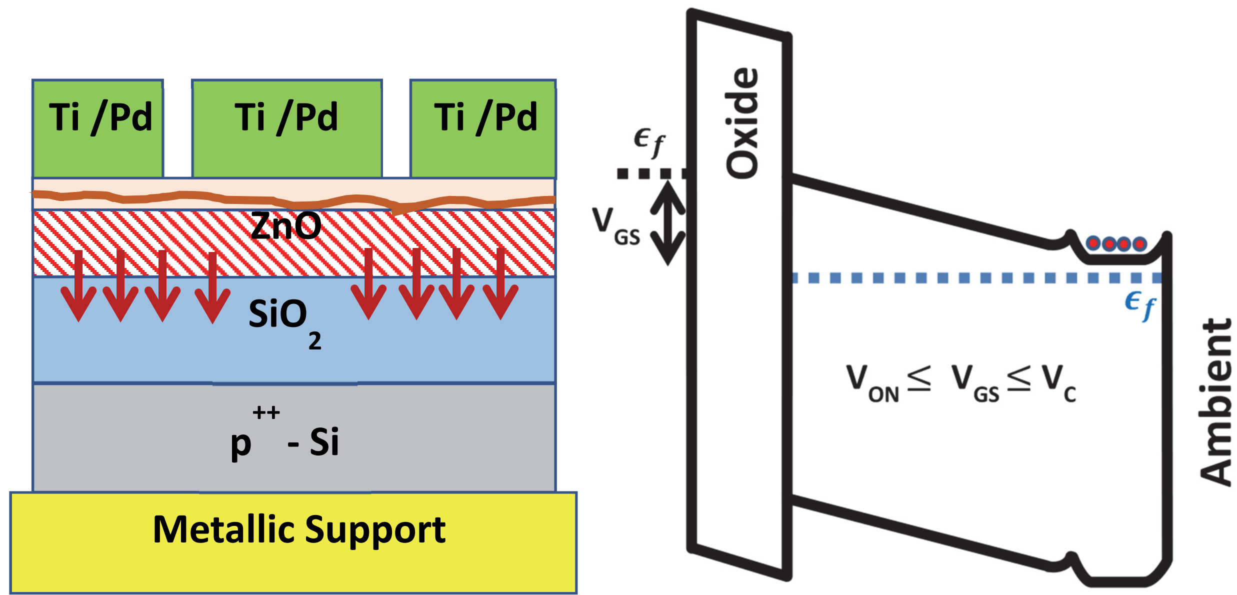

Figure 4.8: Device cross-section schematics of representation the ZnO-ZnO interlayer-interfaces (left). The red arrows represent the electric field applied by the bottom gate, depleting (hatched area) parts of the active layer just below the potential barrier at the interface. Energy band diagram representation of the channel layer with gate bias just below the critical voltage (V_C) just before the hot carriers can tunnel through the barrier (right).

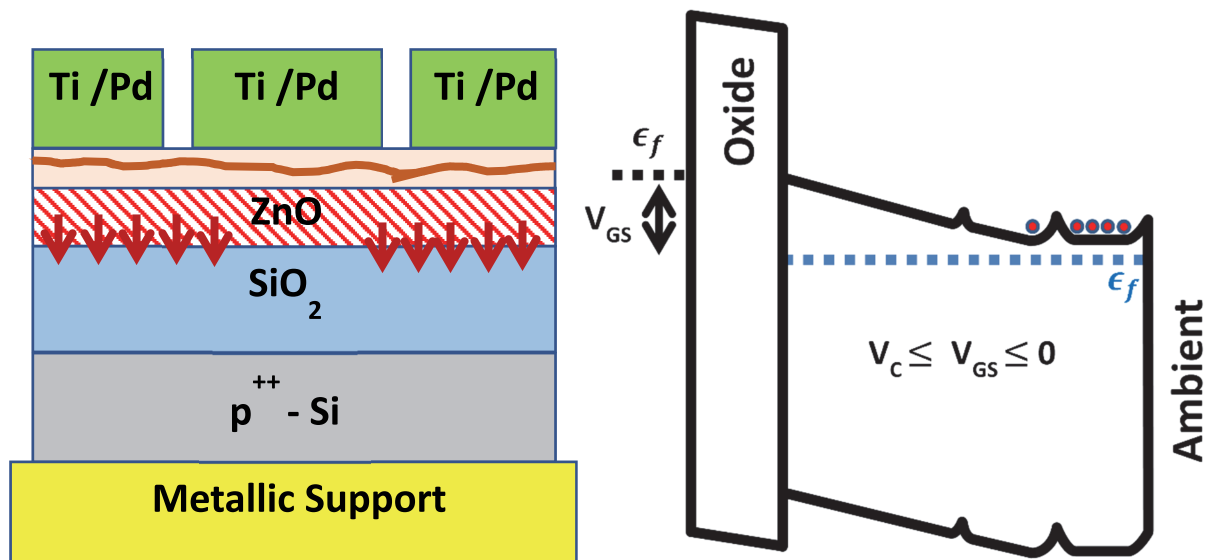

Figure 4.9: Device cross-section schematics of representation the ZnO-ZnO interlayer-interfaces (left). The red arrows represent the electric field applied by the bottom gate, depleting (hatched area) parts of the active layer well below the potential barrier at the interface. Energy band diagram representation of the channel layer with gate bias just above the critical voltage (V_C), allowing the hot carriers to tunnel through the barrier (right).

References

[1] Look, D.C., Reynolds, D.C., Hemsky, J.W., Jones, R.L. and Sizelove, J.R., 1999. Production and annealing of electron irradiation damage in ZnO. Applied Physics Letters, 75(6), pp.811-813.

[2] Auret, F.D., Goodman, S.A., Hayes, M., Legodi, M.J., Van Laarhoven, H.A. and Look, D.C., 2001. Electrical characterization of 1.8 MeV proton-bombarded ZnO. Applied Physics Letters, 79(19), pp.3074-3076.

[3] Jackson, T., 2017. Radiation Hard and Self Healing Substrate Agnostic Nanocrystalline ZnO Thin Film Electronics. PENNSYLVANIA STATE UNIV STATE COLLEGE UNIVERSITY PARK United States.

[4] Thomas, D.G., 1960. The exciton spectrum of zinc oxide. Journal of Physics and Chemistry of Solids, 15(1-2), pp.86-96.

[5] Fortunato, E., Barquinha, P. and Martins, R., 2012. Oxide semiconductor thin-film transistors: a review of recent advances. Advanced materials, 24(22), pp.2945-2986.

[6] Vehse, W.E., Sibley, W.A., Keller, F.J. and Chen, Y., 1968. Radiation damage in ZnO single crystals. Physical Review, 167(3), p.828.

[7] Locker, D.R. and Meese, J.M., 1972. Displacement thresholds in ZnO. IEEE Transactions on Nuclear Science, 19(6), pp.237-242.

[8] Ágoston, P., Albe, K., Nieminen, R.M. and Puska, M.J., 2009. Intrinsic n-type behavior in transparent conducting oxides: a comparative hybrid-functional study of In 2 O 3, SnO 2, and ZnO. Physical review letters, 103(24), p.245501.

[9] Kohan, A.F., Ceder, G., Morgan, D. and Van de Walle, C.G., 2000. First-principles study of native point defects in ZnO. Physical Review B, 61(22), p.15019.

[10] Furuta, M., Kamada, Y., Kimura, M., Hiramatsu, T., Matsuda, T., Furuta, H., Li, C., Fujita, S. and Hirao, T., 2010. Analysis of hump characteristics in thin-film transistors with ZnO channels deposited by sputtering at various oxygen partial pressures. IEEE Electron Device Letters, 31(11), pp.1257-1259.

[11] Norris, B.J., Anderson, J., Wager, J.F. and Keszler, D.A., 2003. Spin-coated zinc oxide transparent transistors. Journal of Physics D: Applied Physics, 36(20), p.L105.

[12] Seo, S.J., Choi, C.G., Hwang, Y.H. and Bae, B.S., 2008. High performance solution-processed amorphous zinc tin oxide thin film transistor. Journal of Physics D: Applied Physics, 42(3), p.035106.

[13] Park, K.B., Seon, J.B., Kim, G.H., Yang, M., Koo, B., Kim, H.J., Ryu, M.K. and Lee, S.Y., 2010. High electrical performance of wet-processed indium zinc oxide thin-film transistors. IEEE Electron Device Letters, 31(4), pp.311-313.

[14] Jeong, S., Ha, Y.G., Moon, J., Facchetti, A. and Marks, T.J., 2010. Role of gallium doping in dramatically lowering amorphous-oxide processing temperatures for solution-derived indium zinc oxide thin-film transistors. Advanced Materials, 22(12), pp.1346-1350.

[15] Sun, B. and Sirringhaus, H., 2005. Solution-processed zinc oxide field-effect transistors based on self-assembly of colloidal nanorods. Nano letters, 5(12), pp.2408-2413.

[16] Park, S.H.K., Hwang, C.S., Ryu, M., Yang, S., Byun, C., Shin, J., Lee, J.I., Lee, K., Oh, M.S. and Im, S., 2009. Transparent and Photo-stable ZnO Thin-film Transistors to Drive an Active Matrix Organic-Light-Emitting-Diode Display Panel. Advanced Materials, 21(6), pp.678-682.

[17] Ong, B.S., Li, C., Li, Y., Wu, Y. and Loutfy, R., 2007. Stable, solution-processed, high-mobility ZnO thin-film transistors. Journal of the American Chemical Society, 129(10), pp.2750-2751.

[18] Li, C.S., Li, Y.N., Wu, Y.L., Ong, B.S. and Loutfy, R.O., 2008. Performance improvement for solution-processed high-mobility ZnO thin-film transistors. Journal of Physics D: Applied Physics, 41(12), p.125102.

[19] Wang, S., Mirkhani, V., Yapabandara, K., Ko, S., Sk, M.H., Park, M. and Hamilton, M.C., 2015, June. Analysis of the effect of gamma-ray irradiation and low-temperature characteristics of sol-gel derived ZnO thin-film transistors. In Device Research Conference (DRC), 2015 73rd Annual (pp. 171-172). IEEE.

[20] Giraldo, A., Paccagnella, A. and Minzoni, A., 2000. Aspect ratio calculation in n-channel MOSFETs with a gate-enclosed layout. Solid-State Electronics, 44(6), pp.981-989.

[21] K.A. Alim, V.A. Fonoberov, M. Shamsa, A.A. Balandin, J. Appl. Phys. 97 (2005) 124313.

[22] Hoffman, R.L., 2004. ZnO-channel thin-film transistors: Channel mobility. Journal of Applied Physics, 95(10), pp.5813-5819.

[23] Koga, J., Takagi, S. and Toriumi, A., 1994, December. A comprehensive study of MOSFET electron mobility in both weak and strong inversion regimes. In Electron Devices Meeting, 1994. IEDM'94. Technical Digest., International (pp. 475-478). IEEE.

[24] Sze, S.M. and Ng, K.K., 2006. Physics of semiconductor devices. John wiley & sons, p.765

[25] Cordaro, J.F., Shim, Y. and May, J.E., 1986. Bulk electron traps in zinc oxide varistors. Journal of applied physics, 60(12), pp.4186-4190.

[26] Vanheusden, K., Seager, C.H., Warren, W.T., Tallant, D.R. and Voigt, J.A., 1996. Correlation between photoluminescence and oxygen vacancies in ZnO phosphors. Applied Physics Letters, 68(3), pp.403-405.

[27] Sukkar, M.H., Johnson, K.H. and Tuller, H.L., 1990. Defects and electronic structure of interfaces in ZnO: Cluster molecular orbital calculations. Materials Science and Engineering: B, 6(1), pp.49-59.

[28] Chaabouni, F., Abaab, M. and Rezig, B., 2004. Metrological characteristics of ZnO oxygen sensor at room temperature. Sensors and Actuators B: chemical, 100(1), pp.200-204.

[29] Lagowski, J., Sproles Jr, E.S. and Gatos, H.C., 1977. Quantitative study of the charge transfer in chemisorption; oxygen chemisorption on ZnO. Journal of Applied Physics, 48(8), pp.3566-3575.

[30] Göpel, W., 1978. Reactions of oxygen with ZnO–$10\bar{1}0$-surfaces. Journal of Vacuum Science and Technology, 15(4), pp.1298-1310.

[31] van Dijken, A., Meulenkamp, E.A., Vanmaekelbergh, D. and Meijerink, A., 2000. The kinetics of the radiative and nonradiative processes in nanocrystalline ZnO particles upon photoexcitation. The Journal of Physical Chemistry B, 104(8), pp.1715-1723.

[32] Jones, A., Jones, T.A., Mann, B. and Firth, J.G., 1984. The effect of the physical form of the oxide on the conductivity changes produced by CH4, CO and H2O on ZnO. Sensors and Actuators, 5(1), pp.75-88.

[33] Erol, A., Okur, S., Comba, B., Mermer, Ö. and Arıkan, M.C., 2010. Humidity sensing properties of ZnO nanoparticles synthesized by sol–gel process. Sensors and Actuators B: Chemical, 145(1), pp.174-180.

[34] Yapabandara, K., Mirkhani, V., Sultan, M.S., Ozden, B., Khanal, M.P., Park, M., Wang, S., Hamilton, M.C., Chung, Y., Kim, D.J. and Sk, M.H., 2017. Study of device instability of bottom-gate ZnO transistors with sol–gel derived channel layers. Journal of Vacuum Science & Technology B, Nanotechnology and Microelectronics: Materials, Processing, Measurement, and Phenomena, 35(3), p.03D104.

[35] Kumar, S., Gupta, V. and Sreenivas, K., 2005. Synthesis of photoconducting ZnO nano-needles using an unbalanced magnetron sputtered ZnO/Zn/ZnO multilayer structure. Nanotechnology, 16(8), p.1167.

[36] Liao, Z.M., Zhang, H.Z., Zhou, Y.B., Xu, J., Zhang, J.M. and Yu, D.P., 2008. Surface effects on photoluminescence of single ZnO nanowires. Physics Letters A, 372(24), pp.4505-4509.

[37] Wang, S., Mirkhani, V., Yapabandara, K., Cheng, R., Hernandez, G., Khanal, M.P., Sultan, M.S., Uprety, S., Shen, L., Zou, S. and Xu, P., 2018. Electrical characteristics and density of states of thin-film transistors based on sol-gel derived ZnO channel layers with different annealing temperatures. Journal of Applied Physics, 123(16), p.161503.

[38] Blom, F.R., Van de Pol, F.C.M., Bauhuis, G. and Popma, T.J., 1991. RF planar magnetron sputtered ZnO films II: Electrical properties. Thin Solid Films, 204(2), pp.365-376.

[39] Pearton, S.J., Norton, D.P., Ip, K., Heo, Y.W. and Steiner, T., 2005. Recent progress in processing and properties of ZnO. Progress in materials science, 50(3), pp.293-340.

[40] Liao, Z.M., Liu, K.J., Zhang, J.M., Xu, J. and Yu, D.P., 2007. Effect of surface states on electron transport in individual ZnO nanowires. Physics Letters A, 367(3), pp.207-210.

[41] Rothschild, A., Levakov, A., Shapira, Y., Ashkenasy, N. and Komem, Y., 2003. Surface photovoltage spectroscopy study of reduced and oxidized nanocrystalline TiO2 films. Surface science, 532, pp.456-460.

[42] Kohl, D., 1989. Surface processes in the detection of reducing gases with SnO2-based devices. Sensors and actuators, 18(1), pp.71-113.

[43] Liao, Y.H. and Chou, J.C., 2009. Preparation and characterization of the titanium dioxide thin films used for pH electrode and procaine drug sensor by sol–gel method. Materials Chemistry and Physics, 114(2-3), pp.542-548.

[44] Diana, T., Devi, K.N. and Sarma, H.N., 2010. On the optical properties of SnO2 thin films prepared by sol-gel method. Indian Journal of Physics, 84(6), pp.687-691.

Chapter 5

Gamma Irradiation Effects on Sol-Gel Derived Thin Film Transistors

5.1 Introduction

Solution-based bottom-gate zinc oxide thin film transistors (TFTs) were successfully fabricated, remaining functional and demonstrating stability under extreme gamma irradiation conditions. Zinc oxide was used as the active channel layer and was kept unpassivated. The devices were fabricated on samples with different number of layers grown *via* sol-gel spin coating technique. The devices were then measured before and after being exposed to 1.2 MGy (120 Mrad (air)) and an additional 1 MGy (total 2.2 MGy) of gamma irradiation on the same devices. Device characteristics were extracted from the current-voltage measurements. The zinc oxide films were characterized by photoluminescence and Atomic Force Microscopy (AFM) before and after irradiation. The degradation/enhancement of device characteristics such as saturation mobility, drain current on/off ratio and threshold voltage shift before and after irradiation is discussed.

Wide band gap semiconductor (WBGS) devices are of great interest in high power electronics due to their high breakdown voltage and efficiency. Due to its high device efficiency at room temperature (k_BT = 26 meV) among other direct WBGS exciton binding energies, such as 4H-SiC (20 meV), GaN (25 meV) and ZnSe (22 meV), ZnO is an exemplary candidate for

excitonic emission applications.[1,2,3] ZnO has been exploited in power electronics[4], transparent electronics[5], sensing applications[6,7,8], UV-visible down-shifting applications[9], and nano-sized piezotronics[10], generators[11] and modifiers[12,13,14].

Radiation-resistant devices are utilized in various research areas such as space applications and high energy accelerators. Research on structural stability and device characteristics of different semiconductors under gamma irradiation is a growing field, in the search for a radiation-hard substitution for silicon.[15,16,17,18,19,20] Silicon based devices indicate drastic decline under gamma irradiation (with doses as small as 20 kGy)[21,22] and therefore, radiation-hard silicon devices have been scrutinized in the past couple of decades.[23,24,25] Yet, the intrinsic radiation-hardness of ZnO is superior to hardened-silicon or other robust materials such as gallium nitride.[26] Despite the fact that investigations on structural hardness and stability of ZnO devices against irradiation by energetic particles such as electrons[27,28,29,30,31], protons[32,33], neutrons[34,35] and ions[36,37,38] have been reported, the gamma ray irradiation is far from being mature and further research is required. High energy irradiation introduces point defects, as a consequence of Compton scatterings, if the particle energy surpasses displacement energy of lattice atoms.[39] Atomic displacement damage for zinc and oxygen (in wurtzite ZnO) has been reported by several groups. Locker and Meese reported the threshold energies of incoming particles to initiate displacement damage for oxygen and zinc atoms, in wurtzite ZnO, to be 310 keV and 900 keV, respectively.[40] They also claimed the atomic displacement energy (E_d) of 57 eV for both zinc and oxygen atoms. Lorenz *et al.*[41] estimated E_d (Zn)=65 eV and E_d (O)=50 eV. These values are well above the average atomic displacement energies of other WBGSs such as: E_d (Si)=12.9 eV, E_d (Ge)=14.5 eV, E_d (GaAs)=9.5 eV, E_d (GaN)=19.5 eV and E_d (4H-SiC)=21.3 eV.[42]

The energies of the gamma rays from ^{60}Co decay, 1.17 and 1.33 MeV, surpass the displacement threshold energy required for both atoms and therefore, introduction of vacancies and interstitial point defects is expected. Jackson *et al.*[43] reported several successful gamma ray irradiation experiments on bottom-gate ZnO TFTs fabricated *via* pulsed laser deposition (PLD) and plasma-enhanced atomic layer deposition (PEALD). The group reported functional transistors with a slight negative threshold voltage shift after being irradiated by 1 MGy gamma irradiation without being electrically biased during irradiation. An improvement was observed after annealing at 200ºC for 1 minute, removing the radiation induced voltage shifts.[44] The experiment was repeated under electrical bias during irradiation, confirming the radiation resistance of ZnO TFTs.[45,46] This experiment further investigates the radiation-hardness of ZnO thin films and ZnO-based TFTs under gamma irradiation. Atomic force microscopy (AFM) and photoluminescence (PL) were conducted on the films and current-voltage (I-V) measurements of the TFTs were employed. The ZnO TFTs were fabricated *via* sol-gel spin coating technique. Despite the disadvantages of the sol-gel derived devices such as high operating voltages[47], the growth process is an attractive deposition method among researchers due to its simplicity and cost-effectiveness. Unlike growth processes which require ultra-high vacuum and/or high deposition temperature, sol-gel spin-coating technique can be utilized in the ambient. Sol-gel spin coating technique was utilized by Nishio *et al.*[48] to deposit transparent conductive Al-doped ZnO thin films, and by Natsume *et al.*[49] to grow undoped ZnO films, for the first time. Norris *et al.* [50] reported the fabrication of fully transparent thin film transistors (TTFTs) on a glass substrate by spin coating zinc nitrate solution, using indium tin oxide as the transparent bottom-gate contact and a superlattice of Al_2O_3 and TiO_2 (ATO) deposited *via* Atomic Layer Deposition (ALD) as the gate insulator. In this project, to best of our knowledge, the gamma-ray irradiation of sol-gel derived

bottom-gate ZnO TFTs was performed for the first time. Fabricated TFTs were characterized before irradiation, were then radiated *via* ^{60}Co radiation source (rate of 388.3 mGy/s) with a total dose of 1.2 MGy, and were characterized again. After characterization, the devices were radiated by an additional 1 MGy (total 2.2 MGy) radiation dose, surpassing the highest doses previously reported for irradiation of ZnO TFTs fabricated *via* other growth methods. The devices were characterized once more to evaluate the ionization and displacement damage effects on the TFTs induced by irradiation.

5.2 Experimental

The semiconductor was grown using the sol-gel spin-coating method by dropping the solution on the substrate followed by calcining the wafer. The precursor was prepared as mentioned in Chapter 3, to yield a clear, homogenous and stable solution. As the conductive substrate, two heavily-boron-doped silicon wafers (0.01 – 0.02 ohm.cm) were cleaned by acetone, methanol and deionized (DI) water, followed by hydrofluoric (HF) acid to remove possible redundant surface oxide. The wafers were then dry oxidized in order to achieve the bottom gate oxide layers (170 nm silicon dioxide). The precursor was then dropped on the oxidized wafers and rotated at 3000 rpm for 30 s. The coated wafers were then calcined at 285 ºC for 5 minutes to remove the organic residuals through evaporation. The dropping process was repeated 3 times on one wafer (resulting in a 4-layer ZnO film) and 7 times on the other wafer (resulting in an 8-layer ZnO film). The wafers were then annealed at 800 ℃ in ambient air for 1 hour to accommodate the formation of ZnO nanocrystallines through coalescence. The film thicknesses were measured to be ranging from 90 nm to 105 nm by profilometry for the 4-layer wafer (4L), and from 183 nm to 196 nm for the 8 layer wafer (8L). A single 1 cm x 1 cm piece was chosen from the center of each wafer for circular TFT fabrication (central circle for drain and outer ring for source). Circular

source and drain (S/D) patterns were achieved by photolithography on the samples. Titanium, passivated by molybdenum and palladium, was deposited as the ohmic source and drain (S/D) contacts *via* DC magnetron sputtering. The *rationale* behind the S/D metallic structure emerged from the deterioration of titanium/aluminum contacts in a previous study.[51] The deterioration may come from the lower atomic displacement threshold energy for aluminum (~16 eV)[52] compared to palladium (~34 eV).[53] The devices on each sample where then isolated *via* wet-etching by using hydrochloric acid (HCl), forming a mesa structure, in order to minimize the gate oxide leakage current. To reach the conductive silicon bottom gate contact, the backside of the wafer was simply scratched with a diamond pen and silver paint was applied to attach the bottom gate to a metallic substrate for a convenient measurement. The samples were irradiated by gamma rays through exposure to cylindrical ^{60}Co rods to achieve total doses of 1.2 MGy and 2.2 MGy. Device measurements and analysis were conducted before and after irradiation to compare the irradiation effects in the ambient. The ZnO film on each wafer was characterized by room temperature photoluminescence (PL) with a 325 nm laser line (20mW) from a He-Cd laser. Current-voltage (I-V) measurements of the devices were acquired with a Keithley 2400 SourceMeter.

5.3 Results and Discussion

Several TFT devices from each sample (one sample from the 4L wafer and another from 8L wafer) were measured before and after irradiation for output and transfer characteristics. Two devices were chosen from each sample to represent the general behavior of the set. Devices from the 4L wafer (4L-1 and 4L-2) were measured before irradiation (referred to as Un-4L-1 and Un-4L-2 hereafter) and measured again after being irradiated by gamma irradiation doses of 1.2 MGy (referred to as 120-Irr-4L-1 and 120-Irr-4L-2 hereafter) and 2.2 MGy (referred to as 220-Irr-4L-1 and 220-Irr-4L-2 hereafter). Similarly, the unirradiated devices measured from the 8L wafer will

be referred to as Un-8L-1 and Un-8L-2. These devices will be referred to as 120-Irr-8L-1 and 120-Irr-8L-2 after 1.2 MGy irradiation, and 220-Irr-8L-1 and 220-Irr-8L-2 after 2.2 MGy irradiation.

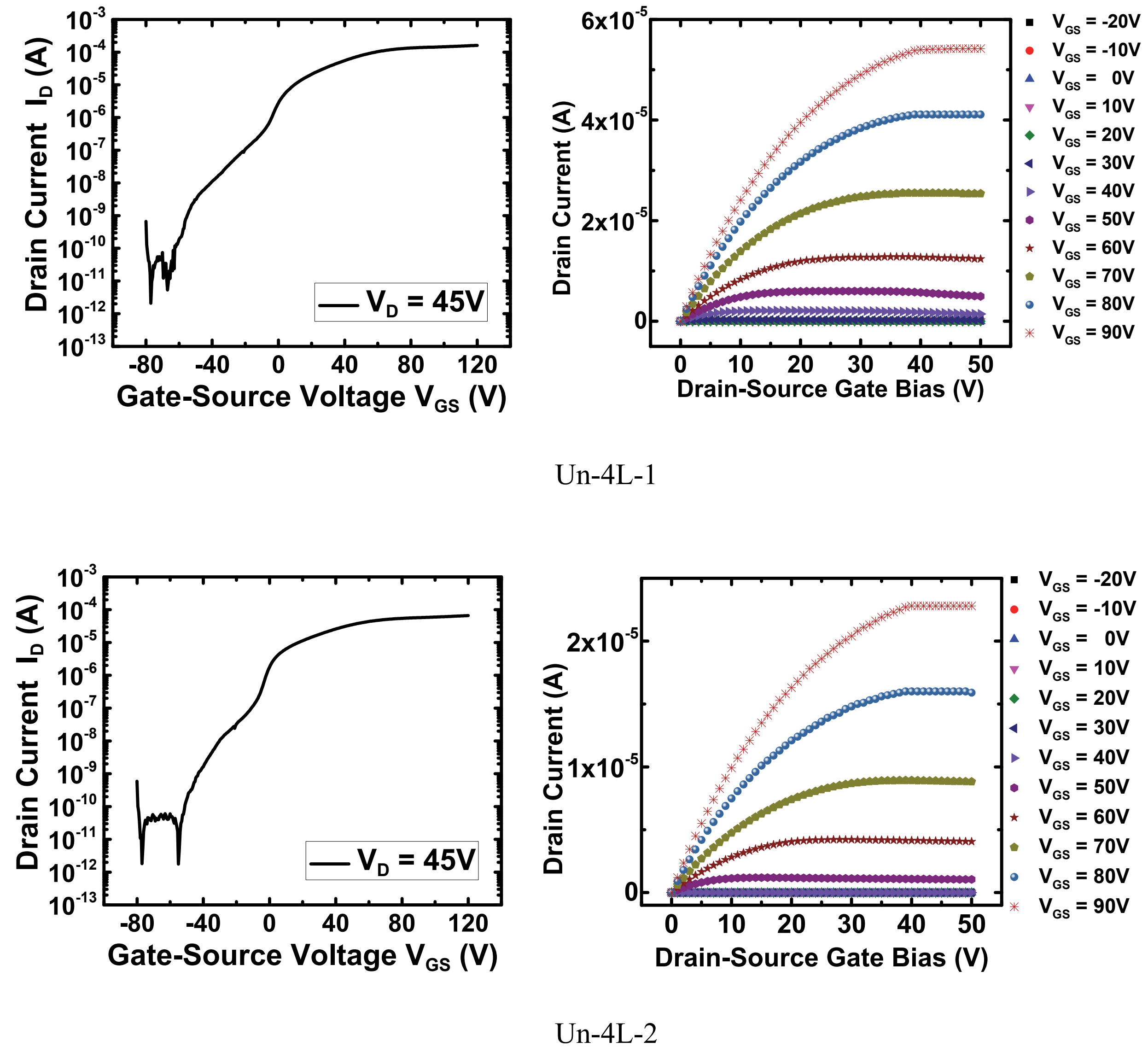

Figure 5.1: Characteristics of the devices from 4L wafer before irradiation. Top: Output (right) and saturation transfer (left) curves for Un-4L-1. Bottom: Output (right) and saturation transfer (left) curves for Un-4L-2.

Figure 5.1 presents the output curves (drain current I_D vs. drain-source voltage bias V_{DS}) and transfer curves (drain current I_D vs. gate-source voltage bias V_{GS}) for Un-4L-1 and Un-4L-2.

After 1.2MGy irradiation, the characteristic curves for these devices (120-Irr-4L-1 and 120-Irr-4L-2) are represented in Figure 5.2. The output characteristic curves indicate stability of the devices after irradiation in the saturation region.

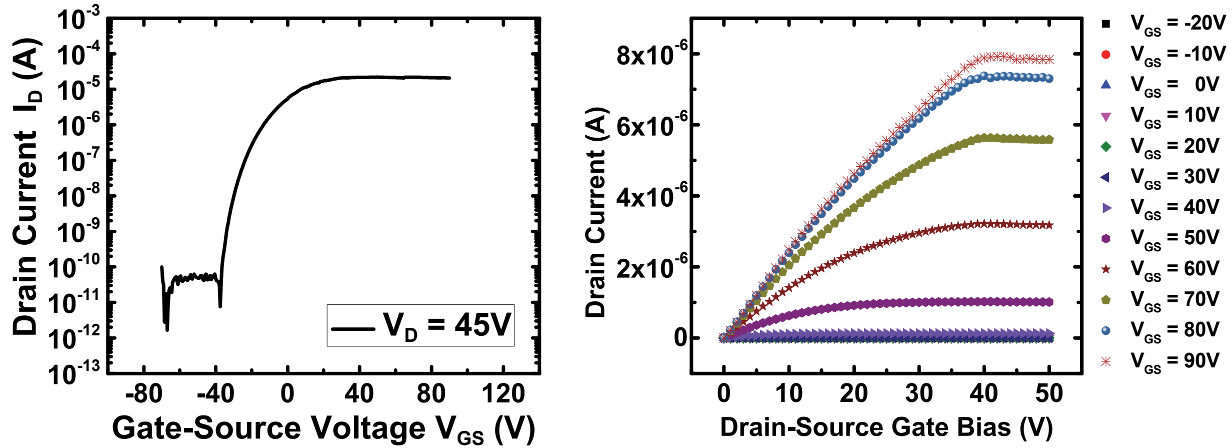

120-Irr-4L-1

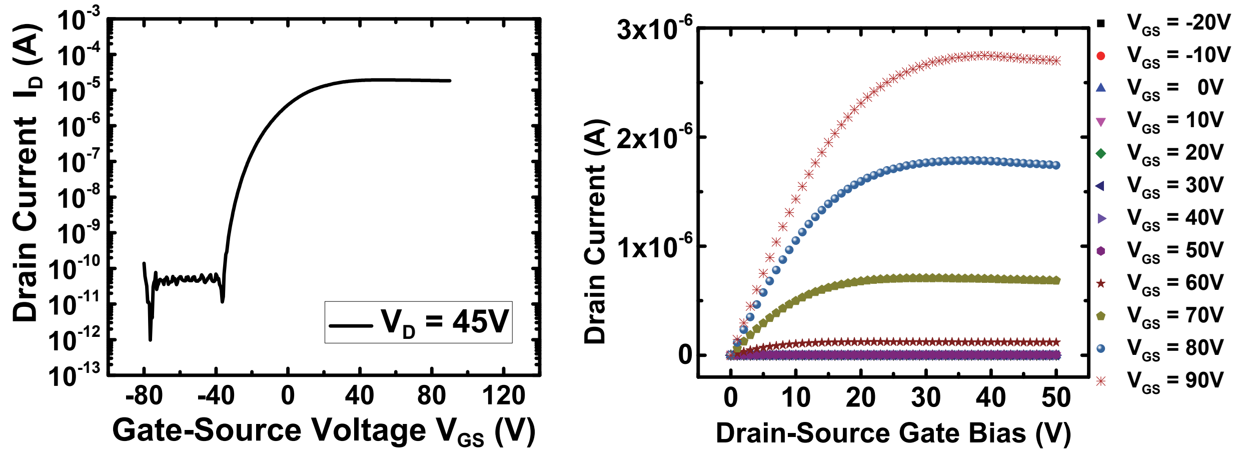

120-Irr-4L-2

Figure 5.2: Characteristics of the devices from 4L wafer after 1.2 MGy irradiation. Top: Output (right) and saturation transfer (left) curves for 120-Irr-4L-1. Bottom: Output (right) and saturation transfer (left) curves for 120-Irr-4L-2.

After 1 MGy additional irradiation dose (2.2 MGy total), the 4L devices (220-Irr-4L-1 and 220-Irr-4L-2) became dysfunctional, plausibly due to active layer thickness reduction caused by

displacement damage to the surface atoms. After 2.2 MGy irradiation, the remaining thin ZnO film becomes fully depleted due to surface oxygen chemisorption. The device could not be turned ON at low gate biases, and higher biases (~60 V) caused the gate insulator to permanently break down.

A few device characteristics such as threshold voltage (V_{th}), drain current ON-OFF ratio (I_{ON}/I_{OFF}) and maximum saturation mobility (μ_{sat}) were extracted from the saturation transfer region. Saturation mobility (μ_{sat}) was obtained at $V_{DS} = 45\ V$ from

$$\mu_{sat}(V_{GS}) = \frac{2}{C_{ox}} \times \left(\frac{W}{L}\right)^{-1} \times {m_{sat}}^2$$

where C_{ox} is the gate oxide capacitance per unit area, $\frac{W}{L}$ is the channel's width-to-length ratio and $m_{sat} \equiv \frac{\partial\sqrt{I_{D,sat}}}{\partial V_{GS}}$ with $I_{D,sat}$ being the drain current in saturation region.[54] Due to the circular shape of the devices, $\frac{W}{L} \equiv \frac{2\pi}{\ln\frac{R_2}{R_1}}$ where R_1 is the drain radius (inner circle) and R_2 is the inner radius of the source (outer ring).[55] I_{OFF} in this work is defined by the average drain current at voltages below the ON voltage (V_{ON}) and I_{ON} is defined by the average saturated current measured in transfer characteristics in saturation region. Despite the ambiguity during the extraction of the threshold voltage (V_{th}) for ZnO TFTs,[56] V_{th} was roughly approximated by linear extrapolation from the $\sqrt{I_{D,sat}}$ vs. V_{GS} curve. In the subthreshold region of the unirradiated devices (Figure 5.1), an abnormality was observed. This abnormality is rectified after 1.2 MGy irradiation (Figure 5.2). We relate this phenomenon to the formation of depletion layers at the ZnO-ZnO interlayer-interfaces caused by oxygen chemisorption during fabrication.[57,58] Oxygen is an avid ambient adsorbent on ZnO surfaces and by forming negative surface ions, the height of Schottky barrier at the ZnO/ambient interface is further increased.[59] The potential barriers

formed at the ZnO-ZnO interlayer-interfaces have been seemingly distorted due to displacement damage occurred in the bulk after irradiation.

Table 5.1 summarizes the data results for devices 4L-1 and 4L-2 for an unirradiated/irradiated sample comparison. Both devices from the 4L wafer indicated similar trends. V_{th} in the fabricated TFTs is unstable, seemingly due to shallow trap states at the insulator/semiconductor interface proximity or the unpassivated semiconductor/ambient interface which may cause a positive shift (acceptor-like traps)[60] or a negative shift (depopulation of donor-like traps).[61]

Table 5.1: Device characteristics of 4L-1 and 4L-2 before and after irradiation. The arrows indicate the enhancement/decline of the value compared to the unirradiated sample.

	μ_{sat} $(cm^2/V.s)$	I_{ON}/I_{OFF}	V_{th} (V)	I_{ON} (A)
Un-4L-1	0.173	2.6×10^7	-12.4	1.4×10^{-4}
120-Irr-4L-1	0.0657 ↓	6.1×10^5 ↓	-23.8 ↓	2.2×10^{-5} ↓
220-Irr-4L-1	——	——	——	——
Un-4L-2	0.164	3.2×10^7	-19.8	5.7×10^{-5}
120-Irr-4L-2	0.0518 ↓	1.2×10^6 ↓	-22.5 ↓	1.9×10^{-5} ↓
220-Irr-4L-2	——	——	——	——

After irradiation, V_{th} was shifted toward negative, suggesting the creation of gate-oxide states by ionization damage, acting as hole traps in the oxide bulk. These states inside oxide bulk trap holes and create fixed positive charges inside the oxide, shift the Fermi level in the gate metal contact and cause a band bending at the SiO_2/ZnO interface. These fixed charges can only be detrapped *via* thermal annealing. Whereas these trap states may have been originated by the creation of point defects, the radiation damage was not sufficient to affect I_G after 1.2 MGy irradiation dose, even through high V_{GS} biases. The average I_{OFF} remained unchanged, implying the stability of the source-drain and gate-channel leakage currents.[62] A decrease in I_{ON} in all 4-

layer devices was observed, resulting in an overall exacerbation in I_{ON}/I_{OFF}. Displacement damage dealt by gamma rays towards the surface layer reduces the thickness of the film as well as increasing the surface roughness and the surface area by gradually deforming or even removing the surface atoms from the structure.[63,64,65] Surface defects in ZnO, specifically oxygen vacancies, act as active adsorption sites for ambient gas molecules.[66] Consequently, in addition to the thinning of the channel, the total depletion region below the exposed surface area increases due to additional chemisorption of oxygen ions and the channel resistance becomes higher due to electron concentration reduction.[67] Noting the formation of the back-channel at the ZnO/ambient interface in the subthreshold region, the surface roughness and Coulomb scattering (by the depletion region formed at the ZnO/ambient interface) are the primary causes of carrier scattering and hence, the decline in saturation mobility (μ_{sat}). These issues prevail in 4-layer devices, due to the lower thickness of the channel layer, but are overshadowed by aspects in the 8-layer devices, after 1.2 MGy. After an additional 1 MGy (2.2 MGy), the 8-layer devices experience the mechanisms in the 4-layer devices, due to the active layer etching.

Figure 5.3, Figure 5.4 and Figure 5.5 represent the output and transfer curves for the devices from the 8-layer wafer before irradiation (Un-8L-1 and Un-8L-2), and after 1.2 MGy irradiation (120-Irr-8L-1 and 120-Irr-8L-2), and after 2.2 MGy irradiation (220-Irr-8L-1) respectively. Device properties of the 8-layer devices (8L-1 and 8L-2) are summarized in Table 5.2 for an overall comparison between device performances before and after irradiation. After 2.2 MGy irradiation, the second 8L sample (220-Irr-8L-2) became dysfunctional after the insulator breakdown at a gate bias of -60 eV.

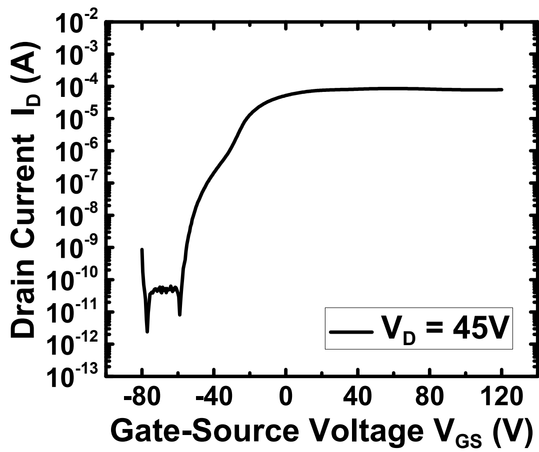

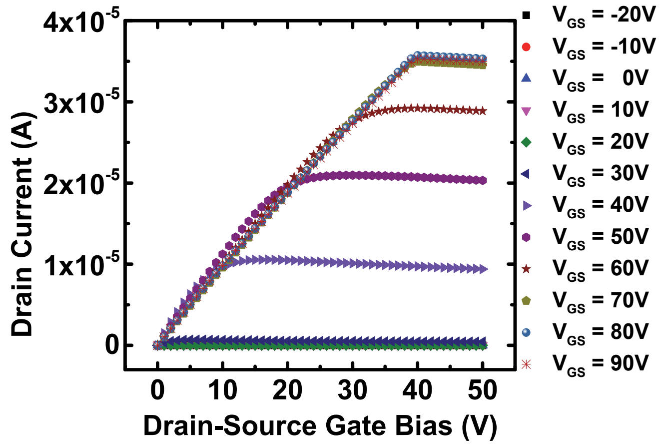

Un-8L-1

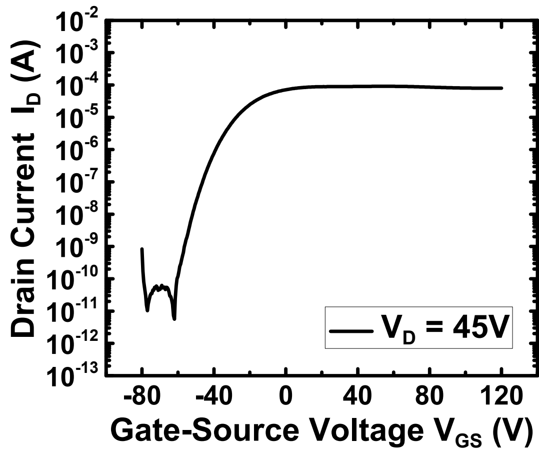

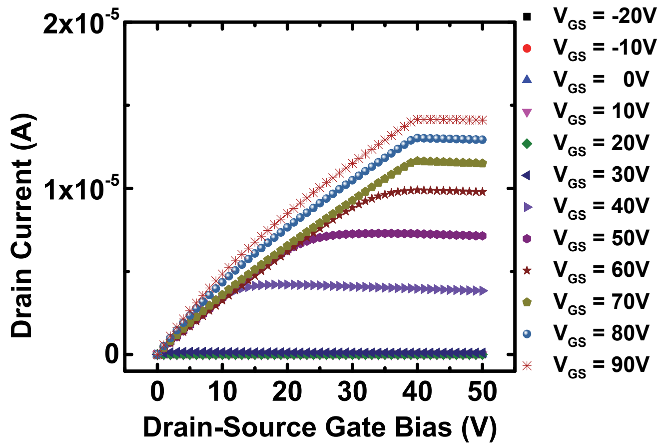

Un-8L-2

Figure 5.3: Characteristics of the devices from 8L wafer before irradiation. Top: Output (right) and saturation transfer (left) curves for Un-8L-1. Bottom: Output (right) and saturation transfer (left) curves for Un-8L-2.

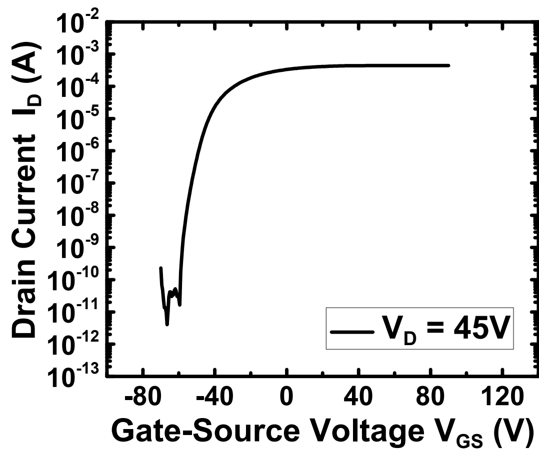

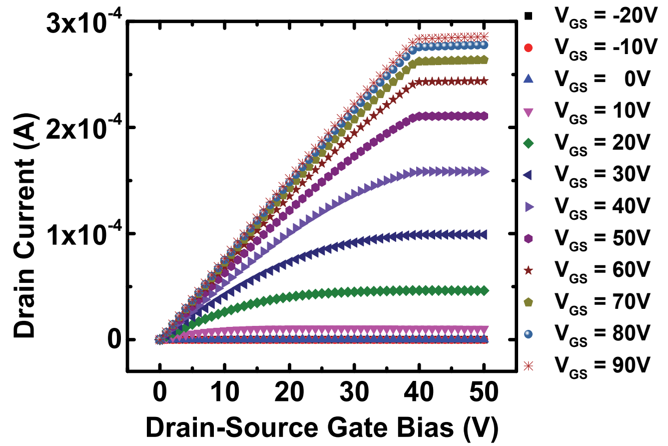

120-Irr-8L-1

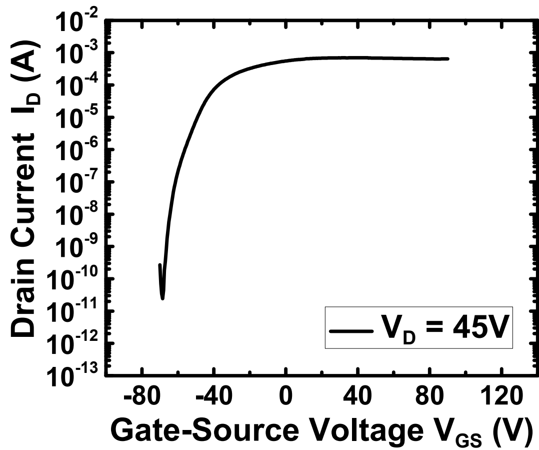

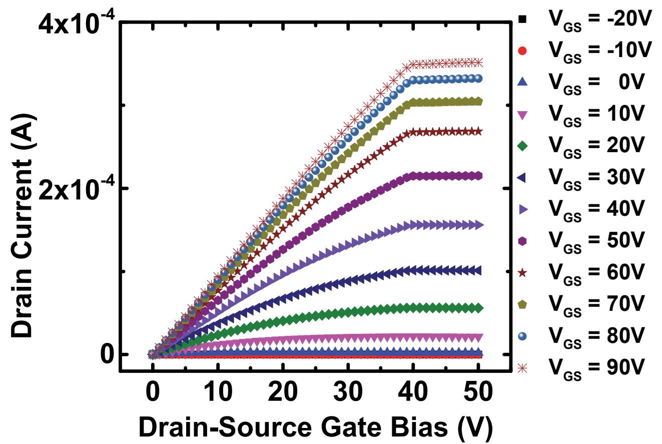

120-Irr-8L-2

Figure 5.4: Characteristics of the devices from 8L wafer after 1.2 MGy irradiation. Top: Output (right) and saturation transfer (left) curves for 120-Irr-8L-1. Bottom: Output (right) and saturation transfer (left) curves for 120-Irr-8L-2.

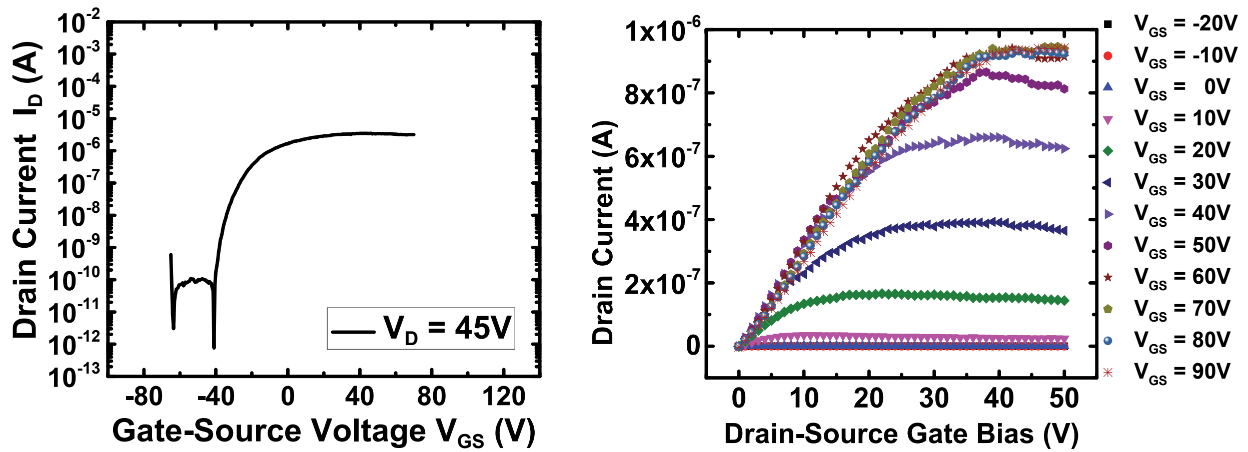

Figure 5.5: Characteristics of the devices from 8L wafer after 2.2 MGy irradiation. Top: Output (right) and saturation transfer (left) curves for 220-Irr-8L-1. The gate insulator of the other device, 220-Irr-8L-2, experienced a permanent break down due to the high gate voltage bias.

Although less apparent in the 8-layer devices, the aforementioned abnormality in the subthreshold region in the unirradiated samples can be noticed (Figure 5.3). After irradiation, interlayer-interface effects become less significant and the abnormality can hardly be recognized (Figure 5.4 and Figure 5.5).

After 1.2 MGy gamma irradiation, similar to the 4-layer devices, V_{th} is shifted for all 8-layer devices confirming the formation of radiation-induced oxide interface hole trap states, created by point defects. A boost in I_{ON} is present in all 8-layer devices, increasing I_{ON}/I_{OFF} in all devices. The creation of new point defects such as zinc interstitials (Zn_i) and neutral oxygen vacancies (V_O), caused by displacement damage, could contribute to shallow donor concentration and therefore be a conceivable reason for the enhancement of I_{ON}. Effects such as electron-hole pair generation caused by high energy radiation can also enhance conductivity.[68] The origin behind intrinsic n-type conductivity of ZnO has been controversial and has been attributed to shallow donors such as oxygen vacancies (V_O)[69], zinc-interstitial nitrogen-antisite (Zn_i-N_O) complexes[70],

hydrogen impurities in interstitial sites[71] and in oxygen vacancy sites[72], and also to other possible impurities.[73]

Furthermore, in all 8-layer sample devices, mobility has increased after irradiation. This signifies induced effects in the bulk, which are dominated by surface effects in the thinner film (4-layer) sample. The carriers are significantly depopulated in the 4-layer sample, imposed by the depletion region under the surface. A strongly viable candidate for the mobility enhancement is the distortion of the potential barriers at ZnO-ZnO interlayer-interfaces. These barriers hinder the carriers and cause Coulomb scattering, reducing the carrier mean-free-path.

After the additional 1 MGy radiation (2.2 MGy total dose), the trend observed in the 4-layer sample devices after 1.2 MGy radiation can be observed in the 8-layer sample (220-Irr-8L-1): a decline in I_{ON}/I_{OFF} and μ_{sat}. This is expected since the thickness of the channel layer has been reduced is such a way that surface effects now dominate the bulk effects. Also, V_{th} experienced a positive shift, suggesting creation of more ZnO/SiO_2 interface states acting as acceptor-like traps. When filled, acceptor-like states become negatively charged. The electric field of filled acceptor-like traps compensates the electric field caused by positive charges in the gate insulator induced by gamma-rays' ionization damage.

Table 5.2: Device characteristics of 8L-1 and 8L-2 before and after irradiation. The arrows indicate the enhancement/decline of the value compared to the unirradiated sample.

	μ_{sat} $(cm^2/V.s)$	I_{ON}/I_{OFF}	$V_{th}\,(V)$	I_{ON} (A)
Un-8L-1	0.576	1.1×10^7	-34.5	8.6×10^{-5}
120-Irr-8L-1	1.789 ↑	2.7×10^7 ↑	-50.5 ↓	4.4×10^{-4} ↑
220-Irr-8L-1	0.007 ↓	1.7×10^4 ↓	-40.0 ↑	3.41×10^{-6} ↓
Un-8L-2	0.338	1.6×10^7	-41.5	9.1×10^{-5}
120-Irr-8L-2	2.194 ↑	2.9×10^7 ↑	-55.0 ↓	7.0×10^{-4} ↑
220-Irr-8L-2	——	——	——	——

Figure 5.6 depicts the morphology of the devices after being irradiated (compare with the unirradiated sample in Figure 4.1 (left) in Chapter 4), taken by a KEYENCE High Resolution Digital Optical Microscope. The ZnO/SiO_2 step is more distinguished in the 8L sample due to its larger thickness. In addition to the etching mechanism described shortly, the deterioration of the films can be linked to two major factors: (i) the films are not passivated and (ii) the crystalline size is small as an outcome of the deposition method; whereas unexposed films[74] and single crystals[75] are expected to be more radiation-resistant.

Crude profilometry measurements suggested an increase in the overall surface roughness after irradiation. Therefore, Atomic Force Microscopy (AFM) was conducted on samples, acquiring a fine texture. Figure 5.7 exhibits the surface topology of the sample from the 4L wafer before irradiation, as well as the ZnO/SiO_2 step.

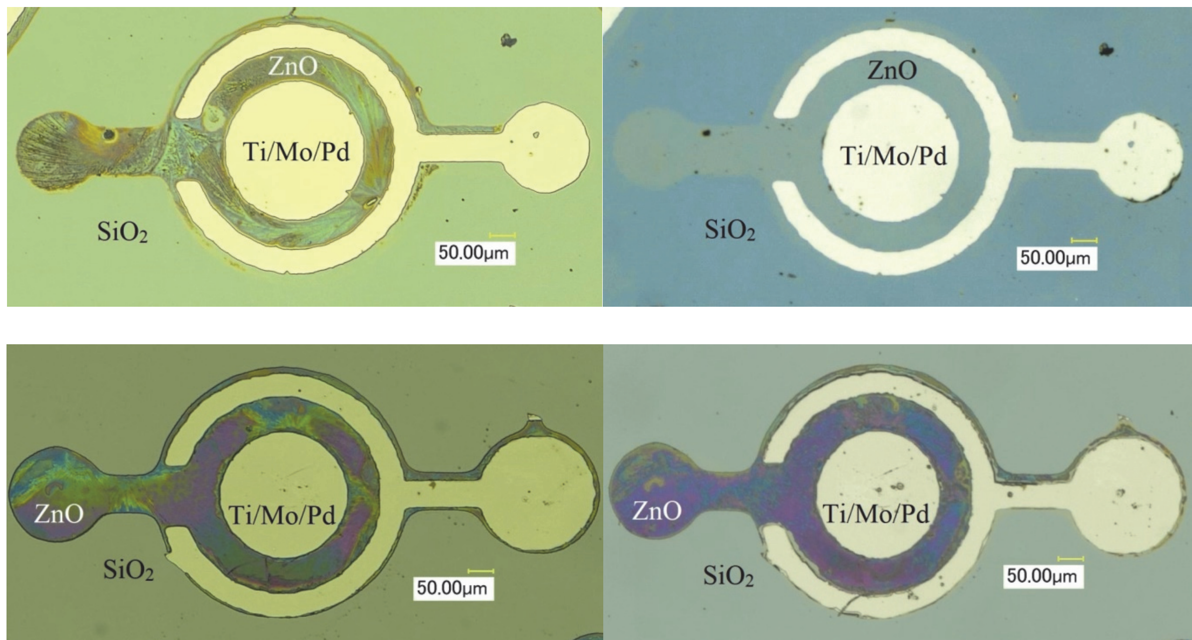

Figure 5.6: Optical microscope top view of irradiated circular TFTs from the samples: 4L sample after 1.2 MGy (Top Left), 4L sample after 2.2 MGy (Top Right), 8L sample after 1.2 MGy (Bottom Left), 8L sample after 2.2 MGy (Bottom Right).

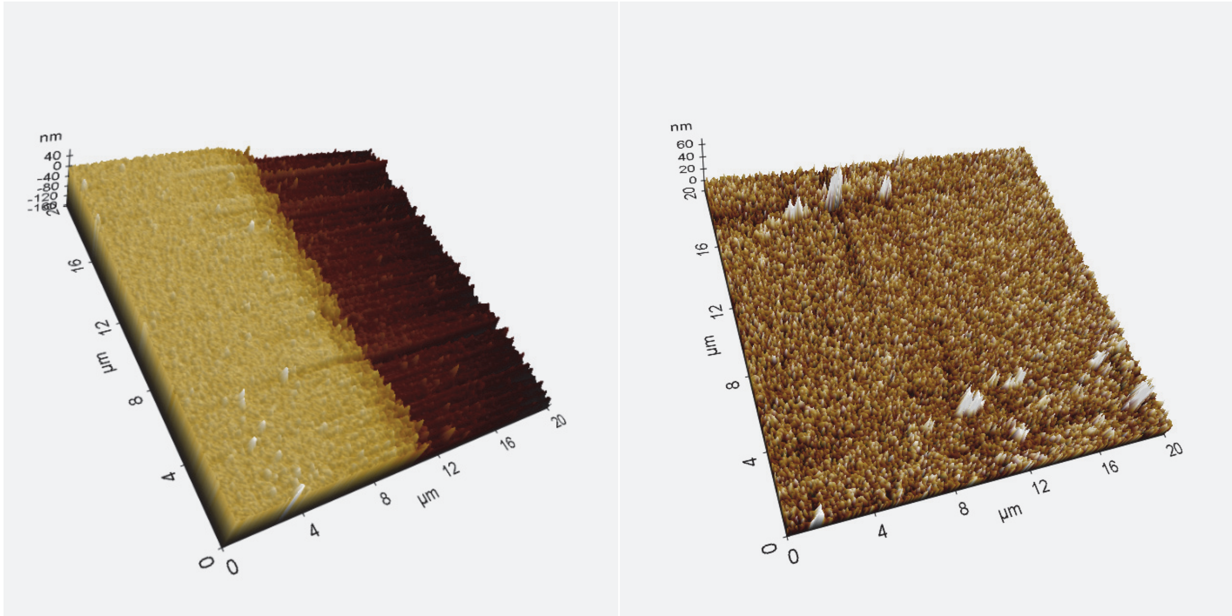

Figure 5.7: AFM of the ZnO/SiO_2 edge (left) and ZnO film surface topography (right) of pristine sample from 4L wafer.

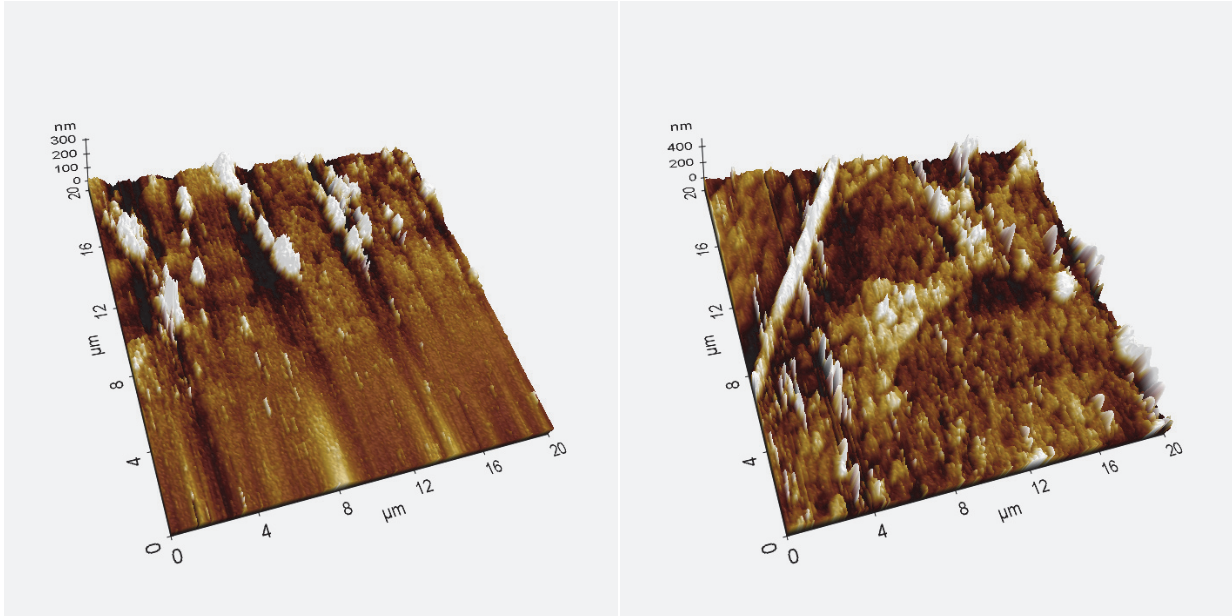

Figure 5.8: AFM of the 4L sample after 1.2 MGy gamma irradiation. The ZnO/SiO_2 edge (left) and the ZnO film surface topography (right).

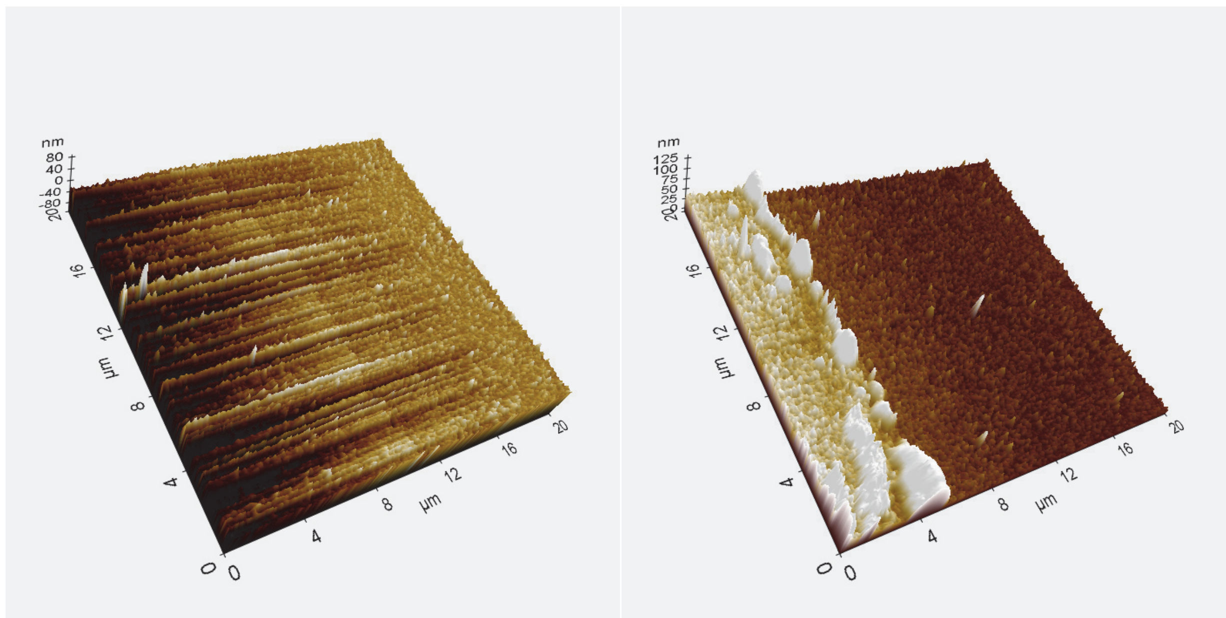

Figure 5.9: AFM of the 4L sample ZnO/SiO_2 edge after 2.2 MGy gamma irradiation from 2 different regions (left and right). The faint tilted-vertical border line at the center of the image (left) is the ZnO/SiO_2 edge.

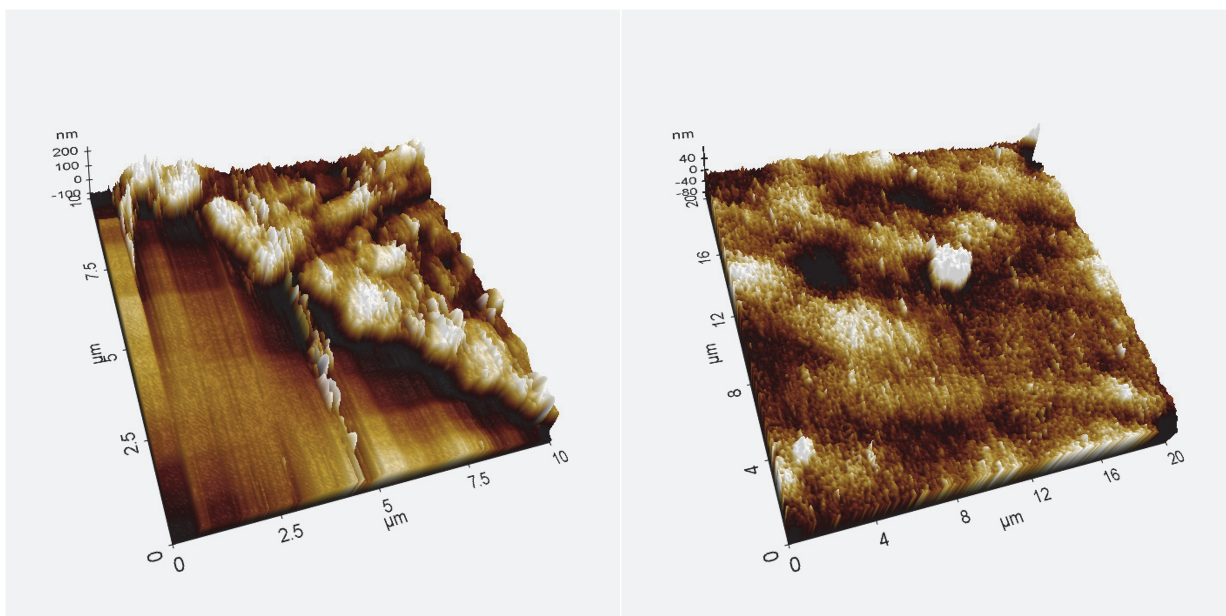

Figure 5.10: AFM images of the sample from the 8L wafer after 1.2 MGy gamma irradiation dose: the ZnO/SiO_2 edge (left) and the surface topography (right).

Figure 5.8 shows the 4L sample after 1.2 MGy gamma irradiation. The ZnO/SiO_2 edge deterioration and the roughening of ZnO film surface suggest the removal of surface atoms. In the AFM images of the 4L sample after the additional irradiation and total dose of 2.2 MGy gamma irradiation (Figure 5.9), the ZnO/SiO_2 edge becomes hard to identify in some regions (Figure 5.9 (left)), confirming the reduction of film thickness.

Figure 5.10 presents the topography of the 8L sample and the ZnO/SiO_2 step after 1.2 MGy irradiation. Considering the similarity of the pristine 8L surface topography to the pristine 4L sample, the deformation and the increase in surface roughness is noticeable after 1.2 MGy gamma irradiation. The ZnO/SiO_2 step is more distinguishable due to the higher thickness of the film. Gamma irradiation effects on layer and device characteristics depend on the total dose, as well as the crystal quality. For low gamma ray irradiation doses (< 30 kGy), in addition to an increase in surface roughness, mobility enhancement has been observed in indium zinc oxide (IZO) polycrystalline films.[76,77,78]

Here, an etching mechanism is proposed as one of the consequences of displacement damage. When high energy photons (gamma rays) with energies as high as 1.17 and 1.33 MeV penetrate the ZnO film, the photon "collide" with an electron through Compton scattering. If the photon is scattered at an angle θ from its initial path, the outgoing photon's energy (E_{out}) can be obtained from the scattering angle θ and the incoming photon's energy (E_{in}) *via*

$$E_{out} = \frac{E_{in}}{1 + \varepsilon(1 - \cos\theta)}$$

where ε is a constant, defined by

$$\varepsilon \equiv \frac{E_{in}}{m_e c^2} \cong \frac{E_{in}}{511\ eV}$$

where m_e is the stationary mass of an electron, and c is the universal constant for speed of light in vacuum. The scattered electron acquires the rest of the remainder of the energy (Figure 5.11), which can also be derived from the four-momentum conservation law to be

$$E_{C,K}(E_i, \theta) = E_{in} \frac{2\varepsilon \, sin^2 \frac{\theta}{2}}{1 + 2\varepsilon \, sin^2 \frac{\theta}{2}}.$$

where $E_{C,K}(E_i, \theta)$ is the outgoing electron's energy. As a result, the maximum energy transferred to the outgoing electron is

$$E_{C,K_{max}} = E_{in} \frac{2\varepsilon}{1 + 2\varepsilon}.$$

As the magnitude of ε, which is directly proportional to E_{in}, increases, the ratio $\frac{2\varepsilon}{1+2\varepsilon}$ gets closer to 1. Therefore, the maximum energy an electron can acquire through Compton scattering can approach 1.17 and 1.33 MeV if the scattered photons angle $\theta \approx \pi$.

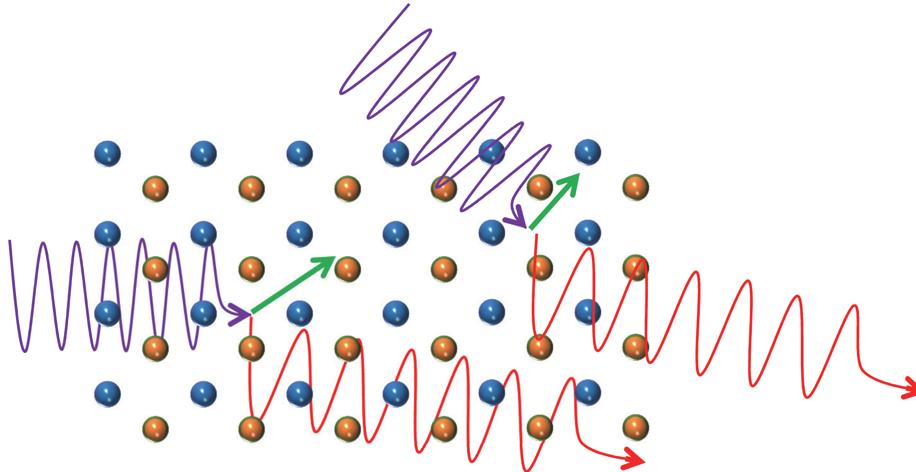

Figure 5.11: Compton scattering inside ZnO lattice. The orange and blue sphere represent O and Zn atoms. The incoming photons (violet arrows) collide with electrons inside the lattice. The outgoing photons (red arrows) have a smaller energy, transferring momentum to energetic electrons (green arrows).

For maximum effect on the lattice, we will consider that the maximum energy is transferred to the Compton-scattered electron (photoelectrons). These energetic photoelectrons may then collide with the nuclei in the lattice and displace a chain of atoms (Figure 5.12). Due to their high velocity, the collision is relativistic and the transferred energy to a nucleus (E_T) can be obtained from

$$E_T = \frac{2E_{in}{}' \, (E_{in}{}' + m_e c^2)}{Mc^2}.$$

where $E_{in}{}'$ is the incoming relativistic electron's energy and M is the atomic mass of the nucleus. The displaced atoms then collide with other lattice atoms, causing a displacement chain. The transferred energy to an outgoing nucleus (T_E) from an incoming non-relativistic nucleus is

$$T_E = \frac{4\, M_{Zn}\, M_O}{(M_{Zn} + M_O)^2}\, E_T$$

where E_T is the incoming nucleus' energy, M_{Zn} is the atomic mass of zinc and M_O is the atomic mass of oxygen. In order for atomic displacement to occur, the incoming particle's energy must surpass the threshold atomic displacement energy discussed earlier (E_d~57 eV). But also, if the number of displaced atoms is small ($n \leq 2$), the displaced atoms can migrate to a vacancy and the damage can be "healed". If multiple atoms ($n \geq 5$) are displaced, the defects will be stable. As a result, in order to observe a stable defect in a sublattice, the incoming particles, photons in this case, must have a threshold energy. To initiate stable displacement damage (green circle in Figure 5.13) to the oxygen (zinc) sublattice in wurtzite ZnO, incoming particles with energies higher than 310 keV (900 keV) are required. And if the displacement chain occurs near the surface, there is a possibility of surface atoms going through a ballistic ejection, leaving the lattice (red circle in Figure 5.13). As the radiation dose increases, the number of electrons acquiring energies above 900 keV, as well as the number of chain displacement occurring close to the surface, increases. Eventually, the active layer will be etched atom by atom and the surface effects, such as depletion

region below the surface due to surface chemisorption, become dominant against the bulk effects, such as the distortion of the potential barriers at the ZnO-ZnO interlayer-interfaces.

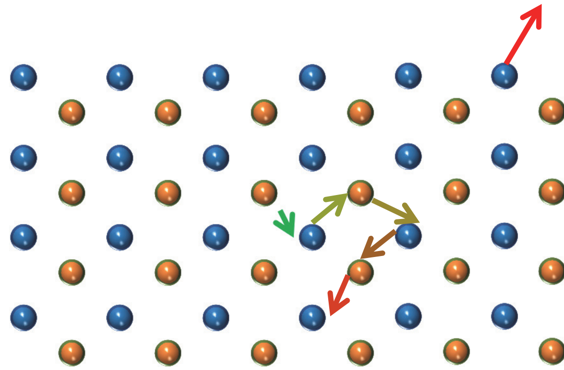

Figure 5.12: Energetic electrons go through inelastic collisions with the lattice atoms. The outgoing nuclei collide with other atoms inelastically. The displacement chain stops when the last nucleus' energy is smaller than the threshold atomic displacement energy of other atoms.

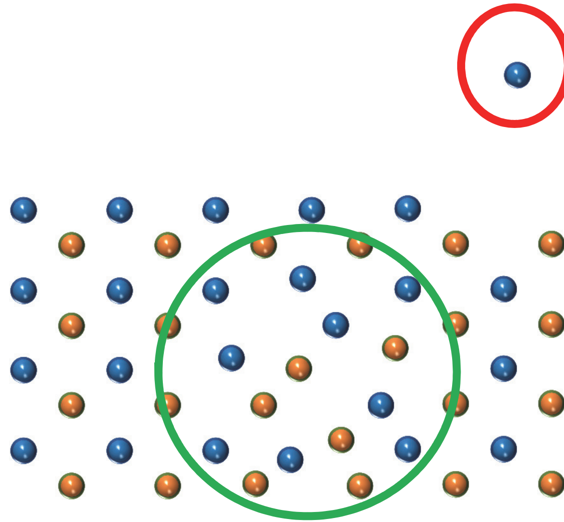

Figure 5.13: Stable distortions (inside the green circle) require higher number of displacements ($n \geq 5$). If the atom being displaced is a surface atom, it might leave the lattice (the atom inside the red circle).

PL spectroscopy was conducted on both wafers before and after irradiation (Figure 5.14). Peculiarly, the spectra from the wafers show different behaviors and yet, they confirm and clarify

the performance degradation in one wafer against the enhancement of the other. In Figure 5.14 (a), the 4L sample indicates a shift from the green luminescence to a very broad blue-violet luminescence, followed by a peak in the UV range. The reduction of the layer thickness of the 4L sample after 2.2 MGy irradiation is further confirmed by the decline in the UV luminescence amplitude. Although the area ratio of the UV luminescence over the visible luminescence is an indication of an improved crystal quality[79], the excitonic emissions close to 3~3.2 eV have been attributed to different transitions. Noting the existing controversy over different aspects of point defects in ZnO, such as the origin of the green luminescence and the n-type/p-type conductivities, the UV-violet-blue luminescence can be attributed to several energy states. Zinc interstitial (Zn_i)[80] state transitions to valence band minimum (VMB), conduction band maximum (CMB) transitions to deep acceptor levels such as zinc vacancies (V_{zn})[81] and to negatively charged zinc vacancies (V_{Zn}^-)[82] have been attributed to blue-violet luminescence. UV luminescence can be attributed to V_{Zn}^- weekly perturbed by neighborhood zinc atoms (*i.e.* V'^-_{Zn})[83], as well as deep acceptor-bound exciton level transitions caused by nitrogen replacing oxygen sites (N_O).[84,85] Fu *et al.* reported an intensification of the UV photoluminescence (PL) emission of ZnO-SiO_2 nanocomposites grown *via* sol gel process compared to ZnO. They deduced the formation of Zn–O–Si bonds at the ZnO-SiO_2 interface.[86]

The PL for 8L sample (Figure 5.14 (b)) indicates a slight shift from the green luminescence toward blue luminescence after 1.2 MGy and a very broad blue/violet/UV luminescence after 2.2 MGy, suggesting the creation of V_{zn} and V_{zn} complexes as well as Zn_i. The nanocrystalline ZnO films contain a significant number of point defects, mainly at the grain boundaries. The cascade caused by ionization damage of gamma irradiation can create and alter the charge of the defects which might have been unstable during the growth process due to high formation energies or very

small migration energies such as Zn_i.[87] A similarity can be noticed between the photoluminescence transitions of Un-4L to 120-Irr-4L, and of 120-Irr-8L to 220-Irr-8L; and that is the decline in green luminescence (mainly attributed to positively charged V_O)[88] and an enhancement of broad blue/violet/UV luminescence (V_{zn} and Zn_i related defects, as well as the creation of Zn–O–Si bonds possibly due to displaced silicon atoms).

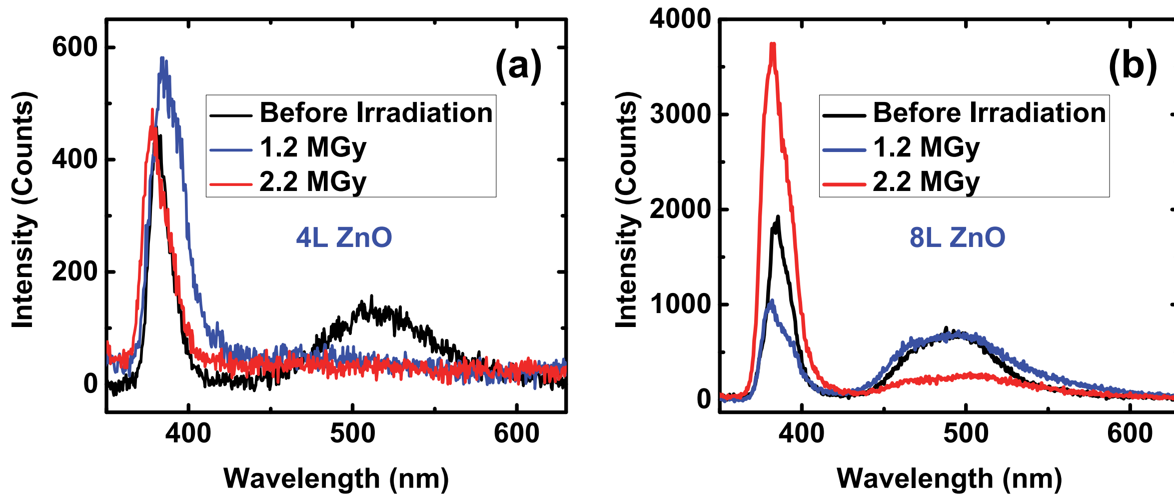

Figure 5.14: PL spectra of the sample from the 4L wafer (a) and the 8L wafer (b) before and after irradiation.

The gate leakage current (I_G) measured for all devices (from 4L and 8L wafers) remained in the 1 ~ 50 pA range before and after 1.2 MGy irradiation dose, indicating the damage effect on I_G to be negligible. After the additional 1 MGy, however, the leakage current in 8L-1 sample was magnified by an order of magnitude (Figure 5.15).

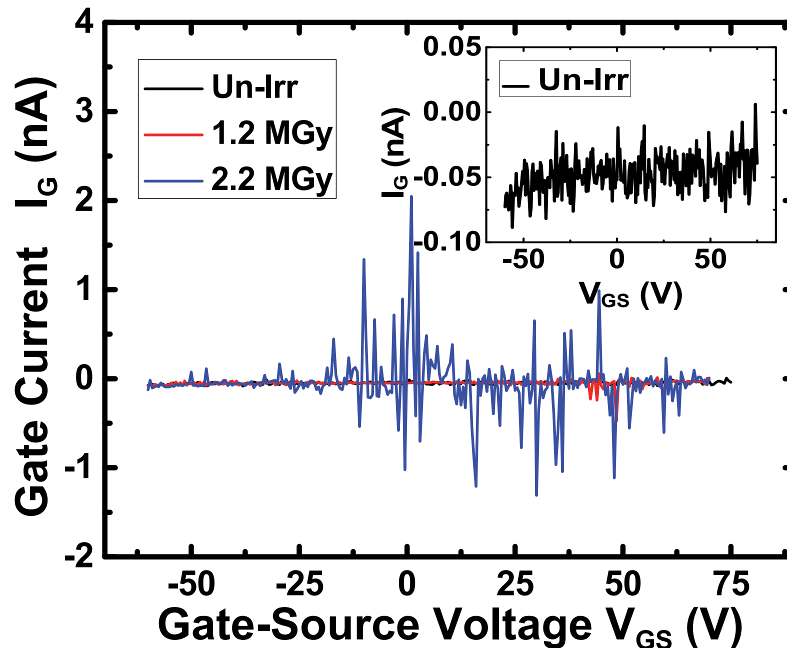

Figure 5.15: Gate current as a function of gate-source voltage after different irradiation doses for 8L-1 (*i.e.* Un-8L-1, 120-8L-1 and 220-8L-1). The inset indicates the magnified leakage current for the unirradiated sample.

Finally, the devices were re-measured after 18 months to examine the improvement and the self-healing of the ZnO devices at room temperature. No recovery was observed in room temperature, proposing the formation of stable point defect clusters[89] and permanent damage due to the etching of the surface due to ballistic ejection of the surface atoms.

5.4 Conclusion

Thin film transistors were fabricated *via* the sol-gel spin-coating technique and were measured before and after gamma irradiation doses of 1.2 MGy and 2.2 MGy. The output measurements confirmed the stability of the devices. Slight saturation mobility degradation (enhancement) was observed in the 4-layer (8 layer) ZnO devices after 1.2 MGy irradiation.

Further radiation dose of 1 MGy degraded the mobility and I_{ON}/I_{OFF} of the 8-layer device and the 4-layer devices became dysfunctional. Measurements indicated a negative shift of threshold voltages in all devices after 1.2 MGy irradiation. An abnormality in the subthreshold regime was observed which was removed after irradiation. AFM indicated a reduction of ZnO layer thickness. A model was proposed based on the displacement damage occurred to the surface atoms. Photoluminescence indicated a broad blue/violet/UV shift of the visible spectrum. The enhancements and degradations of devices were in agreement with PL spectra.

References

[1] Harris, Gary Lynn, ed. Properties of silicon carbide. No. 13. Iet, 1995. p.31.

[2] Gil, Bernard, ed. III-nitride semiconductors and their modern devices. Vol. 18. OUP Oxford, 2013.

[3] Huang, M.H., Mao, S., Feick, H., Yan, H., Wu, Y., Kind, H., Weber, E., Russo, R. and Yang, P., 2001. Room-temperature ultraviolet nanowire nanolasers. science, 292(5523), pp.1897-1899.

[4] Gupta, T.K., 1990. Application of zinc oxide varistors. Journal of the American Ceramic Society, 73(7), pp.1817-1840.

[5] Masuda, S., Kitamura, K., Okumura, Y., Miyatake, S., Tabata, H. and Kawai, T., 2003. Transparent thin film transistors using ZnO as an active channel layer and their electrical properties. Journal of Applied Physics, 93(3), pp.1624-1630.

[6] Dilonardo, E., Alvisi, M., Cassano, G. and Penza, M., 2017. Enhanced gas sensing properties of chemiresistors based on ZnO nanorods electrodecorated with Au and Pd nanoparticles. MRS Advances, 2(18), pp.1001-1007.

[7] Baruah, S., Maibam, B. and Kumar, S., 2017. Zinc Oxide: A Novel Material for Biosensors (A review). Imperial Journal of Interdisciplinary Research, 3(3)

[8] Ibupoto, Z.H., Khun, K. and Willander, M., 2013. A selective iodide ion sensor electrode based on functionalized ZnO nanotubes. Sensors, 13(2), pp.1984-1997.

[9] Zhu, Y., Liu, S., Apostoluk, A., Masenelli, B. and Daniele, S., 2013. ZnO nanoparticles as a luminescent down-shifting layer for photosensitive devices. Journal of Semiconductors, 34(5).

[10] Wang, Z.L., 2007. Nanopiezotronics. Advanced Materials, 19(6), pp.889-892.

[11] Wang, Z.L. and Song, J., 2006. Piezoelectric nanogenerators based on zinc oxide nanowire arrays. Science, 312(5771), pp.242-246.

[12] Lin, Y.J., Su, Y.C. , 2012. Modification of the electrical properties of poly (3, 4-ethylenedioxythiophene) doped with poly (4-styrenesulfonate) upon doping of ZnO nanoparticles of different content. Journal of Applied Physics, 111(7), p.073712.

[13] Mirkhani, V., Tong, F., Song, D., Chung, Y., Ozden, B., Yapabandara, K., Hamilton, M., Kim, D.J., Koo, H., Lee, K.K. and Park, M., 2016. Simulation of the Refractive Index of Ga Doped ZnO Nanoparticles Embedded in PEDOT: PSS Using Effective Medium Approximations. Journal of Nanoscience and Nanotechnology, 16(7), pp.7358-7362.

[14] Wong, M., Guenther, J., Sun, L., Blümel, J., Nishimura, R. and Sue, H.J., 2012. Synthesis and fabrication of multifunctional nanocomposites: stable dispersions of nanoparticles tethered with short, dense and polydisperse polymer brushes in poly (methyl methacrylate). Advanced Functional Materials, 22(17), pp.3614-3624.

[15] Abubakar, S., Kaya, S., Karacali, H. and Yilmaz, E., 2017. The gamma irradiation responses of yttrium oxide capacitors and first assessment usage in radiation sensors. Sensors and Actuators A: Physical, 258, pp.44-48.

[16] Novak, S., Singh, V., Monmeyran, C., Ingram, A., Han, Z., Lin, H., Borodinov, N., Patel, N., Du, Q., Hu, J. and Luzinov, I., 2017. Positron annihilation lifetime spectroscopy (PALS) studies of gamma irradiated As 2 Se 3 films used in MIR integrated photonics. Journal of Non-Crystalline Solids, 455, pp.29-34.

[17] Ozden, B., Khanal, M.P., Park, J., Uprety, S., Mirkhani, V., Yapabandara, K., Kim, K., Kuroda, M., Bozack, M.J., Choi, W. and Park, M., 2017. Raman and X-ray photoelectron spectroscopy investigation of the effect of gamma-ray irradiation on MoS2. Micro & Nano Letters, 12(4), pp.271-274.

[18] Khanal, M.P., Ozden, B., Kim, K., Uprety, S., Mirkhani, V., Yapabandara, K., Ahyi, A.C. and Park, M., 2017. Electrical and optical characteristics of gamma-ray irradiated AlGaN/GaN high electron mobility transistors. Journal of Vacuum Science & Technology B, Nanotechnology and Microelectronics: Materials, Processing, Measurement, and Phenomena, 35(3), p.03D107.

[19] Deshpande, V.K. and Raut, A.P., 2017. Effect of gamma irradiation on the density, glass transition temperature and electrical conductivity of lithium borosilicate glasses with alumina addition. Journal of Non-Crystalline Solids, 457, pp.104-110.

[20] Sayyed, M.I., Elmahroug, Y., Elbashir, B.O. and Issa, S.A., 2017. Gamma-ray shielding properties of zinc oxide soda lime silica glasses. Journal of Materials Science: Materials in Electronics, 28(5), pp.4064-4074.

[21] Lee, E.H., Indluru, A., Allee, D.R., Clark, L.T., Holbert, K.E. and Alford, T.L., 2011. Effects of gamma irradiation and electrical stress on a-Si: H thin-film transistors for flexible electronics and displays. Journal of Display Technology, 7(6), pp.325-329.

[22] Hastas, N.A., Dimitriadis, C.A., Brini, J., Kamarinos, G., Gueorguiev, V.K. and Kaschieva, S., 2003. Effects of gamma-ray irradiation on polycrystalline silicon thin-film transistors. Microelectronics Reliability, 43(1), pp.57-60.

[23] Benedetto, J.M., Bishop, A., Martin, M. and Haddad, N., 1998, July. High total dose response of the UTMC gate array fabricated at Lockheed Martin Federal Systems. In Radiation Effects Data Workshop, 1998. IEEE (pp. 86-90). IEEE.

[24] Anelli, G., Campbell, M., Delmastro, M., Faccio, F., Floria, S., Giraldo, A., Heijne, E., Jarron, P., Kloukinas, K., Marchioro, A. and Moreira, P., 1999. Radiation tolerant VLSI circuits in standard deep submicron CMOS technologies for the LHC experiments: practical design aspects. IEEE Transactions on Nuclear Science, 46(6), pp.1690-1696.

[25] Hughes, H.L. and Benedetto, J.M., 2003. Radiation effects and hardening of MOS technology: devices and circuits. IEEE Transactions on Nuclear Science, 50(3), pp.500-521.

[26] Auret, F.D., Goodman, S.A., Hayes, M., Legodi, M.J., Van Laarhoven, H.A. and Look, D.C., 2001. The influence of high energy proton bombardment on the electrical and defect properties of single-crystal ZnO. Journal of Physics: Condensed Matter, 13(40), p.8989.

[27] Knutsen, K.E., Galeckas, A., Zubiaga, A., Tuomisto, F., Farlow, G.C., Svensson, B.G. and Kuznetsov, A.Y., 2012. Zinc vacancy and oxygen interstitial in ZnO revealed by sequential annealing and electron irradiation. Physical Review B, 86(12), p.121203.

[28] Look, D.C., Reynolds, D.C., Hemsky, J.W., Jones, R.L. and Sizelove, J.R., 1999. Production and annealing of electron irradiation damage in ZnO. Applied Physics Letters, 75(6), pp.811-813.

[29] Smith, J.M. and Vehse, W.E., 1970. ESR of electron irradiated ZnO confirmation of the F+ center. Physics Letters A, 31(3), pp.147-148.

[30] Coskun, C., Look, D.C., Farlow, G.C. and Sizelove, J.R., 2004. Radiation hardness of ZnO at low temperatures. Semiconductor science and technology, 19(6), p.752.

[31] Vlasenko, L.S. and Watkins, G.D., 2005. Optical detection of electron paramagnetic resonance for intrinsic defects produced in ZnO by 2.5-MeV electron irradiation in situ at 4.2 K. Physical Review B, 72(3), p.035203.

[32] Khanna, R., Ip, K., Allums, K.K., Baik, K., Abernathy, C.R., Pearton, S.J., Heo, Y.W., Norton, D.P., Ren, F., Dwivedi, R. and Fogarty, T.N., 2004. Effects of high dose proton irradiation on the electrical performance of ZnO Schottky diodes. physica status solidi (a), 201(12), pp.R79-R82.

[33] Hong, W.K., Jo, G., Sohn, J.I., Park, W., Choe, M., Wang, G., Kahng, Y.H., Welland, M.E. and Lee, T., 2010. Tuning of the electronic characteristics of ZnO nanowire field effect transistors by proton irradiation. Acs Nano, 4(2), pp.811-818.

[34] Flitsiyan, E.S., Swartz, C.M., Peale, R.E., Lupan, O., Chernyak, L., Chow, L., Vernetson, W.G. and Dashevsky, Z., 2008. Neutron transmutation doping and radiation hardness for solution-grown bulk and nano-structured ZnO. In MRS Proceedings (Vol. 1108, pp. 1108-A05). Cambridge University Press.

[35] Taylor, A.L., Filipovich, G. and Lindeberg, G.K., 1970. Electron paramagnetic resonance associated with Zn vacancies in neutron-irradiated ZnO. Solid State Communications, 8(17), pp.1359-1361.

[36] Liao, L., Lu, H.B., Li, J.C., Liu, C., Fu, D.J. and Liu, Y.L., 2007. The sensitivity of gas sensor based on single ZnO nanowire modulated by helium ion radiation. Applied Physics Letters, 91(17), p.173110.

[37] Wendler, E., Bilani, O., Gärtner, K., Wesch, W., Hayes, M., Auret, F.D., Lorenz, K. and Alves, E., 2009. Radiation damage in ZnO ion implanted at 15K. Nuclear Instruments and Methods in Physics Research Section B: Beam Interactions with Materials and Atoms, 267(16), pp.2708-2711.

[38] Azarov, A.Y., Kucheyev, S.O., Titov, A.I. and Karaseov, P.A., 2007. Effect of the density of collision cascades on ion implantation damage in ZnO. Journal of Applied Physics, 102(8), p.083547.

[39] Tuomisto, F., Saarinen, K., Look, D.C. and Farlow, G.C., 2005. Introduction and recovery of point defects in electron-irradiated ZnO. Physical Review B, 72(8), p.085206.

[40] Locker, D.R. and Meese, J.M., 1972. Displacement thresholds in ZnO. IEEE Transactions on Nuclear Science, 19(6), pp.237-242.

[41] Lorenz, K., Alves, E., Wendler, E., Bilani, O., Wesch, W. and Hayes, M., 2005. Damage formation and annealing at low temperatures in ion implanted ZnO. Applied Physics Letters, 87(19), p.191904.

[42] Johnston, A., 2010. Reliability and radiation effects in compound semiconductors. World Scientific. p.241

[43] Jackson, T., 2017. Radiation Hard and Self Healing Substrate Agnostic Nanocrystalline ZnO Thin Film Electronics. PENNSYLVANIA STATE UNIV STATE COLLEGE UNIVERSITY PARK United States.

[44] Zhao, D., Mourey, D.A. and Jackson, T.N., 2010, June. Gamma-ray irradiation of ZnO thin film transistors and circuits. In Device Research Conference (DRC), 2010 (pp. 241-242). IEEE.

[45] Ramirez, J.I., Li, Y.V., Basantani, H. and Jackson, T.N., 2013, June. Effects of gamma-ray irradiation and electrical stress on ZnO thin film transistors. In Device Research Conference (DRC), 2013 71st Annual (pp. 171-172). IEEE.

[46] Ramirez, J.I., Li, Y.V., Basantani, H., Leedy, K., Bayraktaroglu, B., Jessen, G.H. and Jackson, T.N., 2015. Radiation-Hard ZnO Thin Film Transistors. IEEE Transactions on Nuclear Science, 62(3), pp.1399-1404.

[47] Laurenti, M., Porro, S., Pirri, C.F., Ricciardi, C. and Chiolerio, A., 2017. Zinc oxide thin films for memristive devices: a review. Critical Reviews in Solid State and Materials Sciences, 42(2), pp.153-172.

[48] K. Nishio, S. Miyake, T. Sei, Y. Watanabe and T. Tsuchiya, Journal of materials science 31, 14 (1996)

[49] Y. Natsume and H. Sakata, Thin Solid Films 372, 1 (2000)

[50] B. J. Norris, J. Anderson, J. F. Wager and D. A. Keszler, J. Phys. D: Appl. Phys. 36, 20 (2003)

[51] Wang, S., Mirkhani, V., Yapabandara, K., Ko, S., Sk, M.H., Park, M. and Hamilton, M.C., 2015, June. Analysis of the effect of gamma-ray irradiation and low-temperature characteristics of sol-gel derived ZnO thin-film transistors. In Device Research Conference (DRC), 2015 73rd Annual (pp. 171-172). IEEE.

[52] Neely, H.H. and Bauer, W., 1966. Electron-irradiation damage-rate measurements in aluminum. Physical Review, 149(2), p.535.

[53] Jimenez, C.M., Lowe, L.F., Burke, E.A. and Sherman, C.H., 1967. Radiation Damage in Pd Produced by 1-3-MeV Electrons. Physical Review, 153(3), p.735.

[54] Jagadish, Chennupati, and Stephen J. Pearton, eds. Zinc oxide bulk, thin films and nanostructures: processing, properties, and applications. Elsevier, 2011, p. 428.

[55] Giraldo, A., Paccagnella, A. and Minzoni, A., 2000. Aspect ratio calculation in n-channel MOSFETs with a gate-enclosed layout. Solid-State Electronics, 44(6), pp.981-989.

[56] Hoffman, R.L., 2004. ZnO-channel thin-film transistors: Channel mobility. Journal of Applied Physics, 95(10), pp.5813-5819.

[57] This abnormality exists in transconductance and mobility measurements of all devices fabricated by our sol gel spin coating method and is currently under investigation. The justified results will be published elsewhere.

[58] Cordaro, J.F., Shim, Y. and May, J.E., 1986. Bulk electron traps in zinc oxide varistors. Journal of applied physics, 60(12), pp.4186-4190.

[59] Liao, Z.M., Zhang, H.Z., Zhou, Y.B., Xu, J., Zhang, J.M. and Yu, D.P., 2008. Surface effects on photoluminescence of single ZnO nanowires. Physics Letters A, 372(24), pp.4505-4509.

[60] Yapabandara, K., Mirkhani, V., Sultan, M.S., Ozden, B., Khanal, M.P., Park, M., Wang, S., Hamilton, M.C., Chung, Y., Kim, D.J. and Sk, M.H., 2017. Study of device instability of bottom-gate ZnO transistors with sol–gel derived channel layers. Journal of Vacuum Science & Technology B, Nanotechnology and Microelectronics: Materials, Processing, Measurement, and Phenomena, 35(3), p.03D104.

[61] Ghaffarzadeh, K., Nathan, A., Robertson, J., Kim, S., Jeon, S., Kim, C., Chung, U.I. and Lee, J.H., 2010. Instability in threshold voltage and subthreshold behavior in Hf–In–Zn–O thin film transistors induced by bias-and light-stress. Applied Physics Letters, 97(11), p.113504.

[62] Jagadish, Chennupati, and Stephen J. Pearton, eds. Zinc oxide bulk, thin films and nanostructures: processing, properties, and applications. Elsevier, 2011, p. 437.

[63] Abu-Jarad, F., Hala, A.M., Farhat, M. and Islam, M., 1997. Effect of high gamma dose on the PADC properties. Radiation measurements, 28(1), pp.111-114.

[64] Gorna, K. and Gogolewski, S., 2003. The effect of gamma radiation on molecular stability and mechanical properties of biodegradable polyurethanes for medical applications. Polymer degradation and stability, 79(3), pp.465-474.

[65] Montanari, L., Cilurzo, F., Selmin, F., Conti, B., Genta, I., Poletti, G., Orsini, F. and Valvo, L., 2003. Poly (lactide-co-glycolide) microspheres containing bupivacaine: comparison between gamma and beta irradiation effects. Journal of controlled release, 90(3), pp.281-290.

[66] Sukkar, M.H., Johnson, K.H. and Tuller, H.L., 1990. Defects and electronic structure of interfaces in ZnO: Cluster molecular orbital calculations. Materials Science and Engineering: B, 6(1), pp.49-59.

[67] Liao, L., Lu, H.B., Li, J.C., Liu, C., Fu, D.J. and Liu, Y.L., 2007. The sensitivity of gas sensor based on single ZnO nanowire modulated by helium ion radiation. Applied Physics Letters, 91(17), p.173110.

[68] Chang, C., Hu, C. and Brodersen, R.W., 1985. Quantum yield of electron impact ionization in silicon. Journal of Applied Physics, 57(2), pp.302-309.

[69] Liu, L., Mei, Z., Tang, A., Azarov, A., Kuznetsov, A., Xue, Q.K. and Du, X., 2016. Oxygen vacancies: The origin of n-type conductivity in ZnO. Physical Review B, 93(23), p.235305.

[70] Look, D.C., Farlow, G.C., Reunchan, P., Limpijumnong, S., Zhang, S.B. and Nordlund, K., 2005. Evidence for native-defect donors in n-type ZnO. Physical review letters, 95(22), p.225502.

[71] Van de Walle, C.G., 2000. Hydrogen as a cause of doping in zinc oxide. Physical review letters, 85(5), p.1012.

[72] Selim, F.A., Weber, M.H., Solodovnikov, D. and Lynn, K.G., 2007. Nature of native defects in ZnO. Physical review letters, 99(8), p.085502.

[73] McCluskey, M.D. and Jokela, S.J., 2007. Sources of n-type conductivity in ZnO. Physica B: Condensed Matter, 401, pp.355-357.

[74] Mourey, D.A., Burberry, M.S., Zhao, D.A., Li, Y.V., Nelson, S.F., Tutt, L., Pawlik, T.D., Levy, D.H. and Jackson, T.N., 2010. Passivation of ZnO TFTs. Journal of the Society for Information Display, 18(10), pp.753-761.

[75] Vehse, W.E., Sibley, W.A., Keller, F.J. and Chen, Y., 1968. Radiation damage in ZnO single crystals. Physical Review, 167(3), p.828.

[76] Indluru, A., Holbert, K.E. and Alford, T.L., 2013. Gamma radiation effects on indium-zinc oxide thin-film transistors. Thin Solid Films, 539, pp.342-344.

[77] Alford, T.L., Indluru, A., Vemuri, R.N. and Holbert, K.E., 2013. The Stability and Reliability of Mixed Oxide-Based Thin Film Transistors under Gamma Irradiation. ECS Transactions, 50(8), pp.191-196.

[78] Craciun, D., Socol, G., Le Caër, S., Trinca, L.M., Galca, A.C., Pantelica, D., Ionescu, P. and Craciun, V., 2016. Gamma irradiation effects on the properties of indium zinc oxide thin films. Thin Solid Films, 614, pp.2-6.

[79] Fu, Z., Lin, B., Liao, G. and Wu, Z., 1998. The effect of Zn buffer layer on growth and luminescence of ZnO films deposited on Si substrates. Journal of crystal growth, 193(3), pp.316-321.

[80] Ahn, C.H., Kim, Y.Y., Kim, D.C., Mohanta, S.K. and Cho, H.K., 2009. A comparative analysis of deep level emission in ZnO layers deposited by various methods. Journal of Applied Physics, 105(1), p.013502.

[81] Fang, Z., Wang, Y., Xu, D., Tan, Y. and Liu, X., 2004. Blue luminescent center in ZnO films deposited on silicon substrates. Optical Materials, 26(3), pp.239-242.

[82] Wu, X.L., Siu, G.G., Fu, C.L. and Ong, H.C., 2001. Photoluminescence and cathodoluminescence studies of stoichiometric and oxygen-deficient ZnO films. Applied Physics Letters, 78(16), pp.2285-2287.

[83] Wang, X.D., He, S.Y., Yang, D.Z. and Gu, P.F., 2011. Space Radiation Damage in ZnO Induced by Subthreshold Electrons: Defect Identity and Optical Degradation. Radiation research, 176(2), pp.264-268.

[84] Look, D.C., Reynolds, D.C., Litton, C.W., Jones, R.L., Eason, D.B. and Cantwell, G., 2002. Characterization of homoepitaxial p-type ZnO grown by molecular beam epitaxy. Applied physics letters, 81(10), pp.1830-1832.

[85] Rommeluere, J.F., Svob, L., Jomard, F., Mimila-Arroyo, J., Lusson, A., Sallet, V. and Marfaing, Y., 2003. Electrical activity of nitrogen acceptors in ZnO films grown by metalorganic vapor phase epitaxy. Applied physics letters, 83(2), pp.287-289.

[86] Fu, Z., Yang, B., Li, L., Dong, W., Jia, C. and Wu, W., 2003. An intense ultraviolet photoluminescence in sol–gel ZnO–SiO2 nanocomposites. Journal of Physics: Condensed Matter, 15(17), p.2867.

[87] Janotti, A. and Van de Walle, C.G., 2007. Native point defects in ZnO. Physical Review B, 76(16), p.165202.

[88] Vanheusden, K., Seager, C.H., Warren, W.T., Tallant, D.R. and Voigt, J.A., 1996. Correlation between photoluminescence and oxygen vacancies in ZnO phosphors. Applied physics letters, 68(3), pp.403-40.

[89] Lorenz, K., Alves, E., Wendler, E., Bilani, O., Wesch, W. and Hayes, M., 2005. Damage formation and annealing at low temperatures in ion implanted ZnO. Applied Physics Letters, 87(19), p.191904.

Chapter 6

ZnO Nanoparticle Inclusions as Refractive Index Modifiers

6.1 Introduction

The following work has been published in the Journal of Nanoscience and Nanotechnology as "Simulation of the Refractive Index of Ga Doped ZnO Nanoparticles Embedded in PEDOT: PSS Using Effective Medium Approximations". The author wants to primarily acknowledge the help of Fei Tong for her great contribution. This study was also facilitated by Dewang Song, Yoonsung Chung, Burcu Ozden, Kosala Yapabandara, Michael C. Hamilton, Dong-Joo Kim, Helen Koo, Kyeong K. Lee, and Minseo Park.[1] We have theoretically investigated the change of refractive index of nanocomposites composed of Ga-doped ZnO nanoparticles (Ga-ZnO NPs) dispersed in conductive polymer Poly(3,4-ethylenedioxythiophene) and Poly(styrene sulfonic acid) (PEDOT:PSS) matrix by tuning the fraction of the Ga-ZnO NP inclusions and concentration of Ga dopant in Ga-ZnO, by using Maxwell-Garnet, Bruggeman and Lorentz-Lorenz effective medium theories. The dependence of the effective refractive index of Ga-ZnO NPs embedded in PEDOT:PSS composite on the Ga doping concentration and its volume fraction of the inclusions are presented. Ga-ZnO NPs can increase the effective refractive index. This can be used to engineer a desired effective index of refraction for the enhancement of light extraction and absorption efficiency in optical devices such as organic light emitting diodes (OLEDs) and organic solar cells

(OSCs). It is crucial to match the refractive indices of conductive anode electrode and the emissive layer.

Nanoparticles dispersed in a polymer or polymer-nanoparticle composites have recently attracted great attention in the potential optoelectronic applications in band gap alteration for organic solar cells (OSCs)[2,3] and enhancing electroluminescence (EL) properties in organic light emitting diodes (OLEDs).[4,5] Electrical and optical properties of the composite can be tuned by using nano-inclusions. Several researchers have reported modification of the refractive index of the polymer-nanoparticle composites by adjusting the size and concentration of NPs. Obreja *et al.*[6] reported the increase of the refractive index of poly(methyl methacrylate) (PMMA), 2-hydroxyethyl methacrylate (HEMA) and polyvinyl alcohol (PVA) by doping them with oxide NPs such as TiO_2, ZrO_2, SiO_2. Modification of the refractive index of the nanocomposites based on poly(methyl methacrylate) (PMMA) and zinc oxide (ZnO) NPs was reported by Demir *et al.*[7] In addition, Englebienne *et al.*[8] reported an increase in refractive index of composite composed of encapsulated colloidal gold NPs and water-soluble conductive polymer poly(aniline-2-carboxylic acid) (PANI-COOH).

Poly(3,4-ethylenedioxythiophene)-poly(styrene sulfonic acid) (PEDOT:PSS) remains to be a popular conductive organic polymer which is widely used as the anode electrode (hole transport layer) in flexible organic optoelectronic devices such as OLEDs[9,10] and OSCs.[11,12] In the case of OLEDs, it is desired to adjust the refractive index of PEDOT:PSS ($n = 1.42$)[13] to match that of the organic polymer emissive layer whose refractive index is usually in the range of 1.7~1.8.[14] Due to the inherent high refractive index of ZnO ($n=2.0$)[15], embedding ZnO NPs in PEDOT:PSS will increase the refractive index of the polymer-composite matrix, improving the

light extraction efficiency of the OLED. For solar cells, impedance matching of the photoactive layer with the transparent conductive layer can increase the efficiency.[16,17]

Although the modification of the electrical conductivity of PEDOT:PSS by the incorporation of ZnO NPs has been investigated by a few research groups[18,19], the theoretical study of the modification of the refractive index of such nanocomposites have not been conducted. Among the group III dopants applied to alleviate the resistivity of ZnO, Ga is one of the most efficient elements, has the closest electronegativity and the atomic radius to zinc[20], and increases the mobility in ZnO.[21] Therefore, the focus of this work will be on the investigation of the modification of the refractive index of Ga doped ZnO (Ga-ZnO) NPs embedded in PEDOT:PSS (hereafter to be referred to as Ga-ZnO/PEDOT:PSS) by simulation based on Bruggeman (BG), Maxwell-Garnett (MG) and Lorentz-Lorenz (LL) effective medium approximations.[22] These theories were frequently applied for modeling of optical properties of nanocomposites.[23,24,25] Wong *et al.*[26] and Janicki *et al.*[27] used Maxwell-Garnet's, Bruggeman's, Lorentz-Lorenz's and other effective medium theories to model the refractive index profiles of ZnO quantum dots dispersed in Poly(methyl methacrylate), and of the dielectric inhomogeneous coatings, respectively.

6.2 Simulation Details

Among many effective medium approximations (EMA), BG's, MG's and LL's theories were used since Ga-ZnO NPs inside PEDOT:PSS form a two-phase nanocomposite.[28] In BG's approach, the ratio of both constituents' volumes in the homogenous blend are comparable (between 1/3 and 2/3).[29] Thus, the effective dielectric constant and the refractive index are equally affected by the two media in BG's method. In MG's approximation, a smaller constituent is

dispersed in a main medium, negligibly affecting the dominant electric field inside. In the cases where the inclusions' fraction approaches zero, and/or the constituents' refractive index approaches the refractive index of the host, the two theories (BG and MG) become equivalent.[30] In both cases, the wavelength of the incoming radiations must be much larger than the size of the inclusions since these approximations are based on considering particles in a uniform electric field. In LL's approximation, the effects of the neighboring dipoles are also taken into account.[31] Spherical inclusions are considered being affected by the outer electric field as well as the dipole field from the neighboring polarized inclusions. It should be noted that the geometrical shapes of the inclusions are considered to be spherical for all the effective medium theories mentioned above. Depending on the structure of the mixture and the comparative filling factors, one approach is more accurate than others.

By using the effective medium approximations, the resultant effective refractive indices n_{eff} of the Ga-ZnO/PEDOT:PSS were calculated. n_H (higher index) and n_L (lower index) are denoted for the refractive indices of Ga-ZnO and PEDOT:PSS, respectively. In general, $n^2 = \varepsilon\mu$, where ε is the relative permittivity and μ is the relative permeability. Since the inclusions and the matrix are both non-magnetic in this study, it was assumed that $\mu \rightarrow 1$. The volume fraction of the inclusions (Ga-ZnO) is denoted by f_H, and the volume fraction of PEDOT:PSS is denoted by $f_L = 1 - f_H$. The effective refractive indices of the mixtures were calculated using the following equations for (1) BG[32], (2) MG[33] and (3) LL[23] effective medium approximations, respectively:

$$\text{BG} \quad f_H \frac{n_H^2 - n_{eff}^2}{n_H^2 + 2n_{eff}^2} + (1 - f_H)\frac{n_L^2 - n_{eff}^2}{n_L^2 + 2n_{eff}^2} = 0 \tag{1}$$

$$\text{MG} \quad \frac{n_{eff}^2 - n_H^2}{n_{eff}^2 + 2n_H^2} = (1 - f_H)\frac{n_L^2 - n_H^2}{n_L^2 + 2n_H^2} \tag{2}$$

$$\text{LL} \quad \frac{n_{eff}^2 - 1}{n_{eff}^2 + 2} = f_H \frac{n_H^2 - 1}{n_H^2 + 2} + (1 - f_H)\frac{n_L^2 - 1}{n_L^2 + 2} \tag{3}$$

6.3 Results and Discussion

Figure 6.1 shows the schematics of the embedded Ga doped ZnO nanoparticles in PEDOT:PSS polymer matrix. The refractive index of PEDOT:PSS (n_L = 1.42) can be increased by embedding ZnO NPs (n=2.0) in the polymer matrix to match that of the organic polymer emissive (active) layer (n=1.7~1.8) in order to increase the light extraction efficiency. In addition, Ga doping of the ZnO NPs can be applied for fine tuning of the refractive index of the layer.

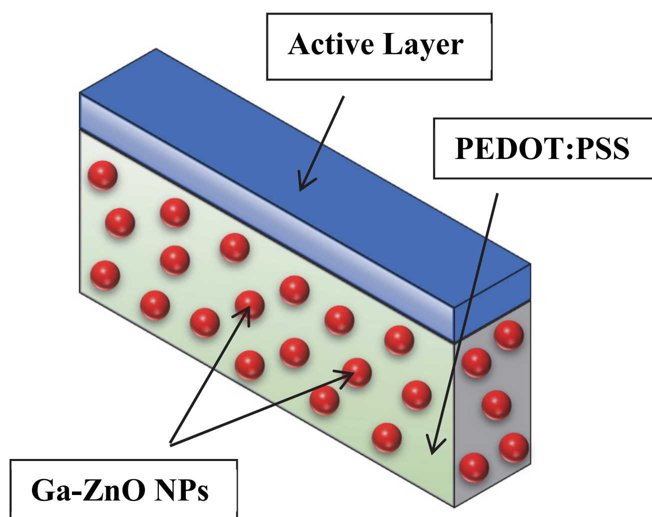

Figure 6.1: Schematics of the embedded Ga doped ZnO nanoparticles in PEDOT:PSS polymer matrix.

The refractive index is wavelength dependent, thus the calculations were performed for three different wavelengths. The maximum index of refraction for pure ZnO occurs at λ= 403 nm according to the experimental data we collected from an article by D.-T. Phan *et al.*[34,35] We have also calculated the effective refractive indices for λ= 550 nm since tris-8-hydroxyquinoline aluminum (Alq3) [36] is widely used in green OLEDs for its high electron mobility and efficiency. In addition, λ= 650 nm was also used for the red OLEDs.[37] Table 6.1 summarizes effective

refractive indices of Ga-ZnO NPs (n_H) with different Ga doping percentages, for each aforementioned wavelength.

Figures 6.2, 6.3, and 6.4 show the effective refractive index of Ga-ZnO/PEDOT:PSS for λ= 403 nm simulated by BG, MG and LL effective medium approximations, respectively. Figures 6.5, 6.6, and 6.7 indicate the simulated effective refractive index of the composite determined at λ = 550 by the BG, MG, and LL theories, respectively. Figures 6.8, 6.9, and 6.10 show the effective refractive index simulated at λ = 650 nm by the BG, MG, and LL equations, respectively. The effective refractive index of Ga-ZnO/PEDOT:PSS was affected by the doping concentration of Ga, the fraction of inclusion, and the wavelength of the light.

Since the maximum refractive index for pure ZnO occurs at λ=403nm, the Ga dopants' contribution to the effective refractive index at this wavelength is more apparent, as is shown in Figures 6.2, 6.3, and 6.4. As for higher wavelengths, the contribution of the dopant becomes less evident.

Table 6.1: Refractive Index of Ga-ZnO [Ref. 34, 35]

Ga weight % →	0 weight %	1 weight %	2 weight %	3 weight %	4 weight %
403nm	2.03524	1.97737	1.96884	1.97202	1.97002
550nm	1.97614	1.96506	1.96591	1.96673	1.97052
650nm	1.96638	1.96272	1.96198	1.96403	1.96572

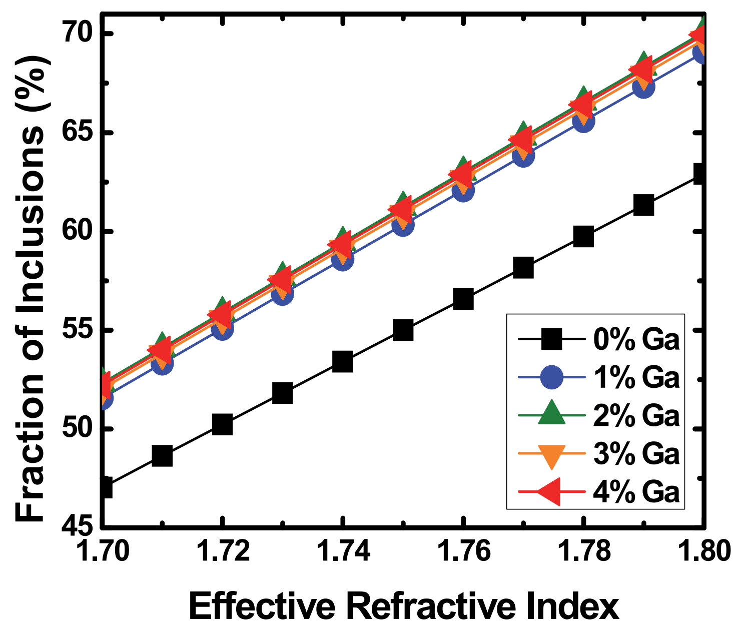

Figure 6.2: Effective Refractive Index of Ga-ZnO/PEDOT:PSS determined by BG at 403nm.

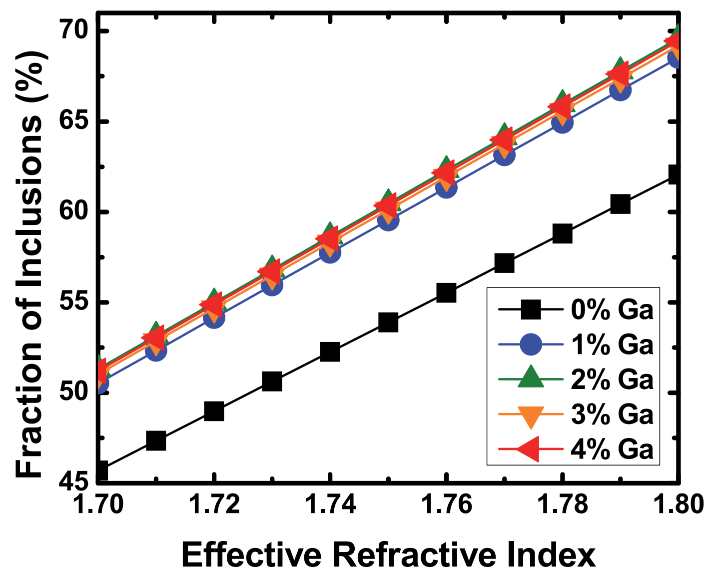

Figure 6.3: Effective Refractive Index of Ga-ZnO/PEDOT:PSS determined by MG at 403nm.

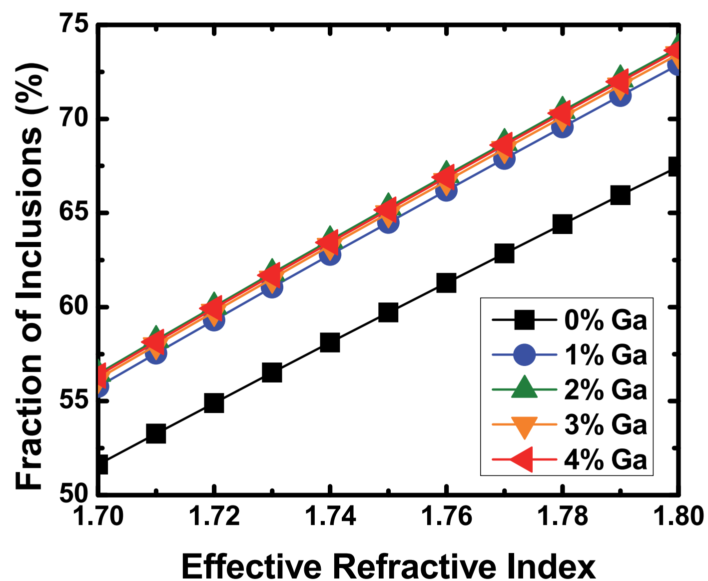

Figure 6.4: Effective Refractive Index of Ga-ZnO/PEDOT:PSS determined by LL at 403nm.

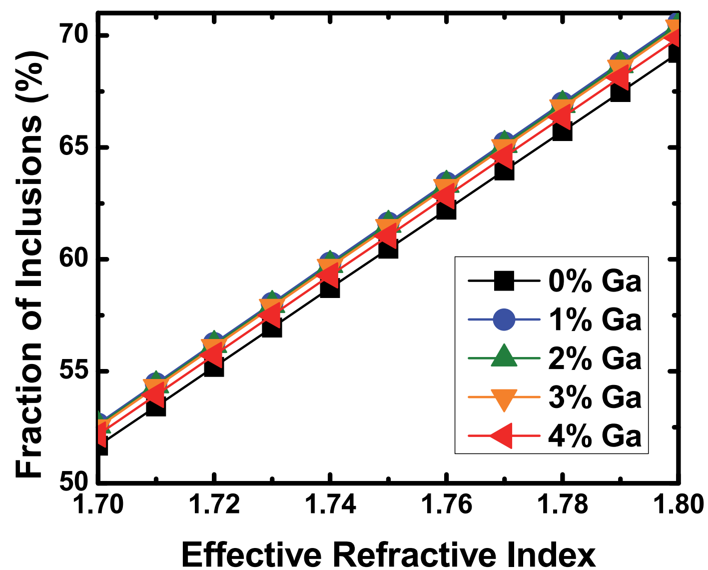

Figure 6.5: Effective Refractive Index of Ga-ZnO/PEDOT:PSS determined by BG at 550nm.

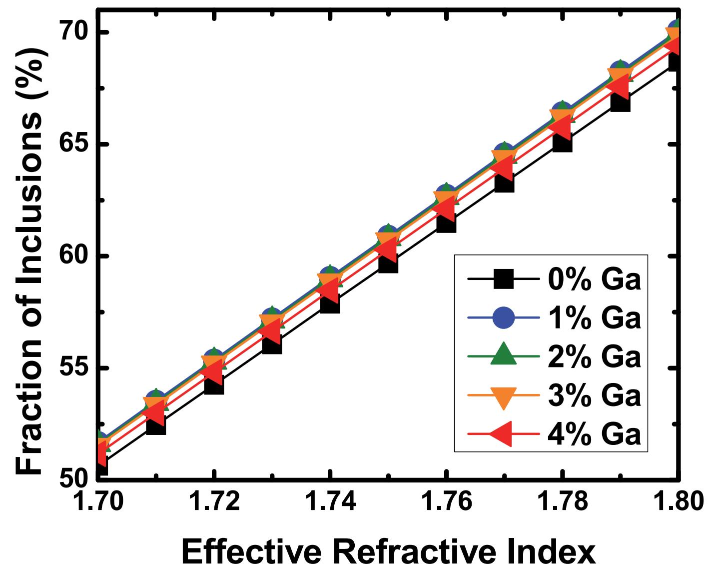

Figure 6.6: Effective Refractive Index of Ga-ZnO/PEDOT:PSS determined by MG at 550nm.

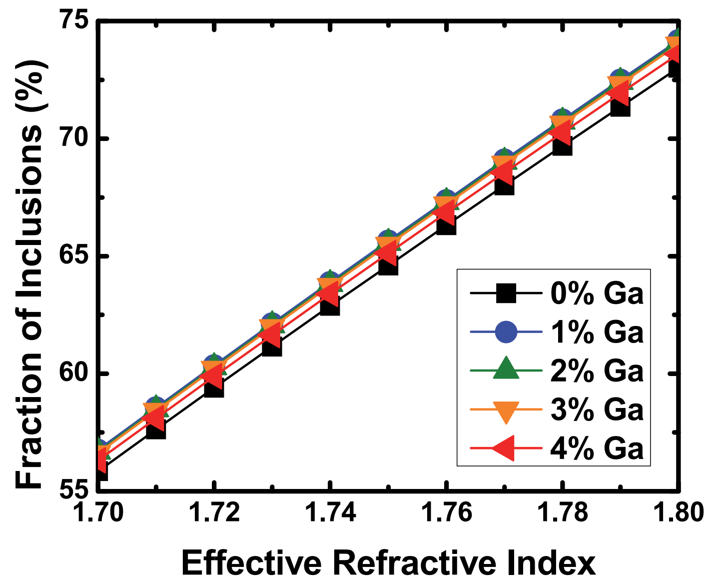

Figure 6.7: Effective Refractive Index of Ga-ZnO/PEDOT:PSS determined by LL at 550nm.

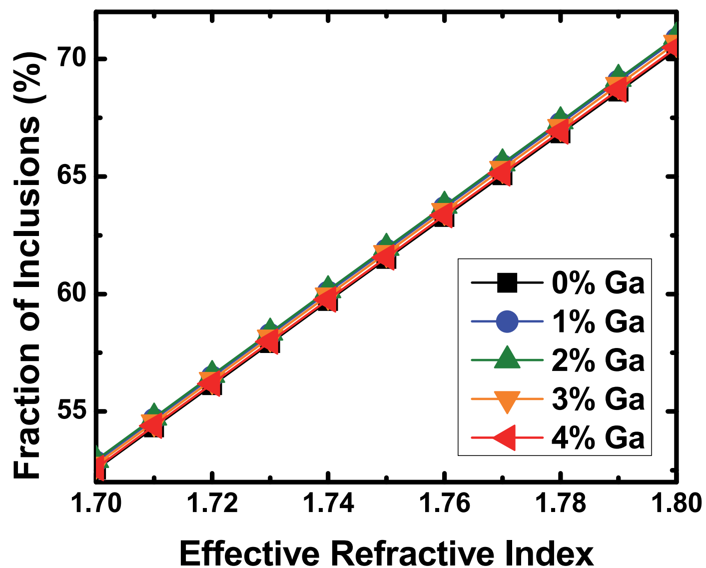

Figure 6.8: Effective Refractive Index of Ga-ZnO/PEDOT:PSS determined by BG at 650nm.

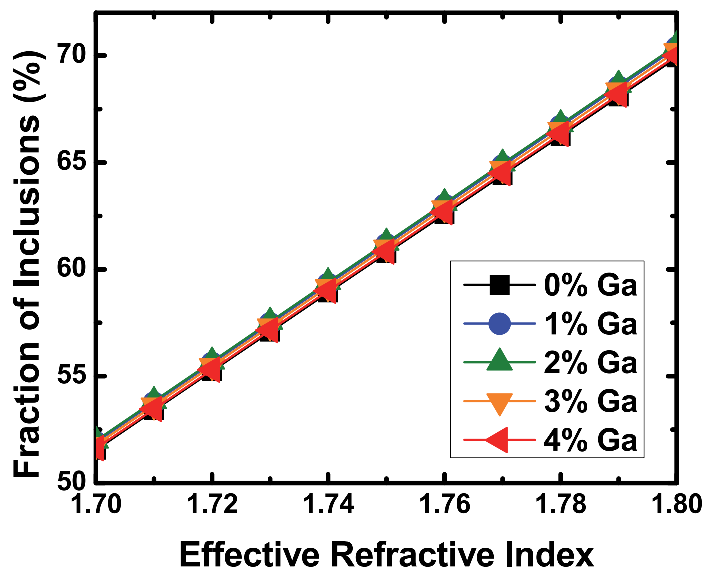

Figure 6.9: Effective Refractive Index of Ga-ZnO/PEDOT:PSS determined by MG at 650nm.

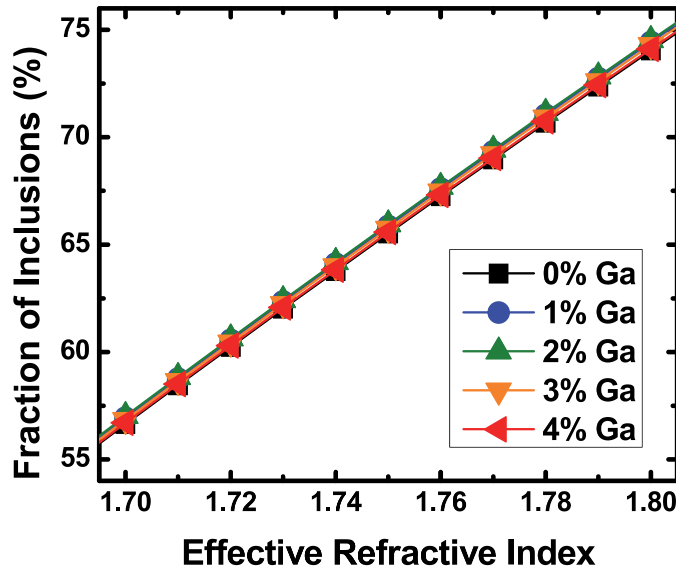

Figure 6.10: Effective Refractive Index of Ga-ZnO/PEDOT:PSS determined by LL at 650nm.

As stated before, the MG approximation is applied for relatively small inclusion volume fractions. Our calculated volume fraction, required for the effective index matching, exceeds 1/3. The result is valid since $n_L \approx n_H$ and therefore the MG and BG theories conclude an analogous result.

Light extraction efficiency can be increased by matching the refractive indices of the emissive layer and the hole transport layer (Ga-ZnO/PEDOT:PSS) in OLEDs. The matching of different active layers with their corresponding transparent conductive layers (Ga-ZnO/PEDOT:PSS) can decrease light reflection, thus increasing the efficiency of multijunction OSCs. In addition, gradual tuning of refractive index, by manipulating the inclusion volume fractions of the Ga-ZnO NPs, can be used in graded-refractive-index-structured solar cells to considerably suppress the reflectance *via* impedance matching.[38]

6.4 Conclusion

Bruggeman, Maxwell-Garnett and Lorentz-Lorenz effective medium approximations were used to simulate the refractive index of Ga-ZnO NPs dispersed in conductive polymer PEDOT:PSS. We have demonstrated how the refractive index of Ga-ZnO/PEDOT:PSS is modified by tuning the fraction of the NPs and the concentration of Ga in ZnO NPs. It was found that if the refractive index of Ga-ZnO/PEDOT:PSS is to be matched with that of the organic emissive layer (n=1.7~1.8), the desired volume fraction of the Ga-ZnO should occur between 45% and 71% when the concentration of Ga in ZnO NPs varies between 0 and 4 percent.

References

[1] V. Mirkhani, F.Tong, D. Song, Y. Chung, B. Ozden, K. Yapabandara, M. Hamilton, D.J. Kim, H. Koo, K.K. Lee and M. Park, J. Nanosci. Nanotechnol. 16, 7 (2016).

[2] E.-K. Park, M. Choi, J.-H. Jeun, K.-T. Lim, J.-M. Kim and Y.-S. Kim, Microelectronic Engineering 111, 166 (2013).

[3] X. Li, W. C. H. Choy, H. Lu, W. E. I. Sha and A. H. P. Ho, Adv. Funct. Mater. 23, 2728 (2013).

[4] F. Liu and J.-M. Nunzi, Appl. Phys. Lett. 99, 123302 (2011).

[5] Y. Xiao, J. P. Yang, P. P. Cheng, J. J. Zhu, Z. Q. Xu, Y. H. Deng, S. T. Lee, Y. Q. Li, and J. X. Tang, Appl. Phys. Lett. 100, 013308 (2012).

[6] P. Obreja, D. Cristea, M. Purica, R. Gavrila and F. Comanescu, Polimery 52, 679 (2007).

[7] M. M. Demir, K. Koynov, Ü. Akbey, C. Bubeck, I. Park, I. Lieberwirth and G. Wegner, Macromolecules 40, 1089 (2007).

[8] P. Englebienne and A. Van Hoonacker, Journal of Colloid and Interface Science 292, 445 (2005).

[9] M. Rippa, R. Capasso, L. Petti, G. Nenna, A. D. G. Del Mauro, M. Grazia Maglione and C. Minarini, J. Mater. Chem. C 3, 147 (2015).

[10] X. Wu, F. Li, W. Wu and T. Guo, Vacuum 101, 53 (2014).

[11] M. R. Lenze, N. M. Kronenberg, F. Würthner and K. Meerholz, Organic Electronics 21, 171 (2015).

[12] Y. H. Kim, C. Sachse, M. L. Machala, C. May, L. Müller-Meskamp and K. Leo, Adv. Funct. Mater. 21, 1076 (2011).

[13] S. Reineke, M. Thomschke, B. Lüssem and K. Leo, Rev. Mod. Phys. 85, 1245 (2013).

[14] H. Greiner, Jpn. J. Appl. Phys. 46, 4125 (2007).

[15] H. S. Shim, N. S. Han, J. H. Seo, S. M. Park and J. K. Song, Bull. Korean Chem. Soc. 31, 2675 (2010).

[16] C. B. Singh, S. Bhattacharya, V. Singh, P. B. Bhargav, S. Sarkar, V. Bhavanasi and N. Ahmad , J. Renewable Sustainable Energy 5, 031605 (2013).

[17] E. R. Messmer, Solar Cell Efficiency vs. Module Power Output: Simulation of a Solar Cell in a CPV Module, in Arturo Morales-Acevedo, Solar Cells - Research and Application Perspectives (pp. 316-317), InTech (2013).

[18] Y.-J. Lin and Y.-C. Su, J. Appl. Phys. 111, 073712 (2012).

[19] N. G. Semaltianos , S. Logothetidis, N. Hastas, W. Perrie, S. Romani, R.J. Potter, G. Dearden, K. G. Watkins, P. French and M. Sharp, Chemical Physics Letters 484, 283 (2010).

[20] S. Kohiki, M. Nishitani and T. Wada, J. Appl. Phys. 75, 2069 (1994).

[21] P. Nunes, E. Fortunato, P. Tonello, F. Braz Fernandes, P. Vilarinho and R. Martins, Vacuum 64, 281 (2002).

[22] E. M. Kiley, V. V. Yakovlev, K. Ishizaki and S. Vaucher, J. Microwave Power and Electromag. Energy 46 (1), 26 (2012).

[23] M. Vargas, E. J. Rubio, A. Gutierrez and C. V. Ramana, J. Appl. Phys. 115, 133511 (2014).

[24] M. Radović, Z. Dohčević-Mitrović, N. Paunović, S. Bošković, N. Tomić, N. Tadić and I. Belča, J. Phys. D: Appl. Phys. 48, 065301 (2015).

[25] M. I. Mishchenko, L. Liu, B. Cairns and D. W. Mackowski, Optics Letters 39, 2607 (2014).

[26] M. Wong, J. Guenther, L. Sun, J. Blümel, R. Nishimura and H.-J. Sue, Adv. Funct. Mater. 22, 3614 (2012).

[27] V. Janicki, J. Sancho-Parramon and H. Zorc, Thin Solid Films 516, 3368 (2008).

[28] J. C. M. Garnett, Phil. Trans. R. Soc. Lond. 203, 385 (1904).

[29] G. A. Niklasson, C. G. Granqvist and O. Hunderi, Appl. Opt. 20, 26 (1981).

[30] J. A. Blackman, in Handbook of Metal Physics: Metallic Nanoparticles, J. A. Blackman, Ed., P. Misra, Series Ed., Elsevier Science (2008), Vol. 5, p.220.

[31] Y. Zhang, Z Jiang and Z. Yu, J. Opt. Soc. Am. A 5, 1601 (1988).

[32] D.A.G. Bruggeman, Ann. Phys. (Leipzig) 24, 636 (1935).

[33] L.A. Golovan, V. Yu Timoshenko and P. K. Kashkarov, Physics-Uspekhi 50, 595 (2007).

[34] D.-T. Phan, A. A. M. Farag, F. Yakuphanoglu and G. S. Chung, J. Electroceram. 29, 12 (2012).

[35] Private Email communication with F. Yakuphanoglu, co-author of [33].

[36] C. W. Tang and S. A. VanSlyke, Appl. Phys. Lett. 51, 913 (1987).

[37] H.-C. Yeh, L.-H. Chan, W.-C. Wu and C.-T. Chen, J. Mater. Chem. 14, 1293 (2004).

[38] S. J. Jang, Y. M. Song, C. I. Yeo, C. Y. Park, J. S. Yu and Y. T. Lee, Optics Express 19, A108 (2011).

Chapter 7

Summary and Future Work

7.1 Summary

This research was mostly devoted to characterization of ZnO films and the TFTs employing the films as active channel layers synthesized *via* the sol-gel spin-coating deposition method. Zinc acetate dehydrate was mixed with monoethanolamine, diluted with isopropanol, and stirred on a hot plate to obtain a transparent, stable and homogenous precursor. The precursor was spin-coated on oxidized boron-doped silicon wafers as substrates and calcined afterwards. The spin-coating process was repeated to obtain different thicknesses on different samples. The samples were then annealed at different temperatures and the films were characterized. Despite the Raman spectroscopy and photoluminescence showing a qualitative crystal quality increase as the annealing temperature increased, SEM images revealed gaps being formed between grains as the annealing temperature reached 900 ℃ and therefore, 800 ℃ was chosen as the post-annealing temperature.

An abnormality in the transfer characteristics, transconductance and the mobility of the TFTs was observed. Hypothesizing that surface oxygen chemisorption occurs during the time interval between the spin-coating processes, an experiment was designed and implemented to examine the hypothesis. ZnO films with different number of spin-coating repetition were used to fabricate TFTs. The I-V and C-V measurements hinted to the possibility of depletion layers being

formed at the ZnO-ZnO interlayer-interfaces. A "kink effect" (or "hump effect") was observed in transfer characteristics of devices with higher number of ZnO layers and multiple peaks were apparent in their transconductance and mobility. These devices also exhibited abnormality in their C-V characteristics, resembling parasitic capacitance effects in parallel with the main capacitor. This effect, however, was absent in the single layer ZnO sample, lowering the possibility of an edge effect to be the cause of this effect in C-V measurements. Furthermore, the single layer ZnO TFT did not show any kink in its transfer characteristics. More rigorous study is advised to achieve a strong conclusion on this matter.

The radiation hardness of ZnO was corroborated by measuring gamma irradiated ZnO TFTs, using ^{60}Co tubes as the radiation source, before and after irradiation. Two samples with different thicknesses were fabricated for this experiment: one with 4 layers of ZnO, and one with 8 layers. The output characteristics indicated the functionality of the devices from both samples after gamma irradiation dose of 1.2 MGy (120 MRad). The transfer characteristics in the saturation region of transistors from the 4 layer sample indicated a reduction in saturation mobility and current ON/OFF ratio (I_{ON}/I_{OFF}), whereas the same properties were enhanced in deices from the 8 layer sample. It was conjectured that the enhancement was related to higher influence of ZnO-ZnO interlayer-interface distortion in the bulk of the 8 layer sample compared to surface effects, while the latter becomes more significant in the thinner 4 layer sample. The kink effect observed in both samples before irradiation, caused by ZnO-ZnO interlayer-interfaces, was absent in the measurements conducted after gamma irradiation dose of 1.2 MGy. AFM and High Resolution Digital Optical Microscopy images confirmed diminishing of the ZnO channel layers as the irradiation dose increased. A model was proposed based on the displacement damage occurring at the surface, due to photon-electron Compton scattering, to explain the gradual etching of the film.

The rise in the blue/violet/UV luminescence of the samples after irradiation implied a surge in zinc vacancies and zinc interstitials.

In addition to the aforementioned research on ZnO TFTs, modification of the refractive index of PEDOT:PSS by gallium doped ZnO nanoparticle inclusions based on volume fraction was studied. Three effective medium approximations (Bruggeman, Maxwell-Garnett and Lorentz-Lorenz) were used to find the appropriate volume fraction of the doped nanoparticle inclusions (n~2) in PEDOT:PSS (n_L = 1.42) to match the index of refraction for organic polymer emissive layer (n=1.7~1.8) in OLEDs. It was found that for gallium doped ZnO nanoparticles, with doping concentration ranging from 0% to 4%, the volume fraction of inclusions inside the PEDOT:PSS matrix should vary between 45% and 71%.

7.2 Future Work

The effect of ZnO-ZnO interlayer-interfaces was investigated by exploiting the number of ZnO layers deposited *via* sol-gel spin-coating method. The claim can be further investigated by drastically elongating the time interval between the spin-coating processes, exposing the top ZnO surface to the ambient even further before the next deposition. If the deposition process (spin-coating and calcination processes) is realized inside an isolated environment with non-reactive ambient, such as an argon filled glovebox, the absence of a depletion layer at the ZnO-ZnO interlayer-interfaces can be investigated.

Radiation hardness of ZnO was highlighted in this work, approving previous reports, with TFTs having unpassivated channel layers as thin as 200 microns functioning after being exposed to a relatively high gamma irradiation dose. The malfunction of transistors with a smaller channel thickness was credited to the consequences of displacement damage on the surface, causing

ballistic ejection of surface atoms. Passivating the ZnO active layer may affect the etching process and the carrier mobility. This passivation layer may, however, introduce impurities into the ZnO layer. Annealing the passivation layer after deposition and the irradiation effects on device performance can be further investigated. Finally, C-V measurements before and after irradiation offer insightful material for scrutinizing the displacement damage, the ZnO/SiO_2 interface traps and the induced SiO_2 positive charges in the bulk.